8824

p. 146

ds QM 593208
jmx

OSU

The Ohio State University

ASYMPTOTIC HIGH FREQUENCY ANALYSIS OF THE ELECTROMAGNETIC BACKSCATTERING FROM AN INLET MODEL CONSISTING OF PIECEWISE LINEARLY TAPERED SECTIONS

By

A. Altintas
P.H. Pathak

The Ohio State University

ElectroScience Laboratory

Department of Electrical Engineering
Columbus, Ohio 43212

(NASA-CR-176844) ASYMPTOTIC HIGH FREQUENCY ANALYSIS OF THE ELECTROMAGNETIC BACKSCATTERING FROM AN INLET MODEL CONSISTING OF PIECEWISE LINEARLY TAPERED SECTIONS (Ohio State Univ.) 146 p

N86-26486

HC# A07/MF #A01

Unclas
G3/32 43427

8824

Technical Report No. 716148-6
Grant No. NSG 1613
November 1985

National Aeronautics and Space Administration
Langley Research Center
Hampton, Virginia 23635

NOTICES

When Government drawings, specifications, or other data are used for any purpose other than in connection with a definitely related Government procurement operation, the United States Government thereby incurs no responsibility nor any obligation whatsoever, and the fact that the Government may have formulated, furnished, or in any way supplied the said drawings, specifications, or other data, is not to be regarded by implication or otherwise as in any manner licensing the holder or any other person or corporation, or conveying any rights or permission to manufacture, use, or sell any patented invention that may in any way be related thereto.

50272-101

REPORT DOCUMENTATION PAGE	1. REPORT NO. 716148-6	2.	3. Recipient's Accession No.

4. Title and Subtitle
ASYMPTOTIC HIGH FREQUENCY ANALYSIS OF THE ELECTROMAGNETIC BACKSCATTERING FROM AN INLET MODEL CONSISTING OF PIECEWISE LINEARLY TAPERED SECTIONS

5. Report Date
November 1985

6.

7. Author(s)
A. Altintas, P.H. Pathak

8. Performing Organization Rept. No.
716148-6

9. Performing Organization Name and Address
The Ohio State University
ElectroScience Laboratory
1320 Kinnear Road
Columbus, Ohio 43212

10. Project/Task/Work Unit No.

11. Contract(C) or Grant(G) No.
(C)
(G) NSG 1613

12. Sponsoring Organization Name and Address
National Aeronautics and Space Administration
Langley Research Center
Hampton, Virginia 23635

13. Type of Report & Period Covered
Technical

14.

15. Supplementary Notes

ORIGINAL PAGE IS
OF POOR QUALITY

16. Abstract (Limit: 200 words)

Electromagnetic backscattering from an open-ended three-dimensional inlet model in analyzed and computed patterns are compared with results of experimental measurements. The model is comprised of two sections. The first section consists of a linearly-tapered waveguide with a rectangular opening at one end and the other end is connected to the second section which is a uniform rectangular waveguide with a planar perfectly conducting termination. The model is electrically large so that many propagating modes are excited. The method of analysis contains conventional aperture integration and modal techniques combined with high frequency techniques, which employ concepts such as modal rays, geometrical theory of diffraction and equivalent currents. For the cases considered, it is shown that only a few of the many propagating modes contribute appreciably to the backscattered field. These modes are selected according to their modal ray angle directions.

17. Document Analysis a. Descriptors

* BACKSCATTERING
ELECTROMAGNETIC FIELDS
* INLET NOZZLES
* ELECTROMAGNETIC SCATTERING
WAVE DIFFRACTION
* " PROPAGATION
* " PATTERNS
TAPERING
WAVEGUIDES
GEOMETRICAL THEORY OF DIFFRACTION

b. Identifiers/Open-Ended Terms

c. COSATI Field/Group

18. Availability Statement	19. Security Class (This Report) Unclassified	21. No. of Pages 135
	20. Security Class (This Page) Unclassified	22. Price

(See ANSI-Z39.18) See Instructions on Reverse OPTIONAL FORM 272 (4-77) (Formerly NTIS-35) Department of Commerce

TABLE OF CONTENTS

		PAGE
LIST OF FIGURES		iv
CHAPTER		
I	INTRODUCTION	1
II	ANALYSIS OF ELECTROMAGNETIC BACKSCATTERING FROM AN INLET STRUCTURE	3
III	DIRECT SCATTERING FROM THE RIM AT THE OPEN END	8
	i.) Singly-diffracted field contribution from edges 1 and 2	12
	ii.) Singly-diffracted field contribution from edges 3 and 4	15
	iii.) Double diffraction from vertical edges in the case of x-z plane scan	18
	iv.) Numerical results for Chapter III	20
IV	THE ANALYSIS OF INTERIOR CAVITY EFFECTS	55
	Numerical Results for Chapter IV	62
V	CONCLUSIONS	111
REFERENCES		113
APPENDIXES		
I	MODAL FIELD EXPRESSIONS IN A RECTANGULAR WAVEGUIDE	114
II	MODAL FIELD EXPRESSIONS IN A LINEARLY TAPERED WAVEGUIDE	119
III	APPLICATION OF THE RECIPROCITY THEOREM TO FIND THE COUPLING OF INCIDENT ENERGY INTO THE MODAL FIELD BY KNOWING THE MODAL RADIATION FROM THE OPEN END OF A RECTANGULAR WAVEGUIDE	126
IV	CORRECTION FOR THE APERTURE INTEGRATION	131

LIST OF FIGURES

FIGURE		PAGE
1.	The geometry of the inlet model.	3
2.	Side and top view of the inlet model.	4
3.	Geometry of an open-ended rectangular waveguide cavity.	5
4.	Numbering of the edges.	11
5.	Aspect angle scan in horizontal (x-z) plane. Vertical ($\hat{\phi}$) polarization, frequency = 8.02 GHz.	22
6.	Aspect angle scan in horizontal (x-z) plane. Vertical ($\hat{\phi}$) polarization, frequency = 9.98 GHz.	23
7.	Aspect angle scan in horizontal (x-z) plane. Vertical ($\hat{\phi}$) polarization, frequency = 11.95 GHz.	24
8.	Aspect angle scan in horizontal (x-z) plane. Horizontal ($\hat{\theta}$) polarization, frequency = 8.02 GHz.	25
9.	Aspect angle scan in horizontal (x-z) plane. Horizontal ($\hat{\theta}$) polarization, frequency = 9.98 GHz.	26
10.	Aspect angle scan in horizontal (x-z) plane. Horizontal ($\hat{\theta}$) polarization, frequency = 11.95 GHz.	27
11.	Aspect angle scan in vertical (y-z) plane. Horizontal ($\hat{\phi}$) polarization, frequency = 8.02 GHz.	28

FIGURE PAGE

12. Aspect angle scan in vertical (y-z) plane. Horizontal ($\hat{\phi}$) polarization, frequency = 9.98 GHz. 29

13. Aspect angle scan in vertical (y-z) plane. Horizontal ($\hat{\phi}$) polarization, frequency = 11.95 GHz. 30

14. Aspect angle scan in vertical (y-z) plane. Vertical ($\hat{\theta}$) polarization, frequency = 8.02 GHz. 31

15. Aspect angle scan in vertical (y-z) plane. Vertical ($\hat{\theta}$) polarization, frequency = 9.98 GHz. 32

16. Aspect angle scan in vertical (y-z) plane. Vertical ($\hat{\theta}$) polarization, frequency = 11.95 GHz. 33

17a. Frequency scan in horizontal (x-z) plane. ϕ=0°, θ=0°, vertical ($\hat{\phi}$) polarization. 36

17b. Inverse Fourier transforms. 37

18a. Frequency scan in horizontal (x-z) plane. ϕ=0°, θ=15°, vertical ($\hat{\phi}$) polarization. 38

18b. Inverse Fourier transforms. 39

19a. Frequency scan in horizontal (x-z) plane. ϕ=0°, θ=30°, vertical ($\hat{\phi}$) polarization. 40

19b. Inverse Fourier transforms. 41

20a. Frequency scan in horizontal (x-z) plane. ϕ=0°, θ=45°, vertical ($\hat{\phi}$) polarization. 42

20b. Inverse Fourier transforms. 43

21a. Frequency scan in horizontal (x-z) plane. ϕ=0°, θ=0°, horizontal ($\hat{\theta}$) polarization. 44

FIGURE		PAGE
21b.	Inverse Fourier transforms.	45
22a.	Frequency scan in horizontal (x-z) plane. ϕ=0°, θ=15°, horizontal ($\hat{\theta}$) polarization.	46
22b.	Inverse Fourier transforms.	47
23a.	Frequency scan in horizontal (x-z) plane. ϕ=0°, θ=30°, horizontal ($\hat{\theta}$) polarization.	48
23b.	Inverse Fourier transforms.	49
24a.	Frequency scan in horizontal (x-z) plane. ϕ=0°, θ=45°, horizontal ($\hat{\theta}$) polarization.	50
24b.	Inverse Fourier transforms.	51
25a.	Frequency scan in horizontal (x-z) plane. ϕ=0°, θ=45°, vertical ($\hat{\phi}$) polarization.	53
25b.	Inverse Fourier transforms.	54
26.	Importance of modes whose modal ray angles are near the angle of incidence.	64
27a.	Aspect angle scan in horizontal (x-z) plane. Vertical (ϕ) polarization, frequency 8.0 GHz.	66
27b.	Calculated aspect angle scans corresponding to Figure 27a.	67
28a.	Aspect angle scan in horizontal (x-z) plane. Vertical ($\hat{\phi}$) polarization, frequency 10.0 GHz.	68
28b.	Calculated aspect angle scans corresponding to Figure 28a.	69
29a.	Aspect angle scan in horizontal (x-z) plane. Vertical (ϕ) polarization, frequency 12.0 GHz.	70
29b.	Calculated aspect angle scans corresponding to Figure 29a.	71

FIGURE PAGE

30a. Aspect angle scan in horizontal (x-z) plane. Horizontal ($\hat{\theta}$) polarization, frequency 8.02 GHz. 72

30b. Calculated aspect angle scans corresponding to Figure 30a. 73

31a. Aspect angle scan in horizontal (x-z) plane. Horizontal ($\hat{\theta}$) polarization, frequency 9.98 GHz. 74

31b. Calculated aspect angle scans corresponding to Figure 31a. 75

32a. Aspect angle scan in horizontal (x-z) plane. Horizontal ($\hat{\theta}$) polarization, frequency 11.95 GHz. 76

32b. Calculated aspect angle scans corresponding to Figure 32a. 77

33a. Aspect angle scan in vertical (y-z) plane. Vertical ($\hat{\theta}$) polarization, frequency 8.02 GHz. 78

33b. Calculated aspect angle scans corresponding to Figure 33a. 79

34a. Aspect angle scan in vertical (y-z) plane. Vertical ($\hat{\theta}$) polarization, frequency 10.01 GHz. 80

34b. Calculated aspect angle scans corresponding to Figure 34a. 81

35a. Aspect angle scan in vertical (y-z) plane. Vertical ($\hat{\theta}$) polarization, frequency 11.96 GHz. 82

35b. Calculated aspect angle scans corresponding to Figure 35a. 83

36a. Aspect angle scan in vertical (y-z) plane. Horizontal ($\hat{\phi}$) polarization, frequency 8.02 GHz. 84

36b. Calculated aspect angle scans corresponding to Figure 36a. 85

37a. Aspect angle scan in vertical (y-z) plane. Horizontal ($\hat{\phi}$) polarization, frequency 10.01 GHz. 86

FIGURE		PAGE
37b.	Calculated aspect angle scans corresponding to Figure 37a.	87
38a.	Aspect angle scan in vertical (y-z) plane. Horizontal ($\hat{\phi}$) polarization, frequency 11.96 GHz.	88
38b.	Calculated aspect angle scans corresponding to Figure 38a.	89
39.	Calculated aspect angle scans in the plane ϕ=45°, $\hat{\phi}$ polarization, frequency = 10.0 GHz.	90
40.	Calculated aspect angle scans in the plane ϕ=45°, $\hat{\theta}$ polarization, frequency = 10.0 GHz.	91
41.	Calculated aspect angle scans in the plane ϕ=45°, $\hat{\theta}$ polarization, frequency = 10 GHz.	92
42a.	Frequency scan in horizontal (x-z) plane. ϕ=0°, θ=0°, vertical ($\hat{\phi}$) polarization.	93
42b.	Inverse Fourier transform.	94
43a.	Frequency scan in horizontal (x-z) plane. ϕ=0°, θ=15°, vertical ($\hat{\phi}$) polarization.	95
43b.	Inverse Fourier transforms.	96
44a.	Frequency scan in horizontal (x-z) plane. ϕ=0°, θ=30°, vertical ($\hat{\phi}$) polarization.	97
44b.	Inverse Fourier transforms.	98
45a.	Frequency scan in horizontal (x-z) plane. ϕ=0°, θ=45°, vertical ($\hat{\phi}$) polarization.	99
45b.	Inverse Fourier transforms.	100

FIGURE PAGE

46a. Frequency scan in horizontal (x-z) plane. ϕ=0°, θ=0°, horizontal ($\hat{\theta}$) polarization. 101

46b. Inverse Fourier transforms. 102

47a. Frequency scan in horizontal (x-z) plane. ϕ=0°, θ=15°, horizontal ($\hat{\theta}$) polarization. 103

47b. Inverse Fourier transforms. 104

48a. Frequency scan in horizontal (x-z) plane. ϕ=0°, θ=30°, horizontal ($\hat{\theta}$) polarization. 105

48b. Inverse Fourier transforms. 106

49a. Frequency scan in horizontal (x-z) plane. ϕ=0°, θ=45°, horizontal ($\hat{\theta}$) polarization. 107

49b. Inverse Fourier transforms. 108

50. The separate returns of modes for the case in Figure 45b. 109

A1. Rectangular waveguide geometry. 114

A2. Geometry of a linearly tapered waveguide. 119

A3. The geometry of the problem. 126

A4. Scattering from a perfectly-conducting half-plane. 131

A5. The integration path c_α. 134

CHAPTER I

INTRODUCTION

In this study, an analysis of electromagnetic backscattering from an open ended inlet cavity is performed, and the calculations based on this analysis are compared with experimental measurements.

The wave scattered by the inlet cavity when it is illuminated by an external source is composed mainly of two effects. The first is due to the diffraction from the rim at the open-end of the inlet and the second is due to the coupling of the incident electromagnetic energy into cavity modes which bounce around inside the cavity before radiating from the open end. The inlet cavity considered here is assumed to have perfectly conducting walls.

The analysis is done on an inlet model with overall dimensions of several wavelengths; therefore, there are quite a few propagating modes inside the cavity. The modal analysis is complemented with the high frequency techniques such as the Geometrical Theory of Diffraction (GTD), the Equivalent Current Method (ECM), the Aperture Integration (AI) and a modification of the Physical Theory of Diffraction (PTD). The edge diffraction, due to the rim of the open-end, is calculated via the ECM in which the equivalent currents are found from GTD. The AI together with a modified PTD approach is applied to get the modal

coupling into the interior and its subsequent radiation back into the exterior region. Since there are many propagating modes inside the cavity, it is expected that only a few modes which are closely phase matched to the direction of the incident wave are strongly excited. This claim is tested and comparisons with measurements are also shown.

The experimental measurements are performed on a model at the compact range facility of the ElectroScience Laboratory of the Ohio State University.

CHAPTER II

ANALYSIS OF ELECTROMAGNETIC BACKSCATTERING FROM AN INLET STRUCTURE

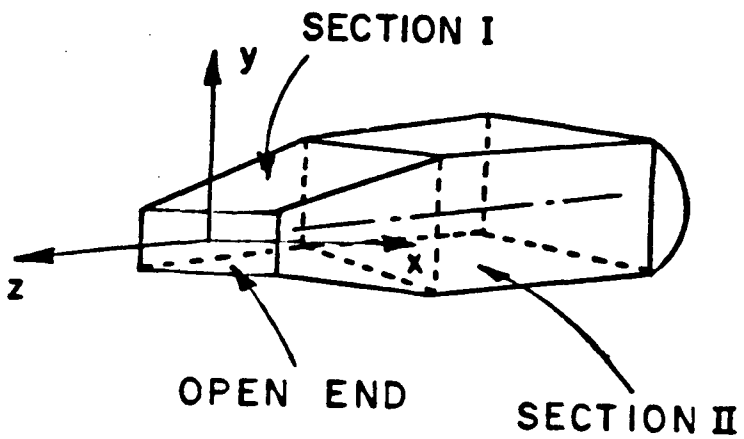
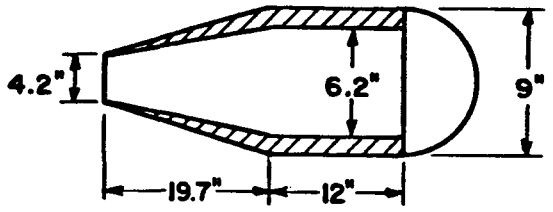


Figure 1. The geometry of the inlet model.

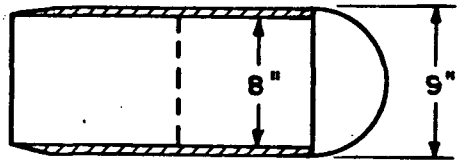
The inlet model of interest in this work is shown in Figure 1. It is basically an open-ended cavity composed of two waveguide sections. The first section is part of a linearly tapered waveguide with one end open; the other end of this section is connected to the second section which is a uniform waveguide with a planar termination inside. The exterior of the second section is curved at the back end to minimize the scattering coming from the exterior features of the structure. The axis of the inlet coincides with the z-axis of the coordinate system, and the

y-axis is in the vertical direction. The model is made of wood and then made conductive using a conductive paint. The dimensions of of the inlet are shown in Figure 2.

The side walls in each of the waveguide sections are parallel to the y-z plane; therefore, there is no tapering effect to be included for those walls. The first step in the analysis is finding the modal field expressions in rectangular and linearly tapered waveguide sections. This is done in Appendices I and II where the expressions are given, and the relationship between the mode sets of linearly tapered and rectangular waveguides is shown. Therefore, the effect of tapering



(a) SIDE VIEW



(b) TOP VIEW

Figure 2. Side and top view of the inlet model.

can be included by modifying the propagation constant in the rectangular waveguide mode expressions which are transverse to the x-direction. So, the analysis is first done on a rectangular cavity as shown in Figure 3, and the solution is modified subsequently to include the effect of tapering.

The geometry of the waveguide structure is shown in Figure 3. The cross-sectional dimensions of the waveguide are "a" and "b" in the x and y-coordinate directions respectively. The length of the waveguide from the open end to the back wall is given by the dimension L. All of the walls of the cavity are assumed to be perfectly conducting. The structure is illuminated by an incident plane wave (e^{jwt} time convention is assumed and suppressed) which is given by

$$\bar{E}^i = (E^i_\theta \hat{\theta} + E^i_\phi \hat{\phi})\, e^{jk(x\sin\theta^i\cos\phi^i + y\sin\theta^i\cos\phi^i + z\cos\theta^i)} \qquad (1)$$

where $0 \leq \theta^i < \pi/2$, $0 \leq \phi^i \leq 2\pi$ are the elevation and aspect angles of the incident field direction, respectively, and k is the free space wavenumber.

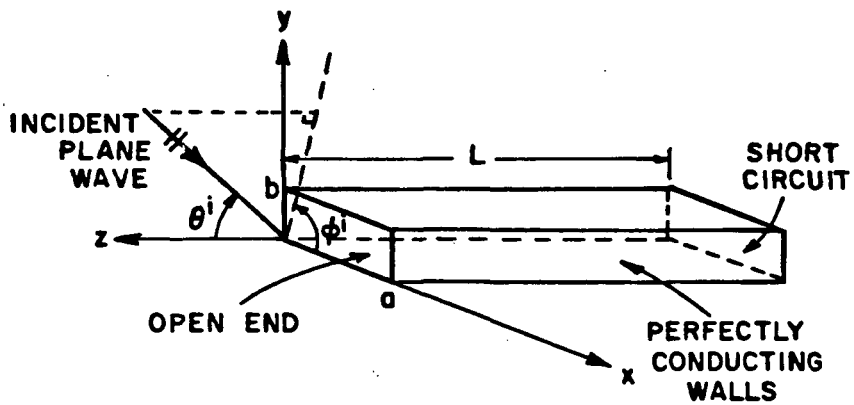


Figure 3. Geometry of an open-ended rectangular waveguide cavity.

The scattered field is composed of two main contributions; one of these is due to the field scattered from the open end by itself, and the other is due to the field which is radiated from the open end. The latter undergoes multiple reflections between the open end and the termination at the back wall after it is initially coupled into the waveguide from the incident field. The fields resulting from these multiple interactions may be expressed as a convergent Neumann series as done by Pace and Mittra [1]. The same result is directly obtained by an alternative procedure based on a self-consistent method [2]. However, from experimental measurements, these multiple interactions are determined to be negligibly small for the inlet model being considered here; therefore, their effect is ignored in this study. Only the first order interaction is discussed which contains the coupling of the incident energy into the interior waveguide modes through the open end, and subsequent reflection of these modes from the back wall and finally, the radiation of these reflected modes from the open end. In Appendix III, it is shown that the mechanisms of coupling into and radiation from the open-end are equivalent via the reciprocity principle.

For a finite cross-section, the field incident at the open end excites a finite number of modes which propagate in the $-\hat{z}$ direction without attenuation, as well as an infinite number of evanescent modes which attenuate exponentially away from the open end in the $-\hat{z}$ direction. In this study, it will be assumed that the dimensions "a" and "b" are large enough to excite at least a few propagating modes and

the length "L" is long enough for the effects of the evanescent modes to be negligible.

In the third chapter of this report the analysis of direct edge diffraction from the rim of the open end is discussed; whereas, the discussion of the wave interaction between the open end and back wall is given in Chapter IV.

CHAPTER III

DIRECT SCATTERING FROM THE RIM AT THE OPEN END

In this section, the direct scattering from the rim (edge) at the open end is calculated using techniques based on Geometrical Theory of Diffraction (GTD). According to the GTD, the scattered field is initiated from some distinct points (diffraction points) on the rim edge as well as from the corners of the rim, respectively as a result of Keller's generalization of the Fermat's principle [3]. In addition to the singly edge and corner diffracted fields, there are multiply diffracted fields which are produced by rays that undergo multiple diffractions across the aperture. These multiple interactions may become important if the aperture dimensions are not sufficiently large in terms of the wavelength.

The diffraction points migrate around the rim edge as the observation point changes position. In some cases, there may be a continuum of diffraction points contributing to the scattered field which produces a cuastic of the diffracted rays. In the case of backscattering when the incident field direction is parallel to x-z (or y-z) plane, every point contributes to edge diffraction. In order to

get a bounded result, one can use the so-called Equivalent Current Method (ECM) [4] based on the GTD. Away from the caustic regions where GTD is valid, the ECM generally blends into the GTD solution provided the inlet opening is sufficiently large in terms of the wavelength. The use of ECM also automatically, albeit approximately takes into account the presence of the corners at the waveguide opening.

In the ECM, the equivalent currents $\bar{I}_{eq}$ and $\bar{M}_{eq}$ of the electric and magnetic type, respectively, are located at the rim, and they radiate in free space to give the diffracted field. The strengths of the equivalent currents are calculated from the GTD, but since they are incorporated in an integral, they give bounded results in the caustic regions of the GTD.

The strengths of equivalent electric and magnetic currents are given by [4]

$$\bar{I}_{eq} = - \frac{\hat{e} \cdot \bar{E}^i(\text{edge})}{Z_o \sin\beta_i \sin\beta_d} D_s(\psi,\psi') \sqrt{\frac{8\pi}{jk}}\, \hat{e} \quad , \tag{2}$$

and

$$\bar{M}_{eq} = - \frac{\hat{e} \cdot \bar{H}^i(\text{edge})}{Y_o \sin\beta_i \sin\beta_d} D_h(\psi,\psi') \sqrt{\frac{8\pi}{jk}}\, \hat{e} \tag{3}$$

where the half-plane diffraction coefficient is given by

$$D_{\substack{s \\ h}}(\psi,\psi') = \frac{-e^{-j\pi/4}}{2\sqrt{2\pi k}} \left[\frac{1}{\cos\frac{\psi-\psi'}{2}} \mp \frac{1}{\cos\frac{\psi+\psi'}{2}} \right] \tag{4}$$

which can also be written as follows:

$$D_{\begin{bmatrix} s \\ h \end{bmatrix}}(\psi,\psi') = \frac{-e^{-j\pi/4}}{\sqrt{2\pi k}} \frac{\begin{vmatrix} \sin \psi/2 \sin \psi'/2 \\ \cos \psi/2 \cos \psi'/2 \end{vmatrix}}{\cos \psi + \cos \psi'} \qquad (5)$$

The other parameters in Equations (2) and (3) are defined as follows:

$\hat{e}$: unit vector along the edge direction

$Z_o = Y_o^{-1}$: free-space impedance, and

β_i, (β_d) : the angles between the edge and incident (or diffracted) field direction.

To define the angles ψ' and ψ, one first projects the vectors in the incident and diffracted field directions into a plane perpendicular to the edge direction. Then ψ' is the angle between the half-plane surface and the projected incident field direction. The angle ψ is similarly defined. The angles ψ' and ψ are measured from the inner faces of the waveguide.

The radiated electric field is computed by

$$\bar{E}^{s1} = \frac{jkZ_o}{4\pi} \int_{rim} [\hat{R} \times \hat{R} \times \bar{I}_{eq} + Y_o \hat{R} \times \bar{M}_{eq}] \frac{e^{-jkR}}{R} d\ell' \qquad (6)$$

where $\bar{R} = R\hat{R}$ is the vector pointing toward the observation point from a source point on the rim. If the observation point is very far away from the open end, one can make the following approximations:

$$R \cong r - \hat{r} \cdot \bar{r}' \quad \text{and} \quad \hat{R} \cong \hat{r} \qquad (7a;b)$$

where $\bar{r}=r\hat{r}$ is the vector pointing toward the observation point from the origin. Also, $\bar{r}'=x'\hat{x}+y'\hat{y}$ is the vector from the origin to the source point. The unit vector in the observation direction is defined by

$$\hat{r} = \hat{x}\sin\theta\cos\phi + \hat{y}\sin\theta\sin\phi + \hat{z}\cos\theta \qquad (8)$$

where θ and ϕ are the elevation and azimuth angles.

As shown in Figure 2, the edges are numbered from 1 to 4. Singly diffracted fields from each edge are calculated separately, and total edge diffraction from the rim is found by adding the results for each edge.

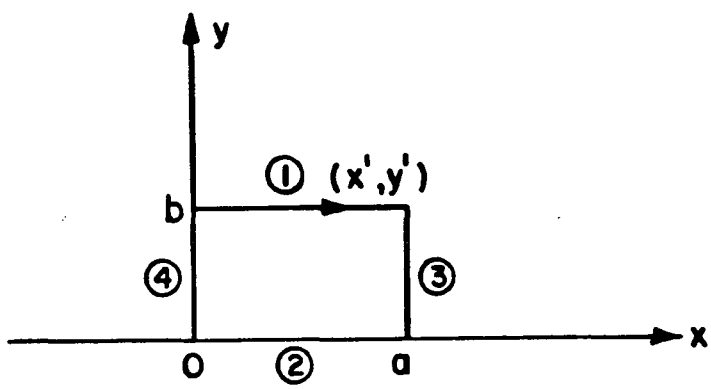


Figure 4. Numbering of the edges.

i.) Singly-diffracted field contribution from edges 1 and 2

Edges 1 and 2 are the upper and lower horizontal edges as shown in Figure 4. Their contributions are similar in the far field; therefore, the expressions for edge 1 are given first, then the total contribution from both 1 and 2 are found.

According to the above definitions, one finds that

$$\cos\psi' = -\frac{\cos\theta^i}{\sin\beta_i} \qquad \cos\psi = -\frac{\cos\theta}{\sin\beta_d} \tag{9a;b}$$

$$\sin\beta_i = \sqrt{1-\sin^2\theta^i\cos^2\phi^i} \qquad \sin\beta_d = \sqrt{1-\sin^2\theta\cos^2\phi} \tag{10a;b}$$

$$\bar{I}_{eq}(x',y') = -\frac{[E_\theta^i \cos\theta^i\cos\phi^i + E_\phi^i(-\sin\phi^i)]\, e^{jk(x'\sin\theta^i\cos\phi^i + y'\sin\theta^i\sin\phi^i)}}{Z_o \sin\beta_i \sin\beta_d} D_s(\psi,\psi')\sqrt{\frac{8\pi}{jk}}\,\hat{x} \tag{11}$$

and

$$\bar{M}_{eq} = -\frac{[E_\phi^i \cos\theta^i\cos\phi^i - E_\theta^i(-\sin\phi^i)]\, e^{jk(x'\sin\theta^i\cos\phi^i + y'\sin\theta^i\sin\phi^i)}}{\sin\beta_i \sin\beta_d} D_h(\psi,\psi')\sqrt{\frac{8\pi}{jk}}\,\hat{x} \quad . \tag{12}$$

Substituting Equations (11) and (12) into Equation (6) and adjusting the domain of integration for edge 1, one obtains that

$$\bar{E}_1^{s1} = \frac{jk}{4\pi r} \frac{e^{-jkr}}{\sin\beta_i \sin\beta_d} \sqrt{\frac{8\pi}{jk}}$$

$$\left[\hat{\theta} \left[(E_\theta^i \cos\theta^i \cos\phi^i \cos\theta\cos\phi - \sin\theta^i \cos\theta\cos\phi E_\phi^i)\, D_s(\psi,\psi') \right.\right.$$

$$\left. + (-E_\phi^i \cos\theta^i \cos\phi^i \sin\phi + E_\theta^i \sin\phi^i \sin\phi)\, D_h(\psi,\psi') \right]$$

$$+\hat{\phi} \left[(-E_\theta^i \cos\theta^i \cos\phi^i \sin\phi - E_\phi^i \sin\phi^i \sin\phi)\, D_s(\psi,\psi') \right.$$

$$\left.\left. + (-E_\phi^i \cos\theta^i \cos\phi^i \cos\theta\cos\phi + E_\theta^i \sin\phi^i \cos\theta\cos\phi)\, D_h(\psi,\psi') \right] \right]$$

$$\int_0^a e^{jk[x'(\sin\theta^i\cos\phi^i + \sin\theta\cos\phi) + b(\sin\theta^i\sin\phi^i + \sin\theta\sin\phi)]}\, dx' \qquad (13)$$

This expression simplifies in the case of backscattering, namely $\theta^i=\theta$ and $\phi^i=\phi$. As mentioned above, the contribution from edge 2 is similar to Equation (13), the total contribution from edges 1 and 2 for the backscatter case is given by

$$\bar{E}^{s1}_{12} = \frac{1}{\pi kr}\,\frac{e^{-jkr}}{\sin^2\beta_i}\,\frac{\cos(kb\sin\theta^i\sin\phi^i)}{\cos\psi}\,\frac{\sin(ka\sin\theta^i\cos\phi^i)}{\sin\theta^i\cos\phi^i}$$

$$e^{\,j\frac{ka}{2}\sin\theta^i\cos\phi + j\frac{kb}{2}\sin\theta^i\sin\phi^i}$$

$$\left[\hat{\theta}\left[(E^i_\theta\cos^2\theta^i\cos^2\phi^i - E^i_\phi\sin\phi^i\cos\phi^i\cos\theta^i)\sin^2\frac{\psi'}{2}\right.\right.$$

$$\left.\left.+(E^i_\phi\cos\theta^i\cos\phi^i\sin\phi^i - E^i_\theta\sin^2\phi^i)\cos^2\frac{\psi'}{2}\right]\right.$$

$$\left.+\hat{\phi}\left[(-E^i_\theta\cos\theta^i\cos\phi^i\sin\phi^i - E^i_\phi\sin^2\phi^i)\sin^2\frac{\psi'}{2}\right.\right.$$

$$\left.\left.+(E^i_\phi\cos^2\theta^i\cos^2\phi^i - E^i_\theta\sin\phi^i\cos\theta^i\cos\phi^i)\cos^2\frac{\psi'}{2}\right]\right] \quad . \qquad (14)$$

For the backscattered field scan in the x-z plane, where $\phi^i=0$, $\psi'=\pi$, one obtains that

$$\bar{E}^{s1}_{12} = -\hat{\theta}\,\frac{e^{-jkr}}{kr}\,e^{\,j\frac{ka}{2}\sin\theta^i}\,\frac{E^i_\theta}{\pi}\,\frac{\sin(ka\sin\theta^i)}{\sin\theta^i} \quad . \qquad (15)$$

Since both horizontal edges scatter always in phase in this plane, the singly diffracted field contribution of horizontal edges is independent of the dimension b. For an observation scan in the x-z plane none of the points along the horizontal edges satisfy the Generalized Fermat's principle. Therefore, there is no edge diffraction contribution from horizontal edges. But, since the edges are of finite length, the corners give a scattered field in every direction. At this

time there is an available approximate, uniform corner diffraction coefficient which is partly based on heuristic arguments [4]. If this corner diffraction coefficient is employed, one will simply obtain the result in Equation (15) as long as one is away from the shadow boundaries of edge diffracted fields. However, since the latter will be true in the present work, this ECM approach will yield the same result as that obtained from the use of the above corner diffraction coefficient. It is noted that in the far zone, only the corner diffraction effects dominate the total rim scattering; i.e, only the end points of the rim edges dominate rather than the whole length of the edges except in the caustic region where the entire length of the rim contributes to the field.

ii.) Singly-diffracted field contribution from edges 3 and 4

In this case, Equations (2) and (3) take the following form:

$$\bar{I}_{eq} = -\frac{(E^i_\theta \cos\theta^i \sin\phi^i + E^i_\phi \cos\phi^i)\, e^{jk(a\sin\theta^i\cos\phi^i + y'\sin\theta^i\sin\phi^i)}}{Z_0 \sin\beta_i \sin\beta_d} D_s(\psi,\psi') \sqrt{\frac{8\pi}{jk}}\, \hat{y} \tag{16}$$

$$\bar{M}_{eq} = -\frac{(E^i_\phi \cos\theta^i \sin\phi^i - E^i_\theta \cos\phi^i)\, e^{jk(a\sin\theta^i\cos\phi^i + y'\sin\theta^i\sin\phi^i)}}{\sin\beta_i \sin\beta_d} D_h(\psi,\psi') \sqrt{\frac{8\pi}{jk}}\, \hat{y} \tag{17}$$

where β_i, β_d, ψ and ψ' are as defined in Equations (9) and (10).

Substitution of Equations (16) and (17) into Equation (6) and defining the parameters for edge 3 one obtains

$$\bar{E}_3^{s1} = \frac{jk}{4\pi r} \frac{e^{-jkr}}{\sin\beta_i \sin\beta_d} \sqrt{\frac{8\pi}{jk}}$$

$$\left[\hat{\theta} \left[(\bar{E}_\theta^i \cos\theta^i \sin\phi^i \cos\theta \sin\phi + \bar{E}_\phi^i \cos\phi^i \cos\theta \sin\phi) D_s(\psi,\psi') \right. \right.$$

$$\left. + (\bar{E}_\phi^i \cos\theta^i \sin\phi^i \cos\phi - \bar{E}_\theta^i \cos\phi^i \cos\phi) D_h(\psi,\psi') \right]$$

$$+ \hat{\phi} \left[(\bar{E}_\theta^i \cos\theta^i \sin\phi^i \cos\phi + \bar{E}_\phi^i \cos\phi^i \cos\phi) D_s(\psi,\psi') \right.$$

$$\left. \left. + (-\bar{E}_\phi^i \cos\theta^i \sin\phi^i \cos\theta \sin\phi + \bar{E}_\phi^i \cos\theta^i \cos\theta \sin\phi) D_h(\psi,\psi') \right] \right]$$

$$\int_0^b e^{jk[a(\sin\theta^i \cos\phi^i + \sin\theta\cos\phi) + y'(\sin\theta^i \sin\phi^i + \sin\theta\sin\phi)]} \, dy' . \tag{18}$$

The contribution of edge 4 is similar to Equation (18). The total contribution from edges 3 and 4 for the backscatter case is given by

$$\bar{E}^{s1}_{34} = \frac{1}{\pi ks}\,\frac{e^{-jkr}}{\sin^2\beta_i}\,\frac{2\cos(ka\sin\theta^i\cos\phi^i)}{2\cos\psi}\,\frac{\sin(kb\sin\theta^i\sin\phi^i)}{\sin\theta^i\sin\phi^i}$$

$$e^{j\frac{ka}{2}\sin\theta^i\cos\phi^i}\; e^{j\frac{kb}{2}\sin\theta^i\sin\phi^i}$$

$$\left[\hat{\theta}\left[\bar{E}^i_\theta\cos^2\theta^i\sin^2\phi^i + E^i_\phi\cos\phi^i\sin\phi^i\cos\theta^i)\sin^2\frac{\psi}{2}\right.\right.$$

$$\left.-(E^i_\phi\cos\theta^i\cos\phi^i\sin\phi^i - E^i_\theta\cos^2\phi^i)\cos^2\frac{\bar{\psi}}{2}\right]$$

$$+\hat{\phi}\left[\bar{E}^i_\theta\sin\phi^i\cos\theta^i + E^i_\phi\cos\phi^i)\cos\phi^i\sin^2\frac{\psi}{2}\right.$$

$$\left.\left.+(E^i_\phi\cos^2\theta^i\sin\phi^i - E^i_\theta\cos\phi^i\sin\phi^i\cos\theta^i)\cos^2\frac{\bar{\psi}}{2}\right]\right] \quad . \quad (19)$$

For an observation scan in the x-z plane, where $\phi^i=0$, $\psi=\pi+\theta^i$, $\beta_i=\frac{\pi}{2}$, one obtains

$$\bar{E}^{s1}_{34} = -\frac{e^{-jkr}}{\pi r}\,e^{j\frac{ka}{2}\sin\theta^i}\,\frac{\cos(ka\sin\theta^i)}{\cos\theta^i}\,b\left[\hat{\phi}E^i_\phi\cos^2\frac{\theta^i}{2} + \hat{\theta}\,E^i_\theta\sin^2\frac{\bar{\theta^i}}{2}\right]. \quad (20)$$

iii.) Double diffraction from vertical edges in the case of x-z plane scan.

The singly diffracted rays from edges 3 or 4 will travel across the aperture and diffract once more at the other end of the aperture before going back to the receiver. Since in the x-z plane scan case, there is a continuum of doubly diffracted rays, the ECM is employed to obtain their contributions.

Let $\bar{E}_{43}$, $\bar{H}_{43}$ be the electric and magnetic fields in $\hat{y}$-direction incident on the fourth edge due to the diffraction from third edge, then one obtains

$$\bar{E}_{43} = \hat{y}\, E_{\phi}^{i} \text{ (at edge 3) } D_s(\psi'=\pi+\theta^i,\ \psi=\tfrac{\pi}{2}) \frac{e^{-jka+jk\frac{a}{2}\sin\theta^i}}{\sqrt{a}} \qquad (21)$$

and

$$\bar{H}_{43} = -\hat{y}\, Y_o E_{\theta}^{i} \text{ (at edge 3) } D_h(\psi'=\pi+\theta^i,\ \psi=\tfrac{\pi}{2}) \frac{e^{-jka+jk\frac{a}{2}\sin\theta^i}}{\sqrt{a}}. \qquad (22)$$

This field $\bar{E}_{43}$ is incident on edge 4, diffracts from edge 4 and constitutes a part of the total doubly diffracted field. For the backscatter case, these doubly diffracted fields have a caustic; therefore, one needs to utilize the ECM to obtain a bounded result. The equivalent electric and magnetic currents are given by

$$\bar{I}_{eq}^{34} = -\frac{\hat{y} \cdot \bar{E}_{43}\, D_s(\psi'=\frac{\pi}{2},\ \psi=\pi-\theta^i)}{Z_o} \sqrt{\frac{8\pi}{jk}}\ \hat{y} \quad , \text{ and} \qquad (23)$$

$$\bar{M}_{eq}^{34} = -\frac{\hat{y} \cdot \bar{H}_{43}\, D_h(\psi'=\frac{\pi}{2},\ \psi=\pi-\theta^i)}{Y_o} \sqrt{\frac{8\pi}{jk}}\ \hat{y} \tag{24}$$

the doubly diffracted fields from these equivalent sources are given by the integral of Equation (6) such that

$$\bar{E}_4^{s2} = \frac{jk}{4\pi}\frac{e^{-jkr}}{r}\left[\hat{y}\, E_\phi^i\, D_s(\psi'=\pi+\theta^i,\ \psi=\tfrac{\pi}{2})\, D_s(\psi'=\tfrac{\pi}{2},\ \psi=\pi-\theta^i)\right.$$

$$\left. + \hat{\theta}\, E_\theta^i\, D_h(\psi'=\pi+\theta^i, \psi=\tfrac{\pi}{2})\, D_h(\psi'=\tfrac{\pi}{2},\ \psi=\pi-\theta^i)\right] b\,\frac{e^{-jka}}{\sqrt{a}}\sqrt{\frac{8\pi}{jk}} \tag{25}$$

The doubly diffracted fields due to diffractions at edges 4 and 3, respectively, are given by similar expressions. The total doubly diffracted field is found by adding these two contributions such that

$$\bar{E}_{34}^{s2} = \frac{e^{-jkr}}{r}\,\frac{be^{-jka}}{\sqrt{\pi jk\,\frac{a}{2}}}\,\frac{1}{\cos^2\theta^i}\left[\hat{y}\, E_\phi^i \cos^2\frac{\theta^i}{2} - \hat{\theta} E_\theta^i \sin^2\frac{\theta^i}{2}\right]. \tag{26}$$

In addition to doubly diffracted rays, there are multiply diffracted rays at the aperture. The analysis of multiple diffractions can be done in general by the GTD, provided that all multiply diffracted fields are ray optical. As is well known, the GTD diffracted fields are not ray optical in the transition regions [4]. In the case considered here one vertical edge is exactly on the reflection shadow boundary of the other edge, where it has to match the discontinuity of the GO (Geometrical Optics) field. Since it is exactly on the shadow boundary, one can

decompose the diffracted field into two ray-optical fields as done previously [5]. The subsequent (double) diffration of these two ray optical components of the singly diffracted fields can be done via conventional application of the GTD. The evaluation of the third order diffraction follows similarly and is given by;

$$\bar{E}^{s3}_{34} = -\frac{e^{-jkr}}{r}\,\frac{be^{-jk2a}}{2\pi\sqrt{\pi jka}}\left[\hat{y}\,E^i_\phi - \frac{\cos^2\frac{\theta^i}{2}}{\cos^2\theta^i} - \hat{\theta}\,E^i_\theta\,\frac{\sin^2\frac{\theta^i}{2}}{\cos^2\theta^i}\right]$$

$$\cos(ka\sin\theta^i)\; e^{jka\sin\theta^i} \qquad (27)$$

The higher-order diffractions, beyond the third-order term, are not considered here because they are very weak in comparison to the lower order terms just analyzed.

iv.) Numerical results for Chapter III

To check the validity of the analysis, the calculated results are compared with a set of measurements obtained using the Compact Range Facility at ElectroScience Laboratory, the Ohio State University. The measurements are done on an inlet model as shown in Figures 1 and 2. In order to remove the interior cavity effects, the inner surface of the back wall of the inlet is covered with absorbing material. Two sets of measurement results are obtained.

a.) At a fixed frequency, the aspect angle (θ) from the z-axis is varied in the horizontal (or vertical) plane from 0 to 90 degrees.

b.) At a fixed aspect angle in the horizontal (or vertical) plane the frequency response is measured, starting from 8 GHz up to 12 GHz at 10 MHz steps. Therefore a bandlimited frequency response is obtained. Then, this response is processed through a Kaiser-Bessel window, and its inverse Fourier Transform is obtained using an FFT algorithm which represents a time domain response. Since the measured spectrum is bandlimited, the time domain response represents the impulse response of the target which is convolved with

$$\frac{2}{\pi} \frac{\sin\omega_b t}{t} \cos\omega_o t \tag{28}$$

where ω_b=half-bandwidth (2 GHz) and ω_o is the center frequency which is 10 GHz in this case.

The measured and calculated radar cross sections (RCS) versus the aspect angle are shown in Figures 5 through 16 for different polarizations and frequencies. In each figure measurements (solid line) and calculations (dashed line) are drawn on the same scale of dB over m^2. Figures 5 through 10 correspond to a horizontal (x-z) scan; whereas, Figures 11 through 16 correspond to a vertical (y-z) scan. In both the horizontal and vertical scans, the radar cross section is measured and analyzed for two polarizations ($\hat{\phi}$ and $\hat{\theta}$). Finally, each case is repeated at three different frequencies, namely around 8, 10 and 12 GHz. In both the horizontal and vertical scans, a $\hat{\phi}$ directed incident electric field will not diffract from two edges which are parallel to the scan plane. Therefore the contribution to the radar cross section in these cases is dominated by the diffracted fields from

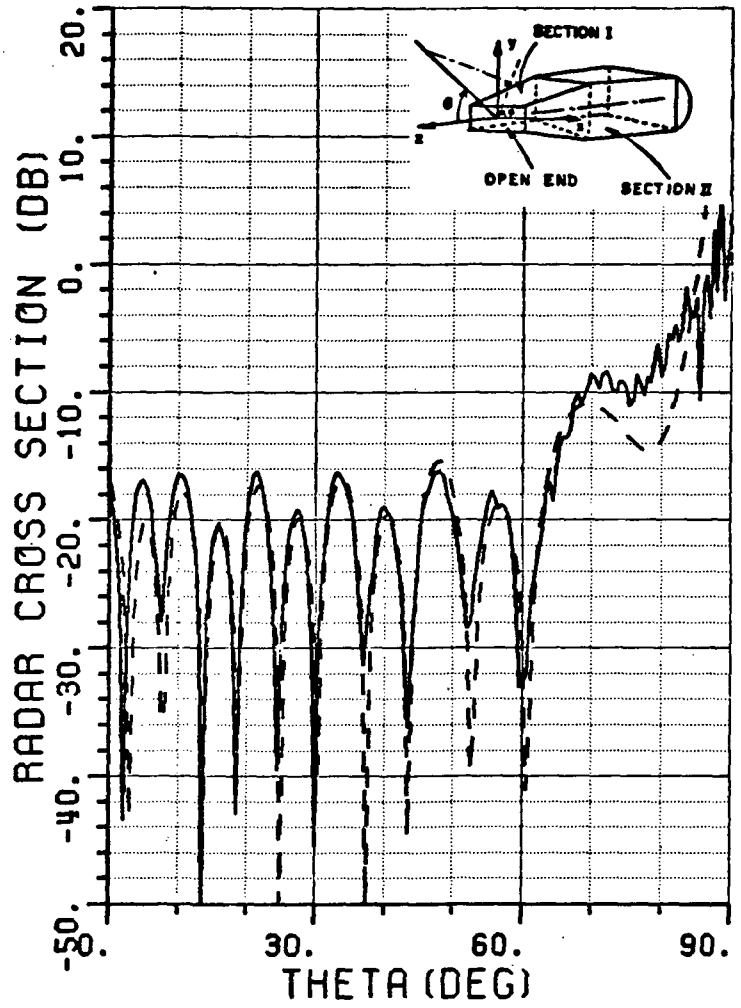


Figure 5. Aspect angle scan in horizontal (x-z) plane. Vertical ($\hat{\phi}$) polarization, frequency = 8.02 GHz.
—— measured, --- calculated results.

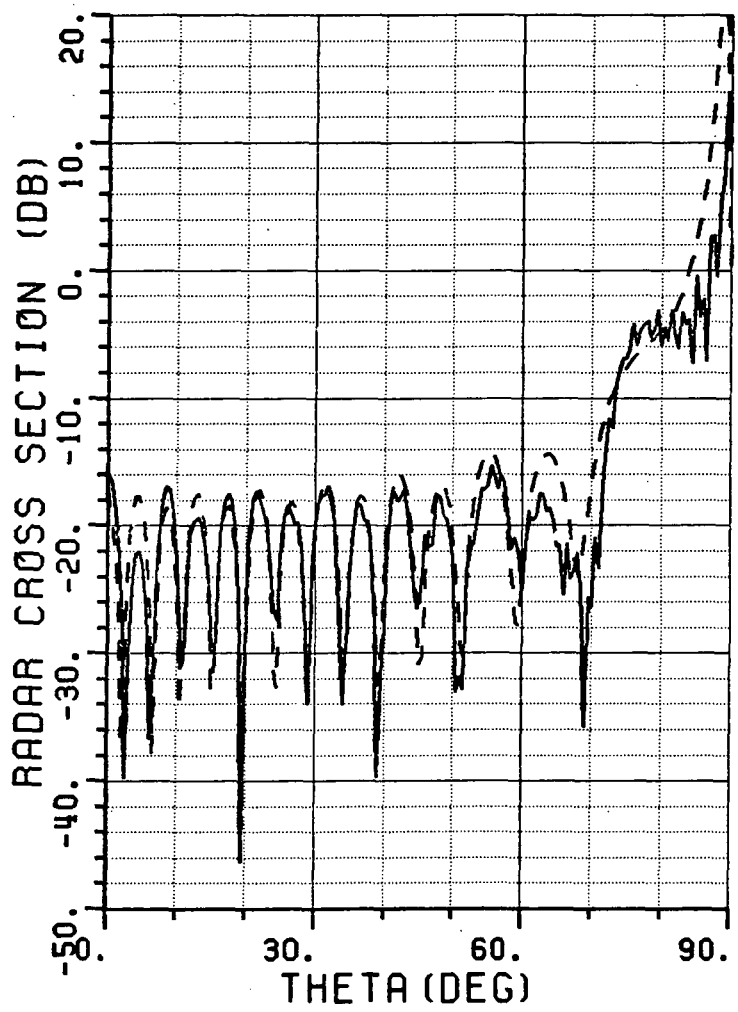


Figure 6. Aspect angle scan in horizontal (x-z) plane. Vertical ($\hat{\phi}$) polarization, frequency = 9.98 GHz.
___ measured, --- calculated results.

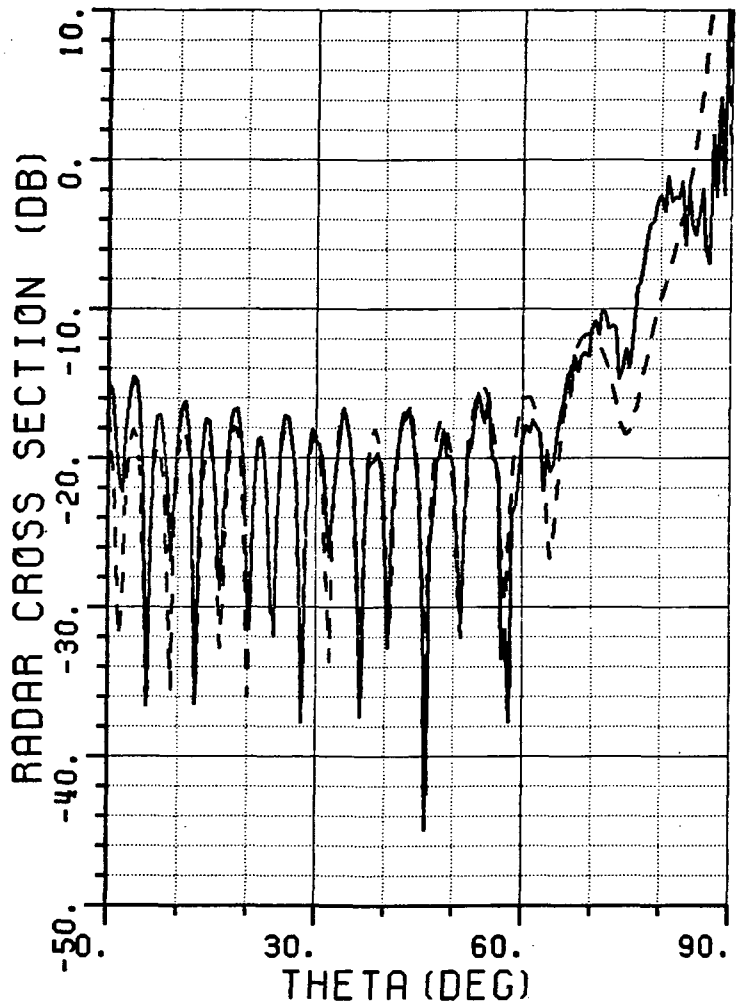


Figure 7. Aspect angle scan in horizontal (x-z) plane. Vertical ($\hat{\phi}$) polarization, frequency = 11.95 GHz.
___ measured, --- calculated results.

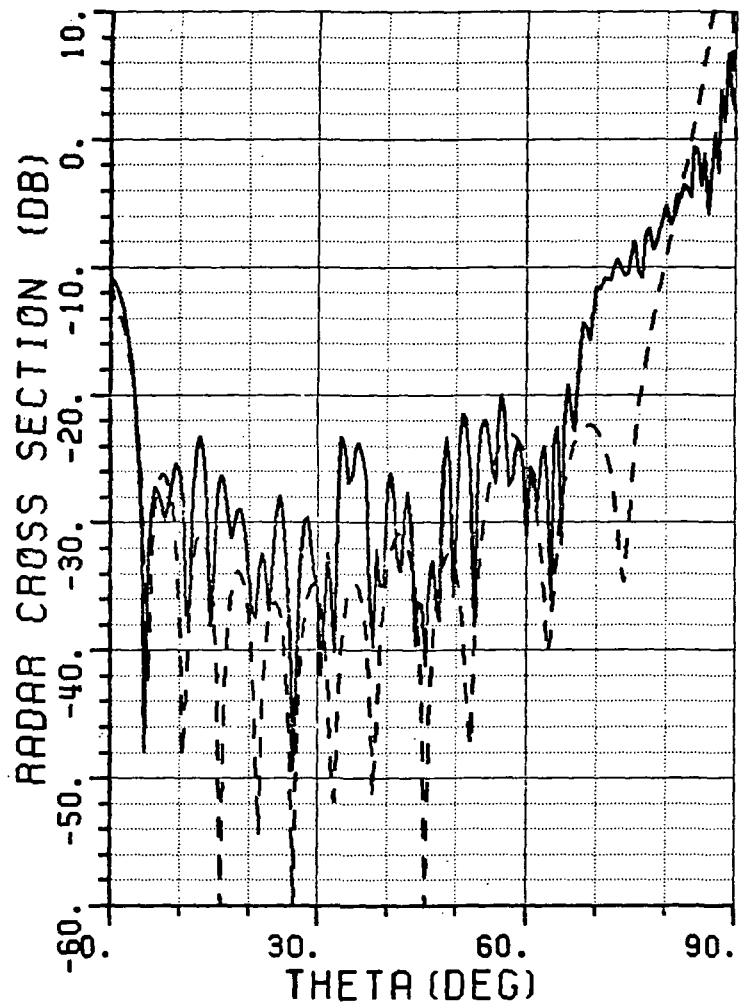


Figure 8. Aspect angle scan in horizontal (x-z) plane. Horizontal ($\hat{\theta}$) polarization, frequency = 8.02 GHz.
—— measured, --- calculated results.

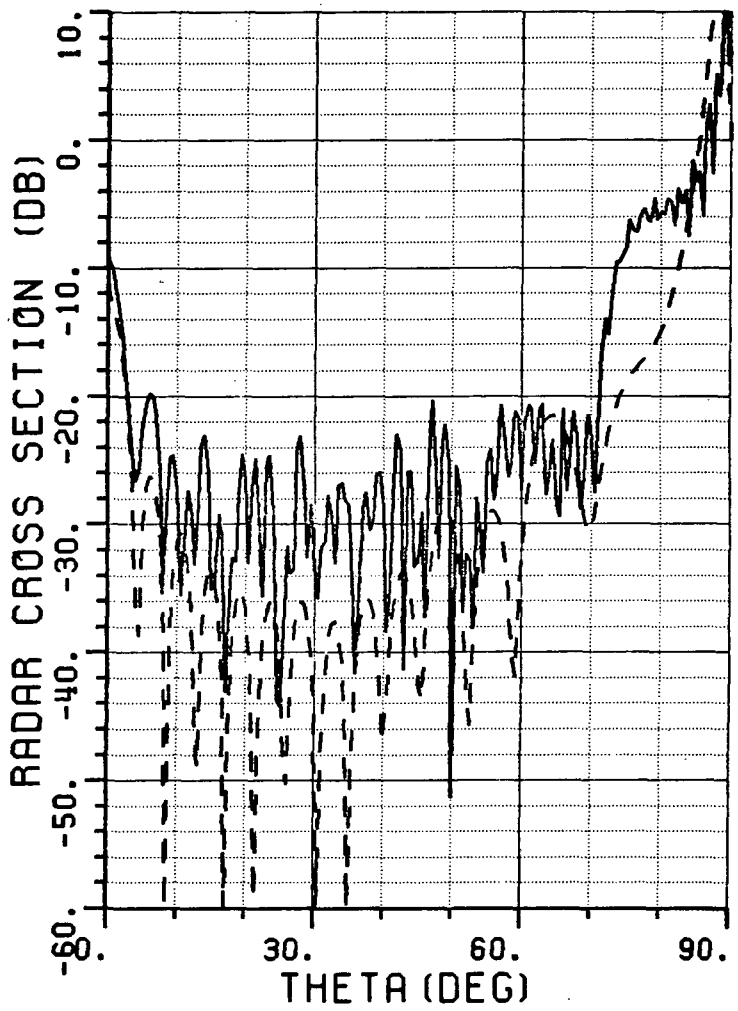


Figure 9. Aspect angle scan in horizontal (x-z) plane. Horizontal ($\hat{\theta}$) polarization, frequency = 9.98 GHz.
—— measured, --- calculated results.

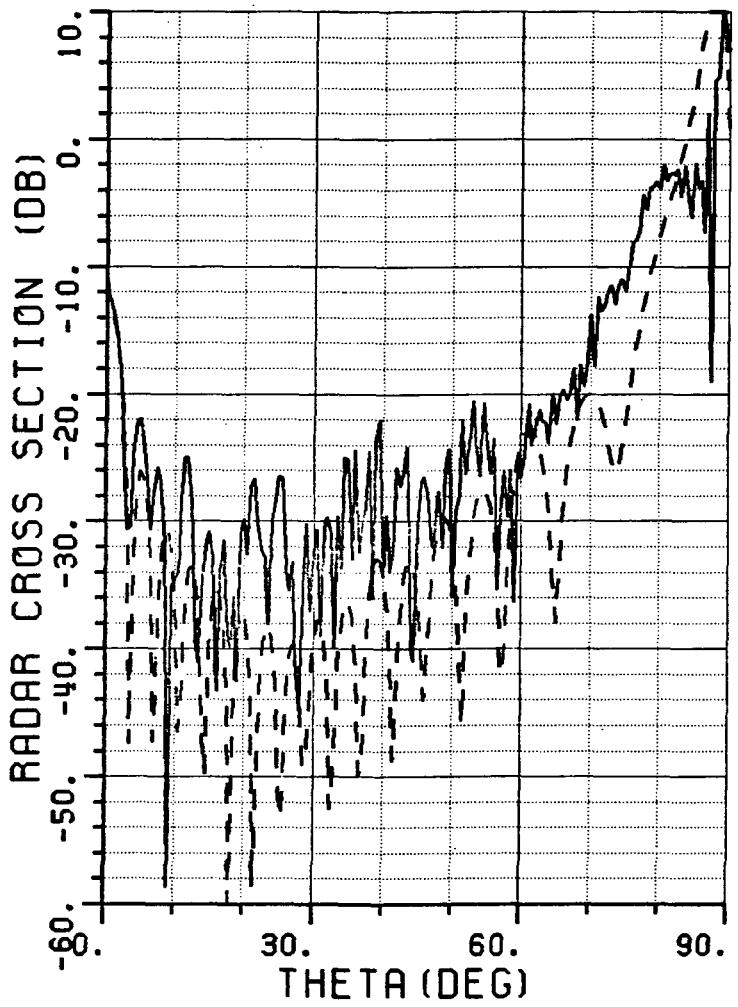


Figure 10. Aspect angle scan in horizontal (x-z) plane. Horizontal ($\hat{\theta}$) polarization, frequency = 11.95 GHz.
—— measured, --- calculated results.

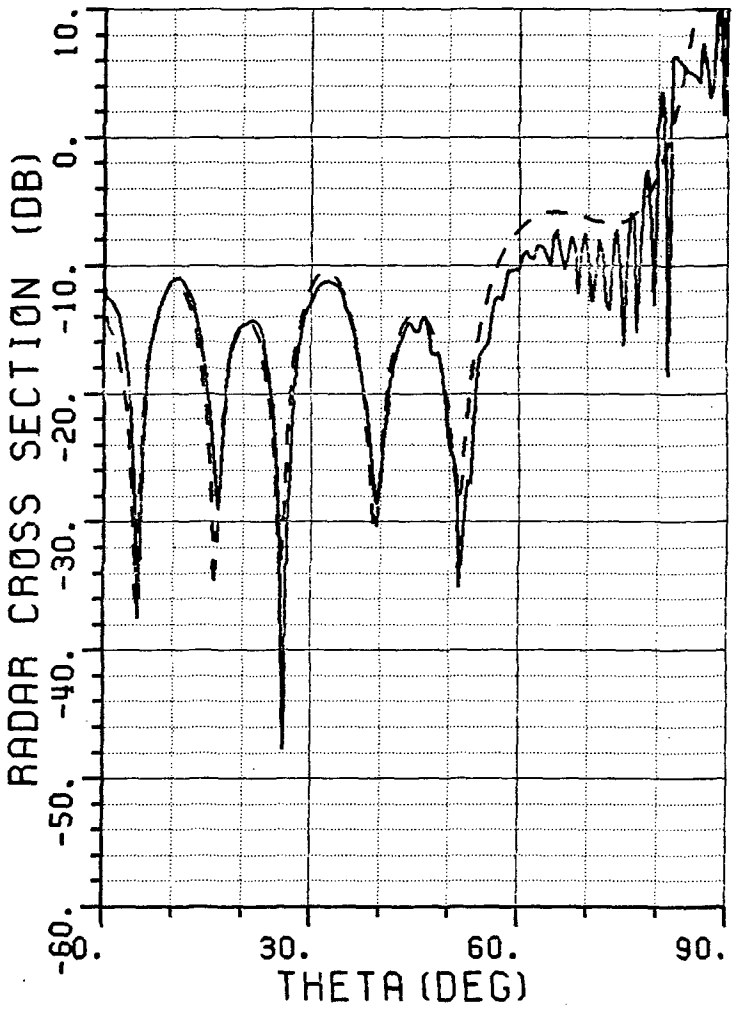


Figure 11. Aspect angle scan in vertical (y-z) plane. Horizontal ($\hat{\phi}$) polarization, frequency = 8.02 GHz.
—— measured, --- calculated results.

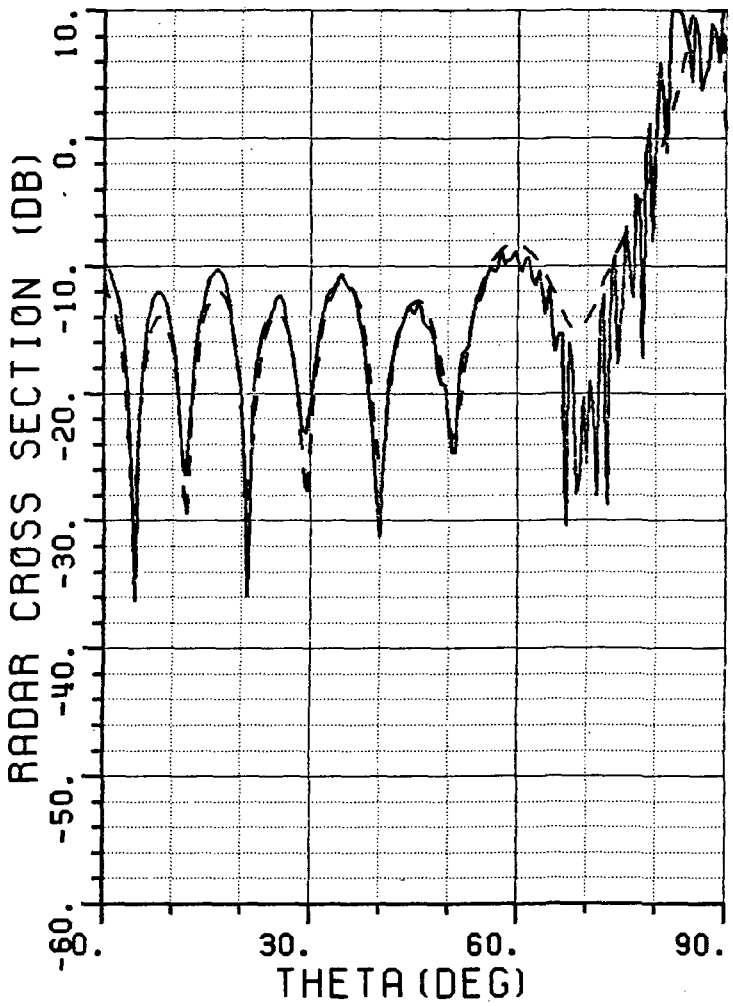


Figure 12. Aspect angle scan in vertical (y-z) plane. Horizontal ($\hat{\phi}$) polarization, frequency = 9.98 GHz.
—— measured, --- calculated results.

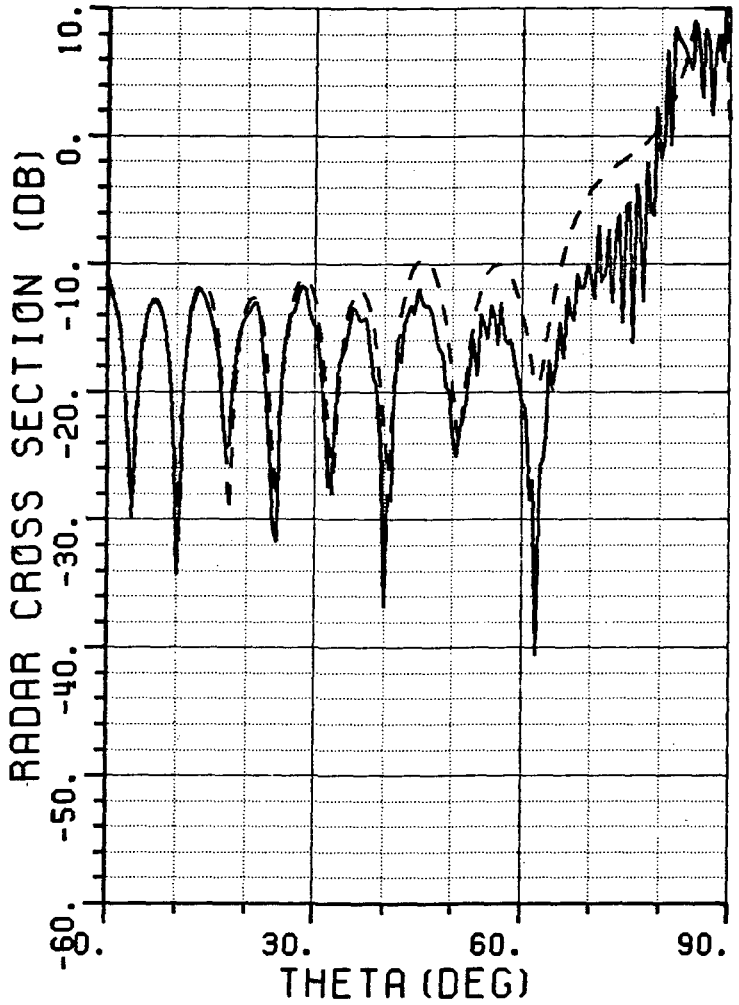


Figure 13. Aspect angle scan in vertical (y-z) plane. Horizontal ($\hat{\phi}$) polarization, frequency = 11.95 GHz.
—— measured, --- calculated results.

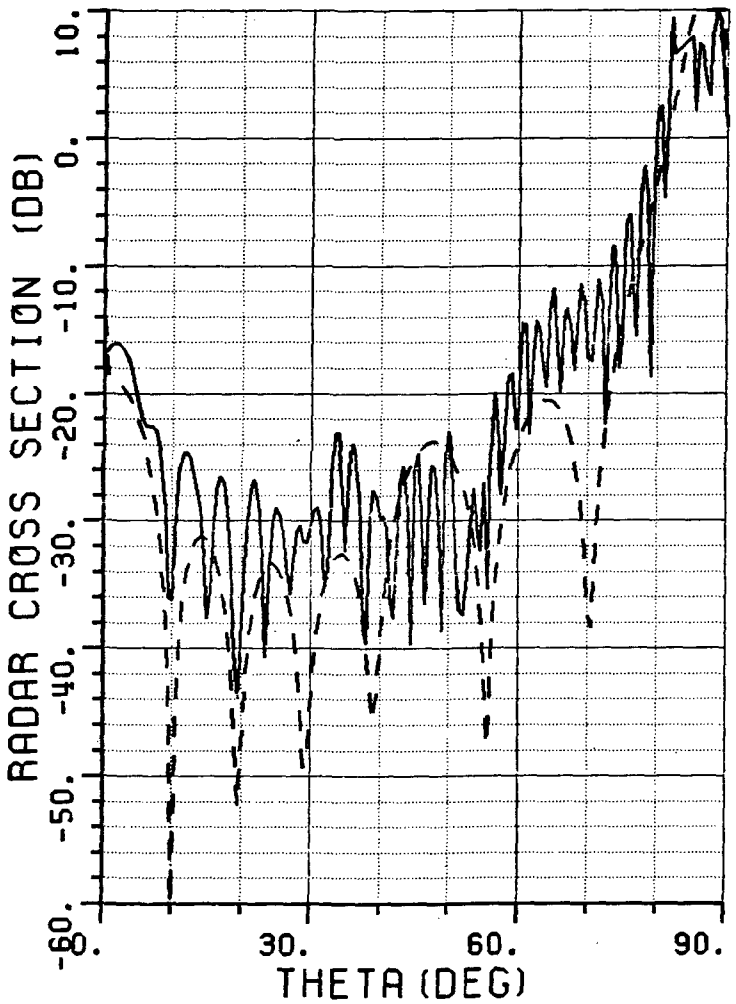


Figure 14. Aspect angle scan in vertical (y-z) plane. Vertical ($\hat{\theta}$) polarization, frequency = 8.02 GHz.
—— measured, --- calculated results.

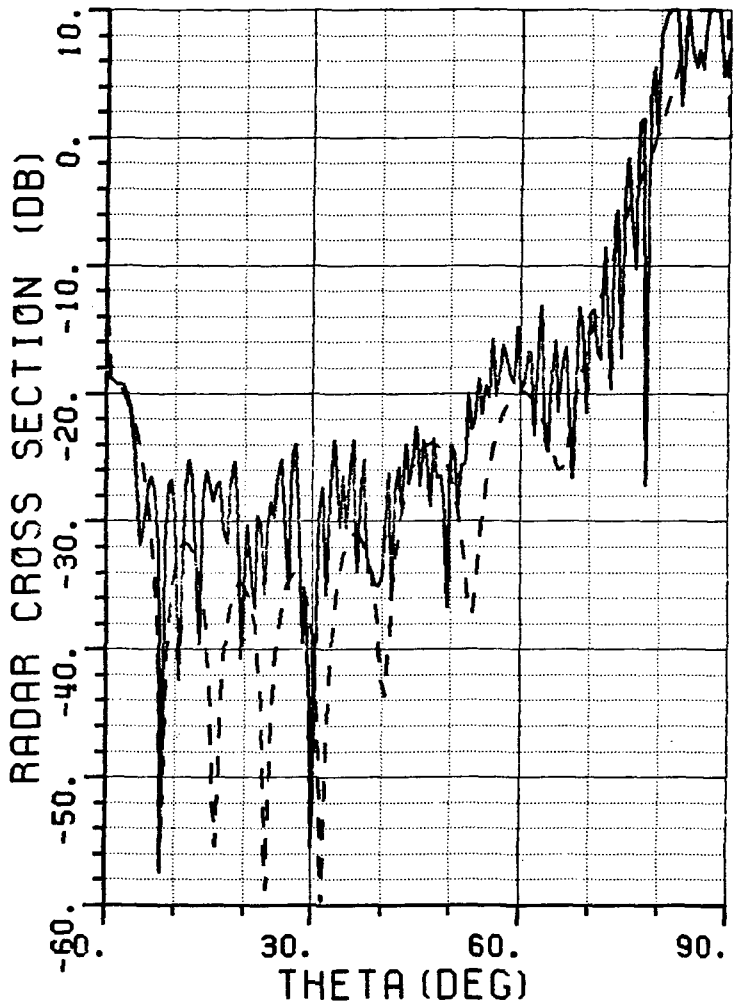


Figure 15. Aspect angle scan in vertical (y-z) plane. Vertical ($\hat{\theta}$) polarization, frequency = 9.98 GHz.
—— measured, --- calculated results.

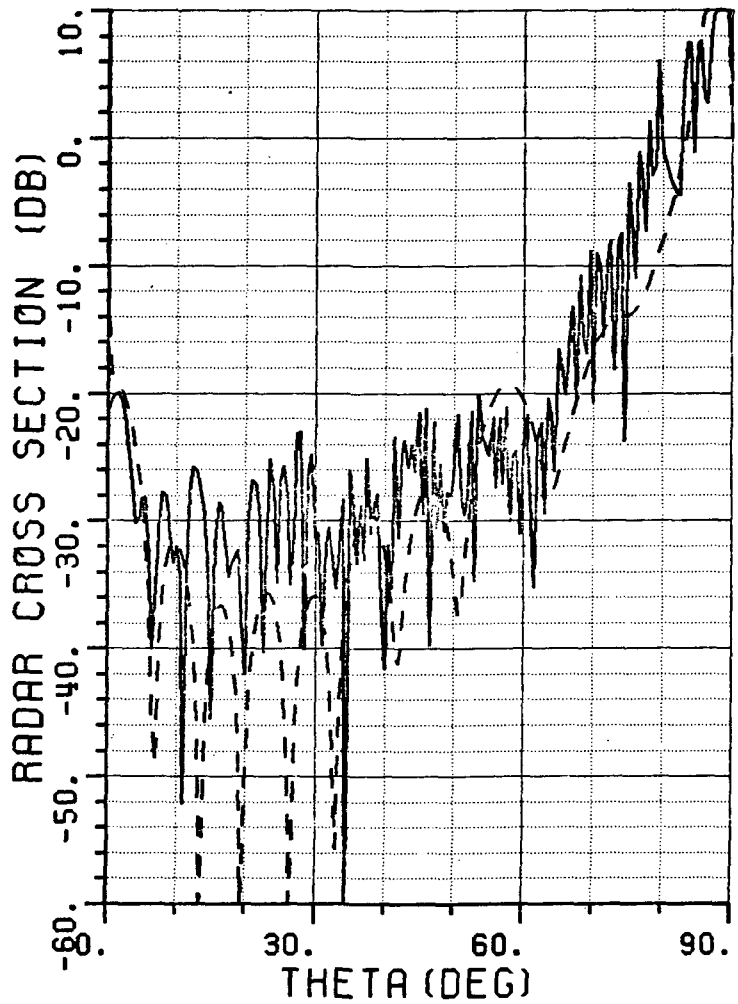


Figure 16. Aspect angle scan in vertical (y-z) plane. Vertical ($\hat{\theta}$) polarization, frequency = 11.95 GHz.
___ measured, --- calculated results.

the remaining two edges. As shown in Figures 5 through 7 and 11 through 13, the calculations agree reasonably well with the measurements. However, for the other polarization ($\hat{\theta}$), all four edges of the open end contribute to the radar cross section; however the contribution from two of these four edges reduces essentially to that from the end points (or corners). As shown in Figures 8 through 10 and 14 through 16, the agreement between the measured and calculated results is not as good as the $\hat{\phi}$-polarization case, especially the horizontal scan. The reason for this discrepancy will become clearer after discussing the frequency domain responses, suffice it to say for now that it is due to the imperfections of the model.

Finally one notes that the rim scattering analysis performed here is valid for aspect angles away from the shadow boundaries of the diffracted field. For aspect angles close to the shadow boundaries of the edges (θ close to 90 degrees) the approach described here should be modified; this modification will not be given here.

Frequency scans are done in the horizontal (ϕ=0) plane, with two different polarizations and with the angle θ fixed at four different values, namely 0, 15, 30 and 45 degrees. The measured (solid line) and calculated (dashed line) radar cross section results are plotted on the same graph and given in dB over m^2. The phase variation of the radar cross section is also shown in the figures. To be able to make a phase comparison, the measured data has been processed so that the two results have the same phase center. The frequency spectra are then inverse

Fourier transformed to obtain the time domain responses. As explained before the time domain response is not an impulse response although it has been denoted like that on the plot for ease in understanding. Therefore, to make the comparison easier, the curves corresponding to measured and calculated time domain returns are shifted by equal amount from the center line. The scale in the time domain is dimensionless and should be taken as a relative scale. Finally, due to the malfunctions of electronic instrument during measurements, there are some glitches in the measured data. They are kept as they appeared originally, since their presence does not effect the overall characteristic of the curves.

As in the case of aspect angle scans, the amplitude and phase of the measured and calculated RCS results are in good agreement especially for a $\hat{\phi}$ polarized field (Figures 17 through 20). Also, it can be seen from the time domain plots that almost all of the measured return is from the rim at the open end. The absorber put at the back of the line very effectively removed any internal cavity effects.

In the case of the horizontal ($\hat{\theta}$) polarization, (Figures 21 through 24) the time domain plots show a relatively large return occuring later in time than the return from the open end. The variation of the position of that return with different θ values implies that it is coming from the external surfaces of the inlet model. Therefore as shown in Figures 22 through 24, the comparison between calculated and measured radar cross section results is not good. This also explains the discrepancy in the aspect angle scan results of Figures 8 through 10.

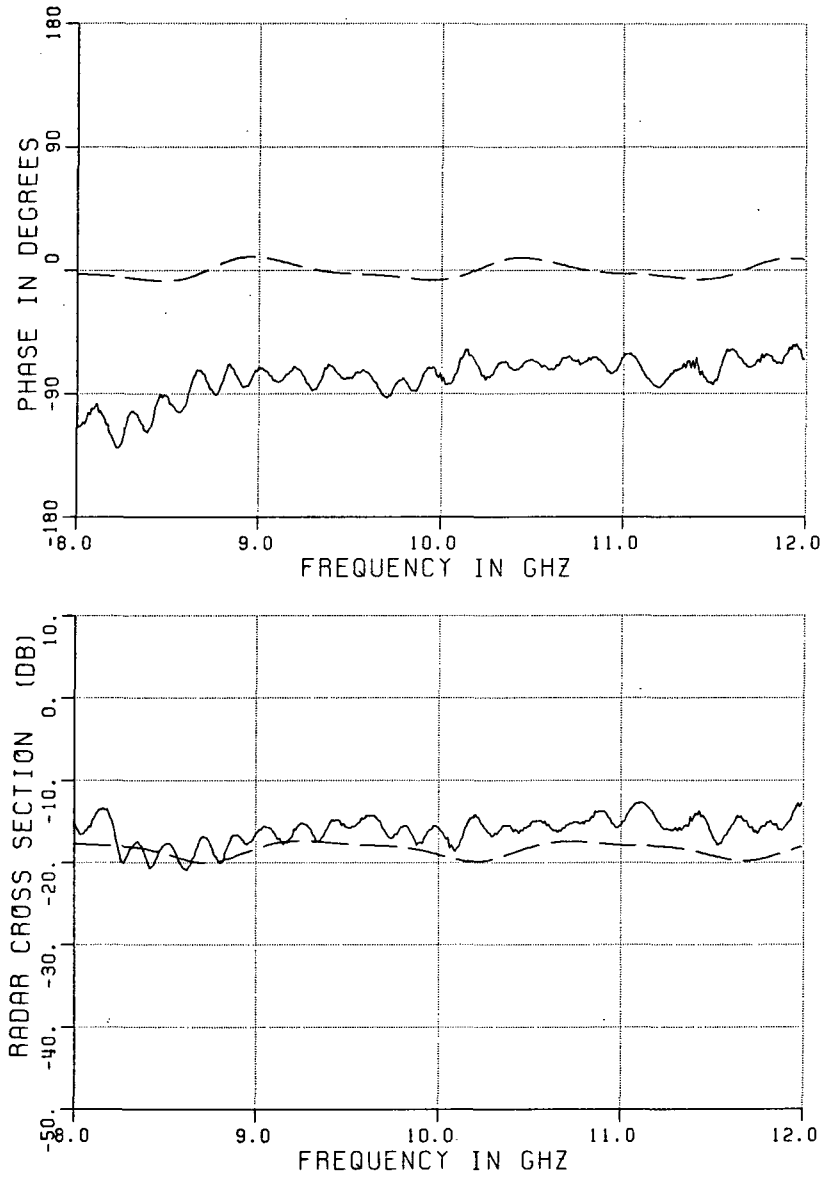


Figure 17a. Frequency scan in horizontal (x-z) plane. ϕ=0°, θ=0°, vertical ($\hat{\phi}$) polarization. ___ measured, --- calculated results.

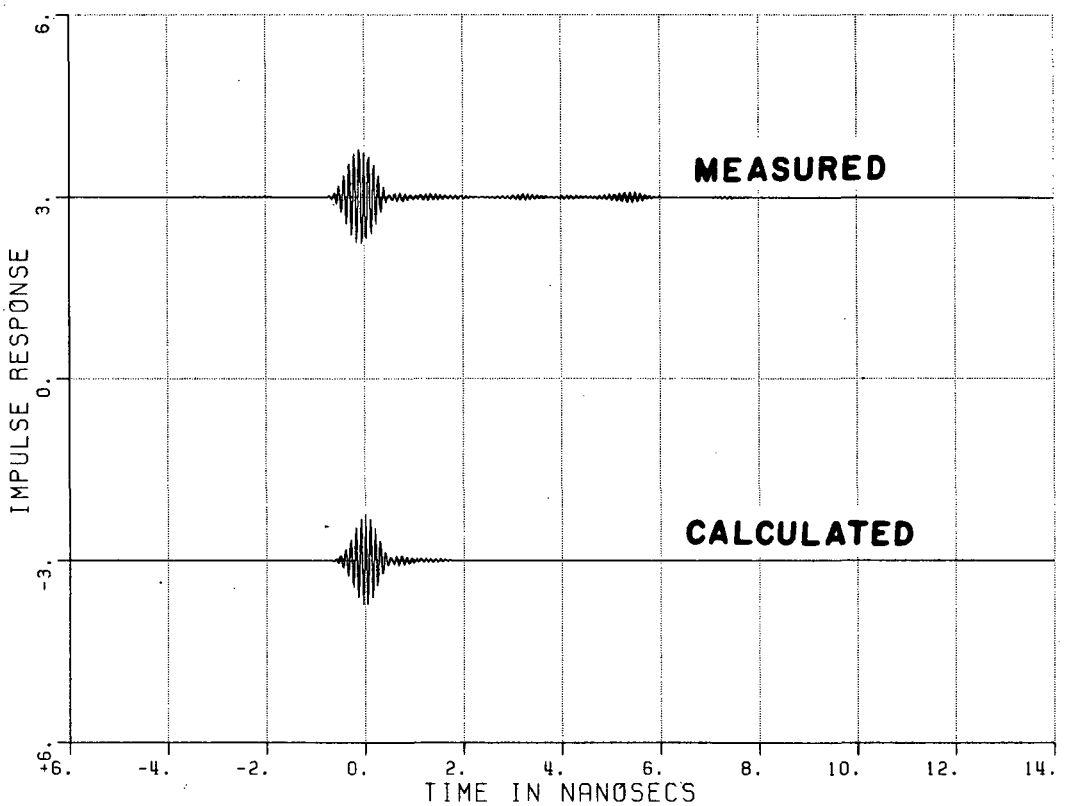


Figure 17b. Inverse Fourier transforms.

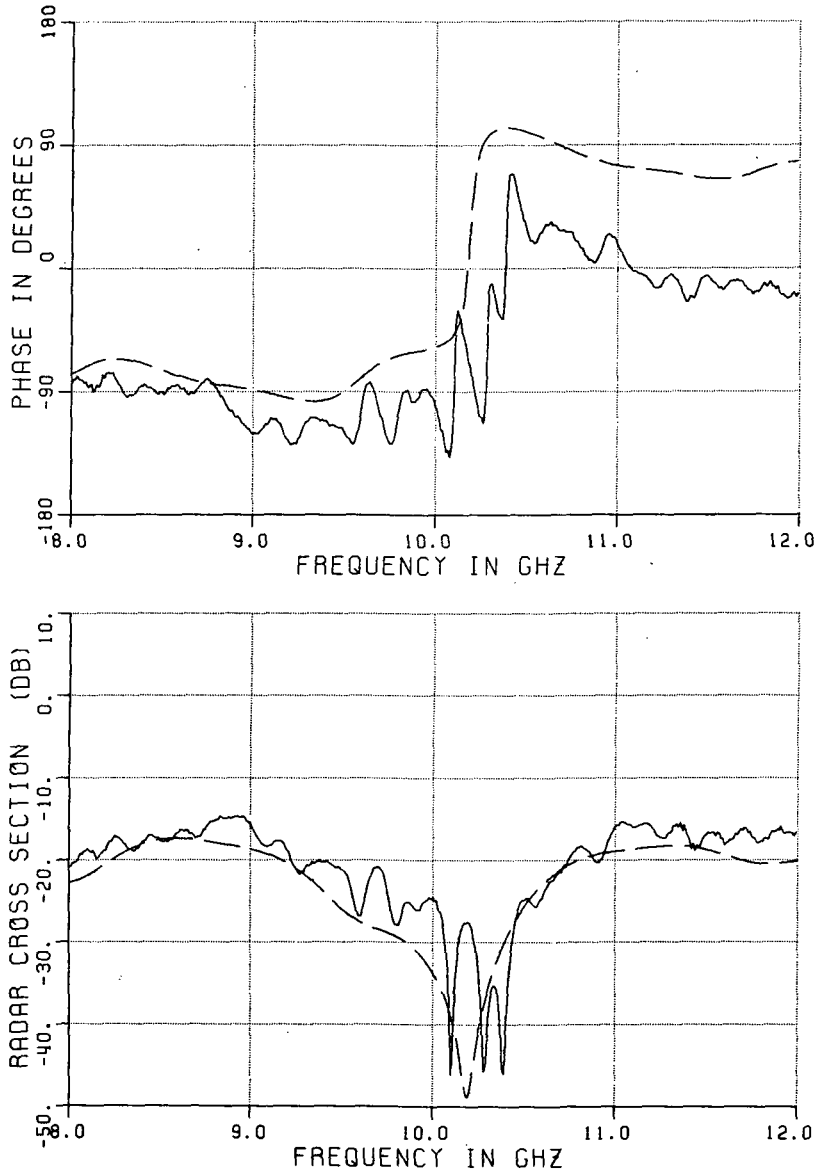


Figure 18a. Frequency scan in horizontal (x-z) plane. ϕ=0°, θ=15°, vertical ($\hat{\phi}$) polarization. ___ measured, --- calculated results.

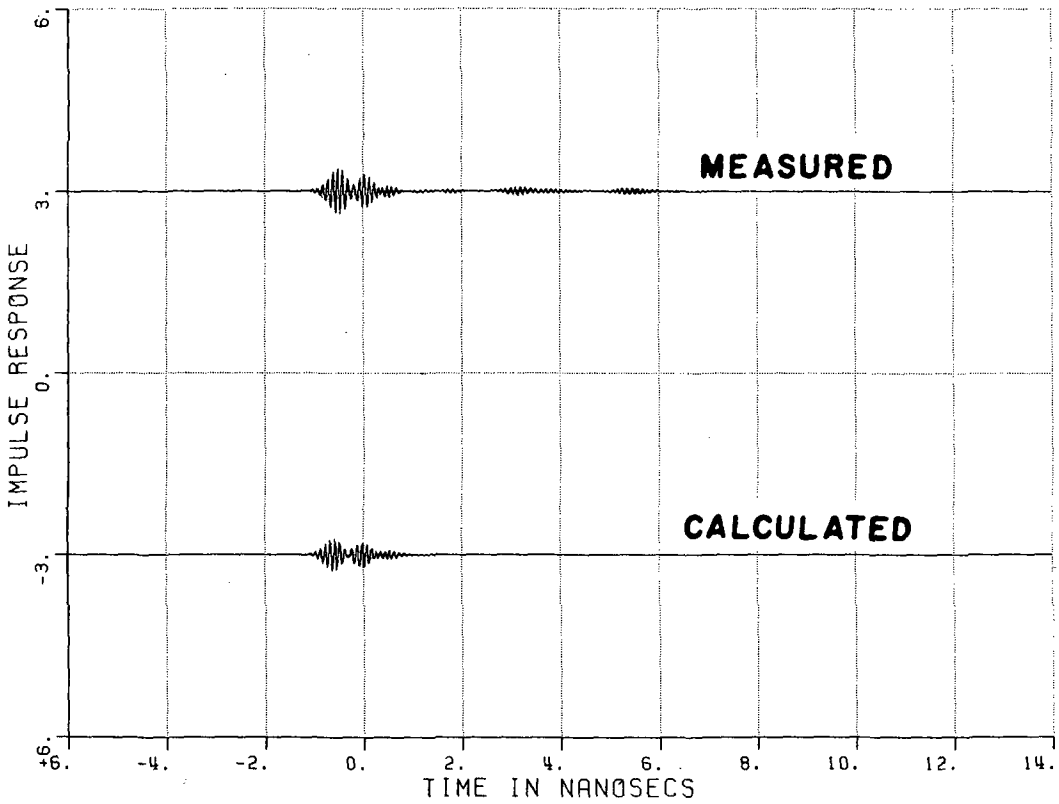


Figure 18b. Inverse Fourier transforms.

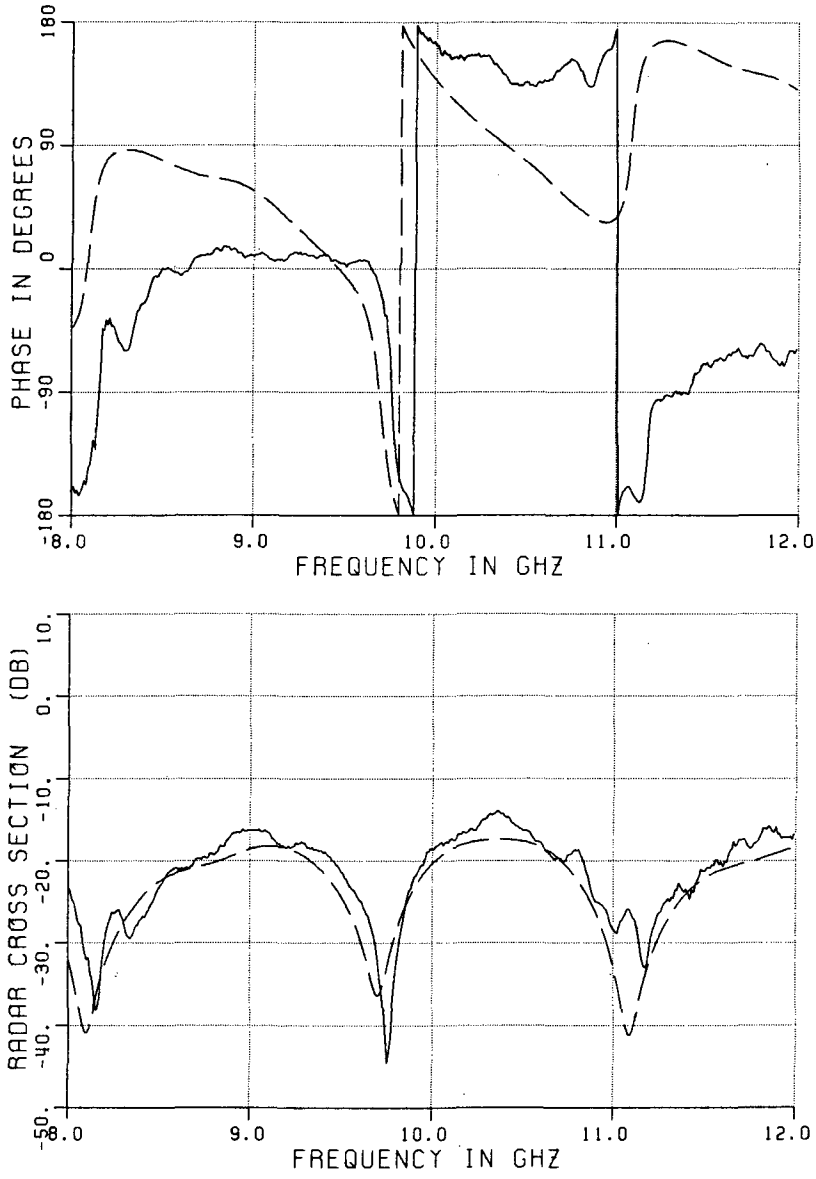


Figure 19a. Frequency scan in horizontal (x-z) plane. ϕ=0°, θ=30°, vertical ($\hat{\phi}$) polarization. ___ measured, --- calculated results.

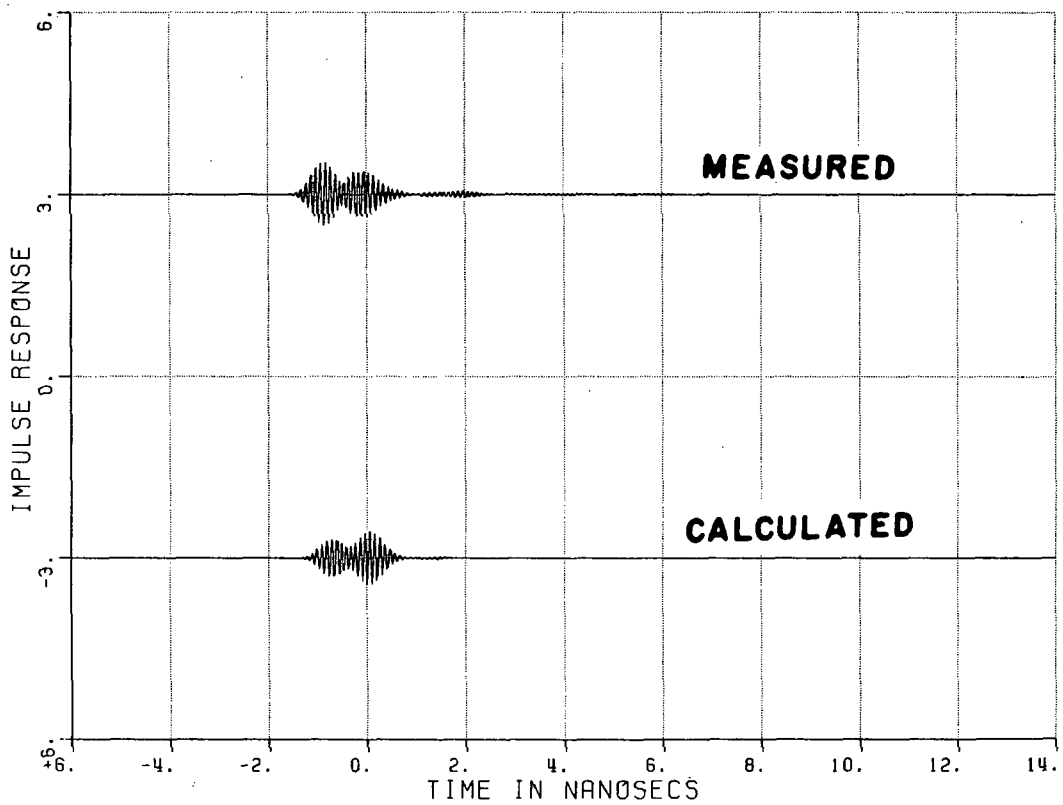


Figure 19b. Inverse Fourier transforms.

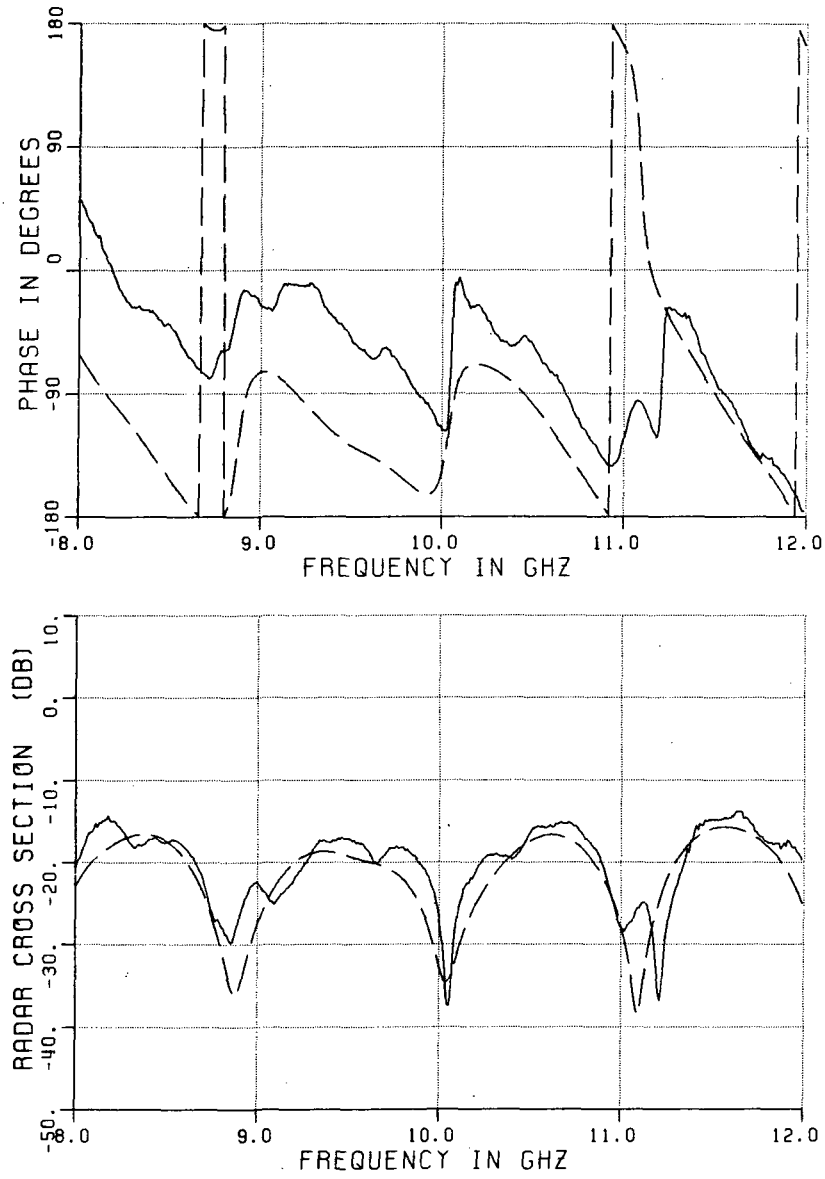


Figure 20a. Frequency scan in horizontal (x-z) plane. ϕ=0°, θ=45°, vertical ($\hat{\phi}$) polarization. ___ measured, --- calculated results.

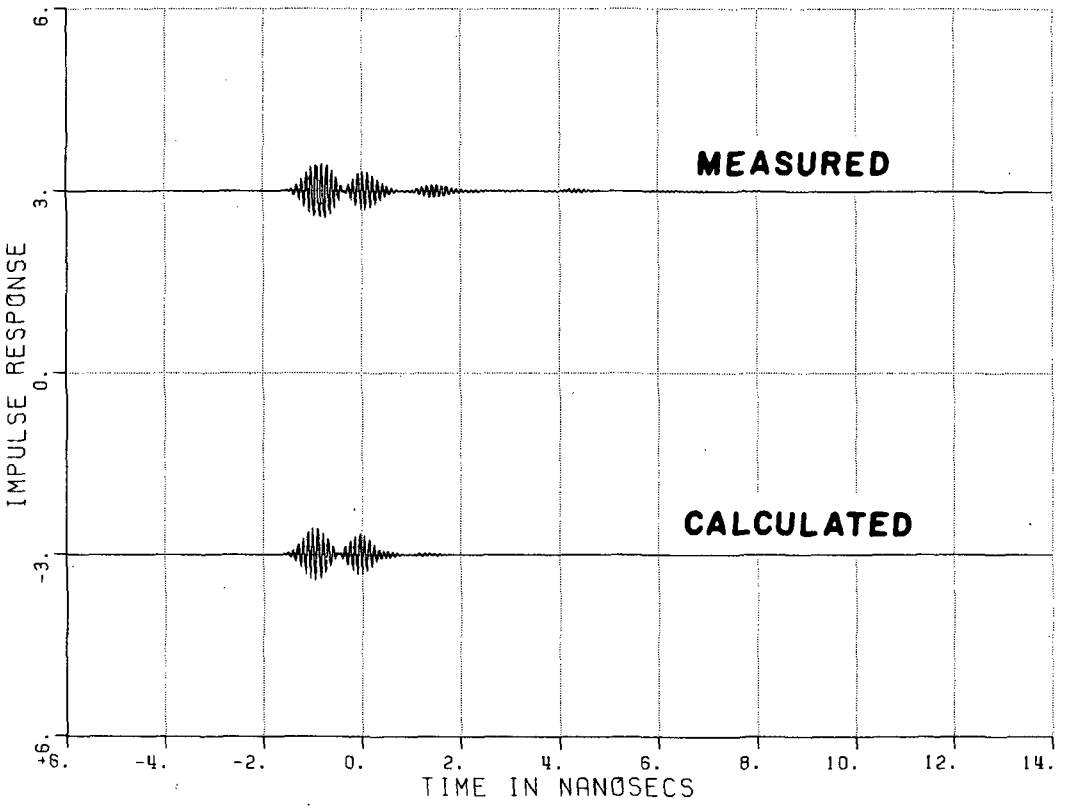


Figure 20b. Inverse Fourier transforms.

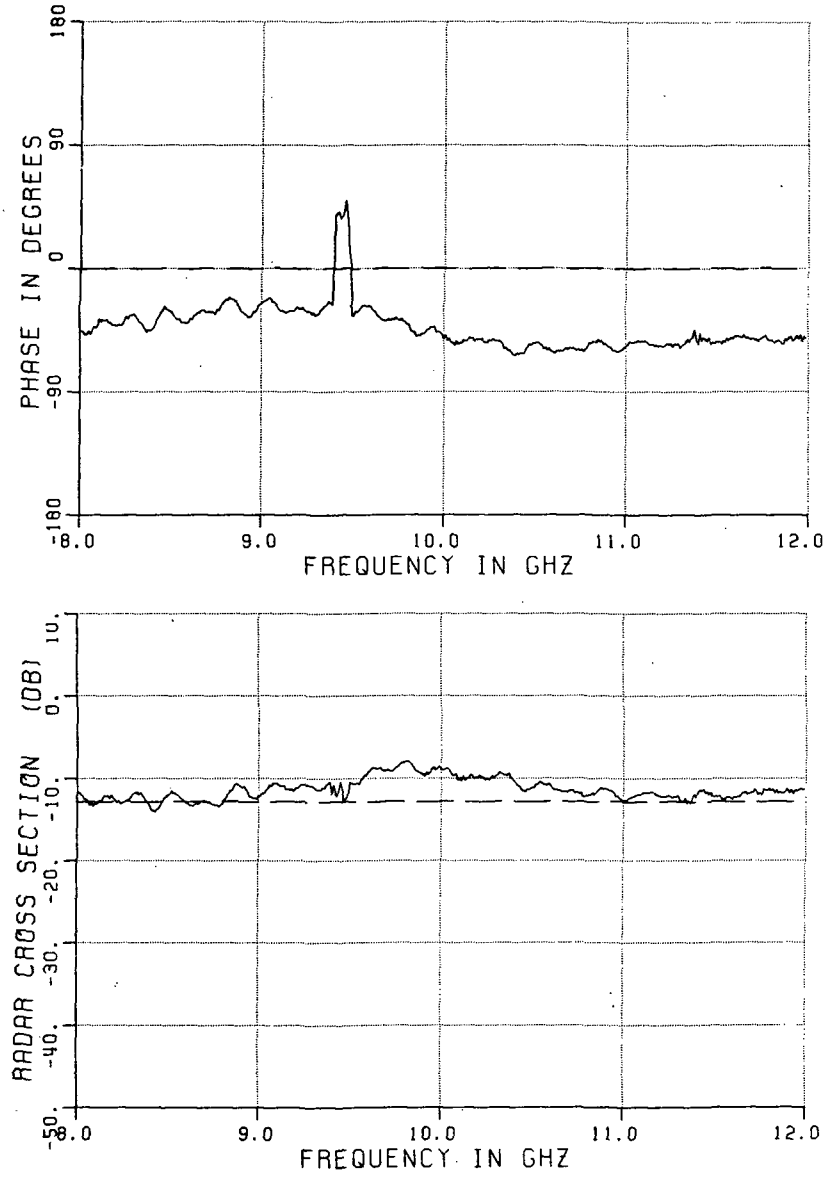


Figure 21a. Frequency scan in horizontal (x-z) plane. ϕ=0°, θ=0°, horizontal ($\hat{\theta}$) polarization. —— measured, --- calculated results.

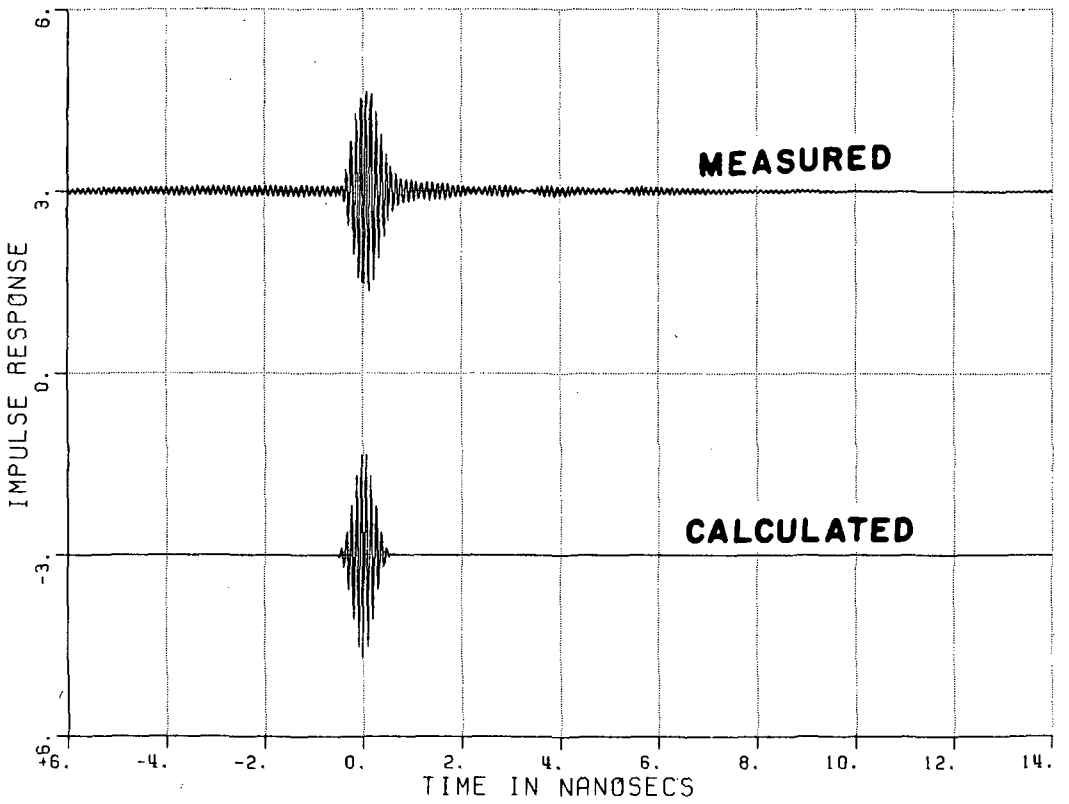


Figure 21b. Inverse Fourier transforms.

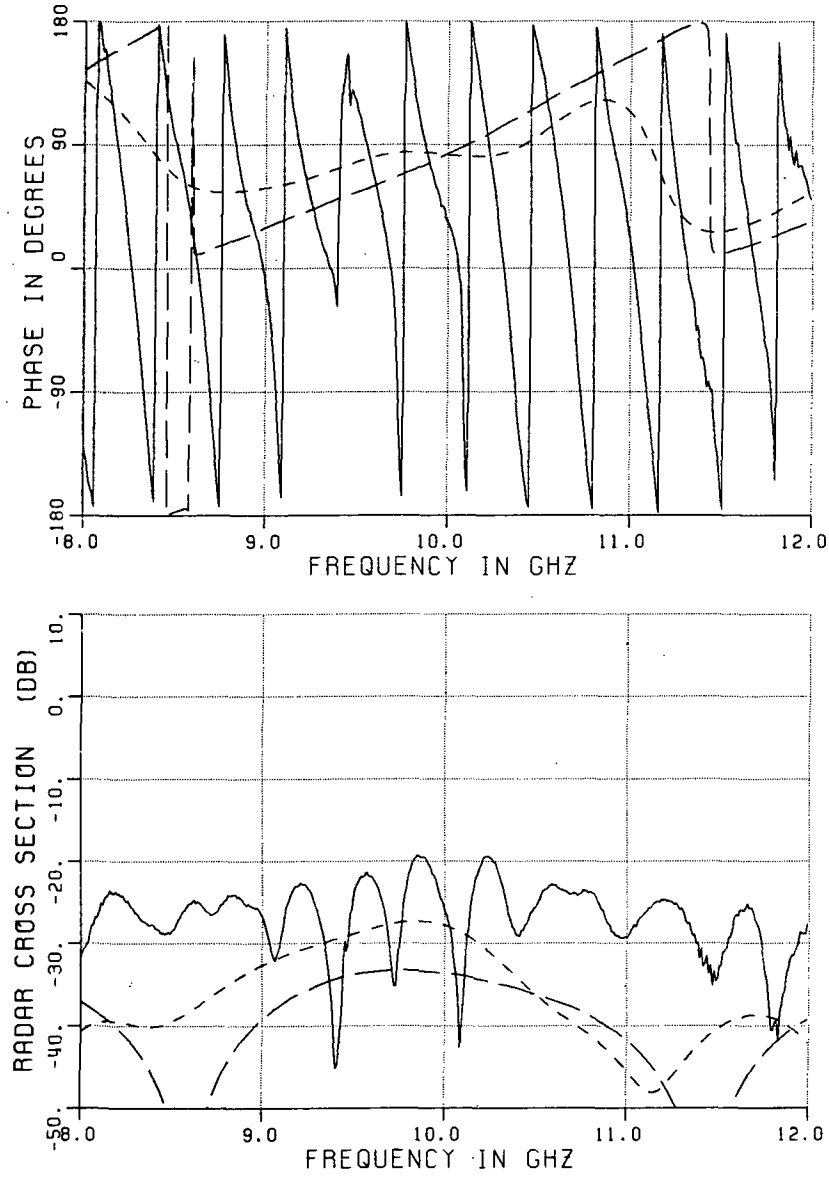


Figure 22a. Frequency scan in horizontal (x-z) plane.
ϕ=0°, θ=15°, horizontal ($\hat{\theta}$) polarization.
——— measured, — — calculated,
---- measured (time gated) results.

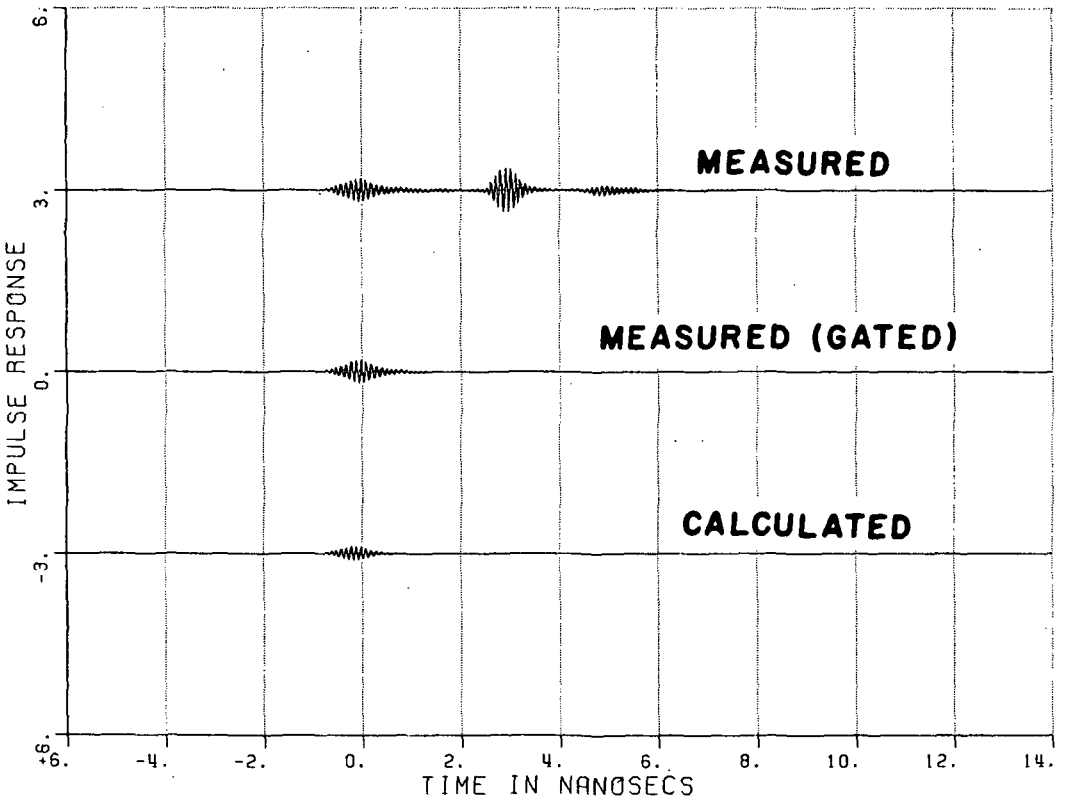


Figure 22b. Inverse Fourier transforms.

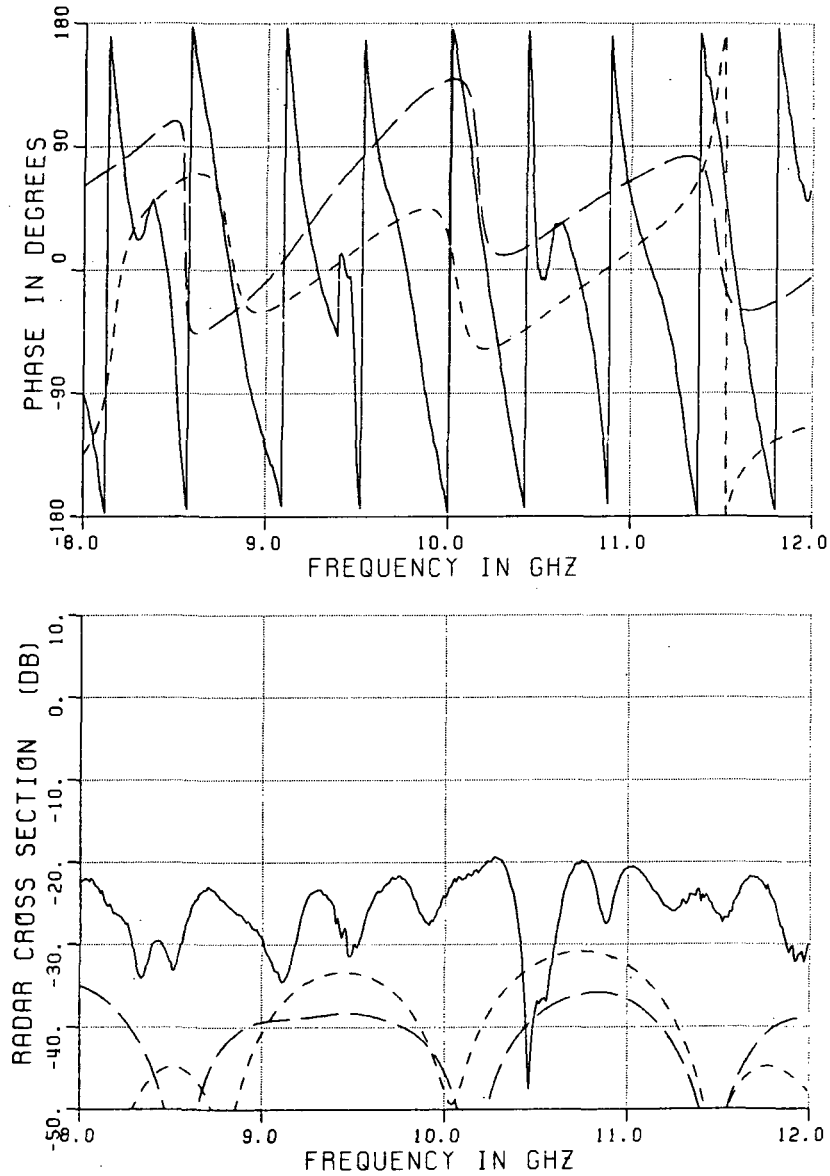


Figure 23a. Frequency scan in horizontal (x-z) plane. ϕ=0°, θ=30°, horizontal ($\hat{\theta}$) polarization. ——— measured, — — calculated, ---- measured (time gated) results.

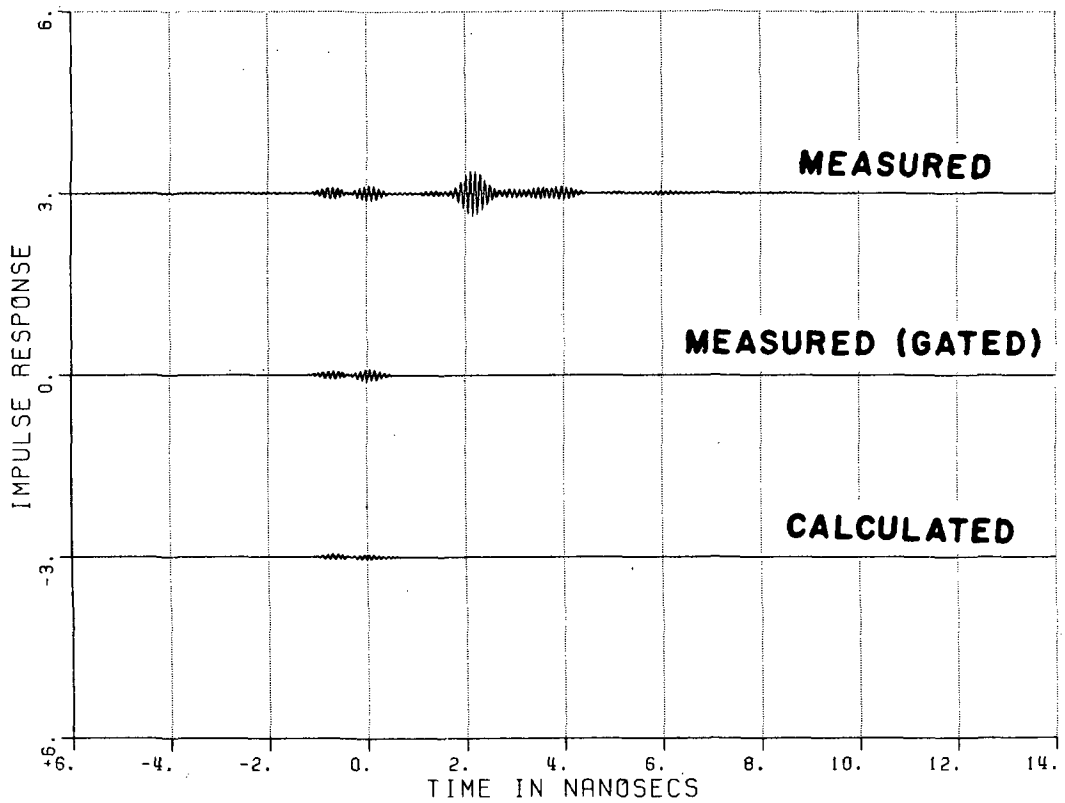


Figure 23b. Inverse Fourier transforms.

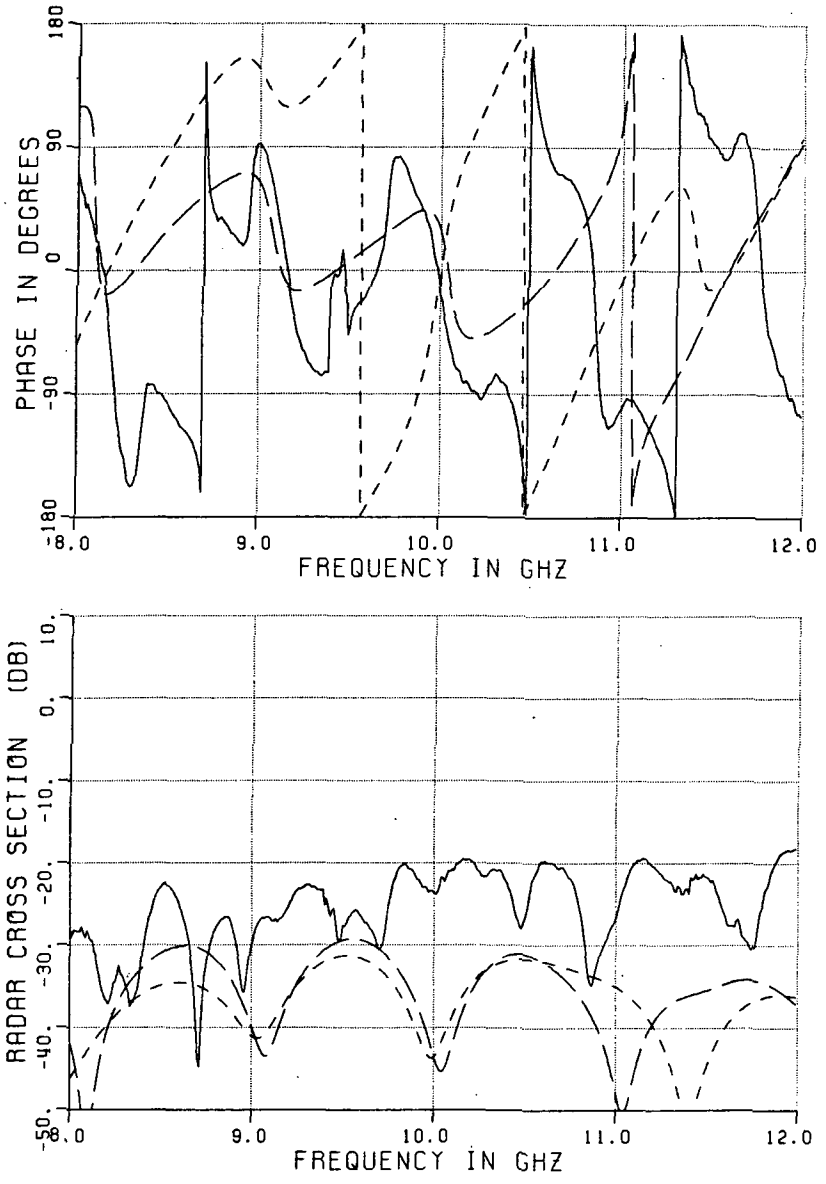


Figure 24a. Frequency scan in horizontal (x-z) plane. ϕ=0°, θ=45°, horizontal ($\hat{\theta}$) polarization.
____ measured, __ __ calculated,
---- *measured (time gated) results.*

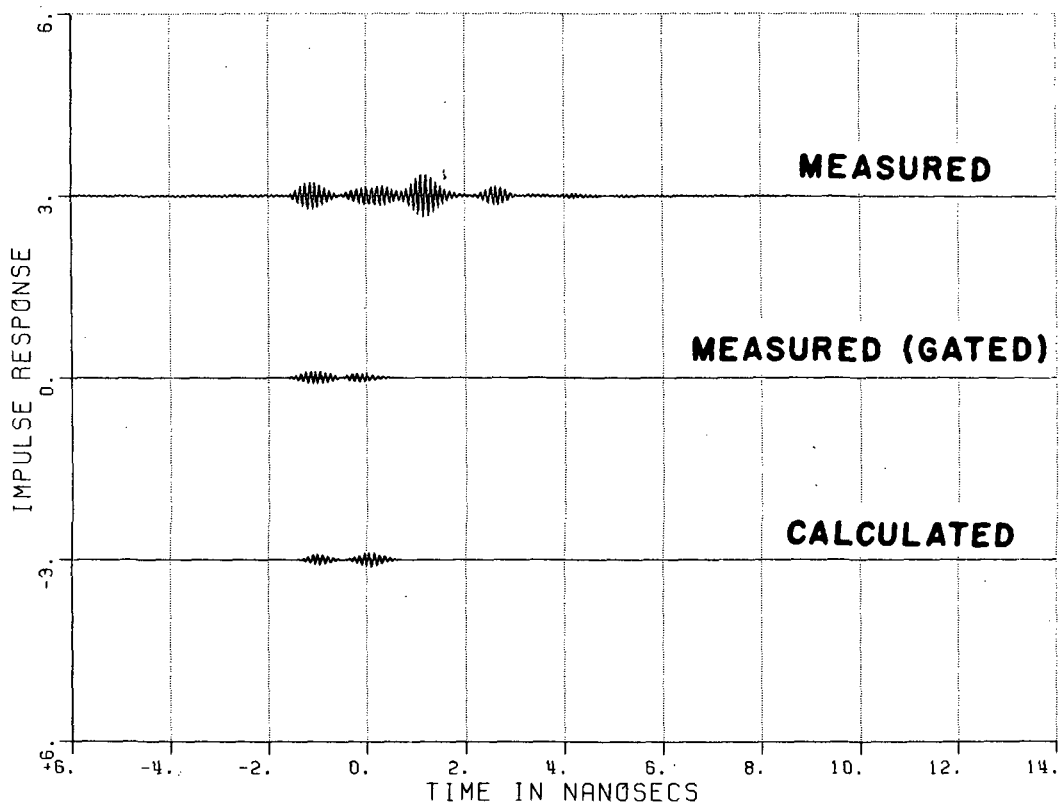


Figure 24b. Inverse Fourier transforms.

To compare the returns coming from the open end only, the unwanted return is gated out from the measured time domain data and is indicated as such in each figure. The actual measured and calculated returns are shown with constant shifts, as before. These time domain plots were then converted into the frequency domain and shown on the same graph. As can be seen in Figures 22a, 23a, and 24a the calculated (long-dashed line) and gated-out measured (short-dashed line) results agree fairly well since they both correspond to the returns pertaining to the rim of the inlet.

As explained before, the time domain responses shown are not the actual impulse responses because of the bandlimited nature of the data in frequency domain. If one had more frequency domain information then the time domain results would be closer to true impulse responses. To show this, calculations corresponding to Figure 20a are repeated and expressions of Equations (20), (26) and (27) are extended down to 10 MHz. The resulting frequency domain plot is shown in Figure 25a. Then, this data is inverse Fourier transormed, and the time domain result is shown in Figure 25b. This result is closer to an actual impulse response, and it clearly shows the single, double and triple diffractions from the vertical edges of the open end. Note that the double order diffractions originating from both edges return to the receiver at the same time.

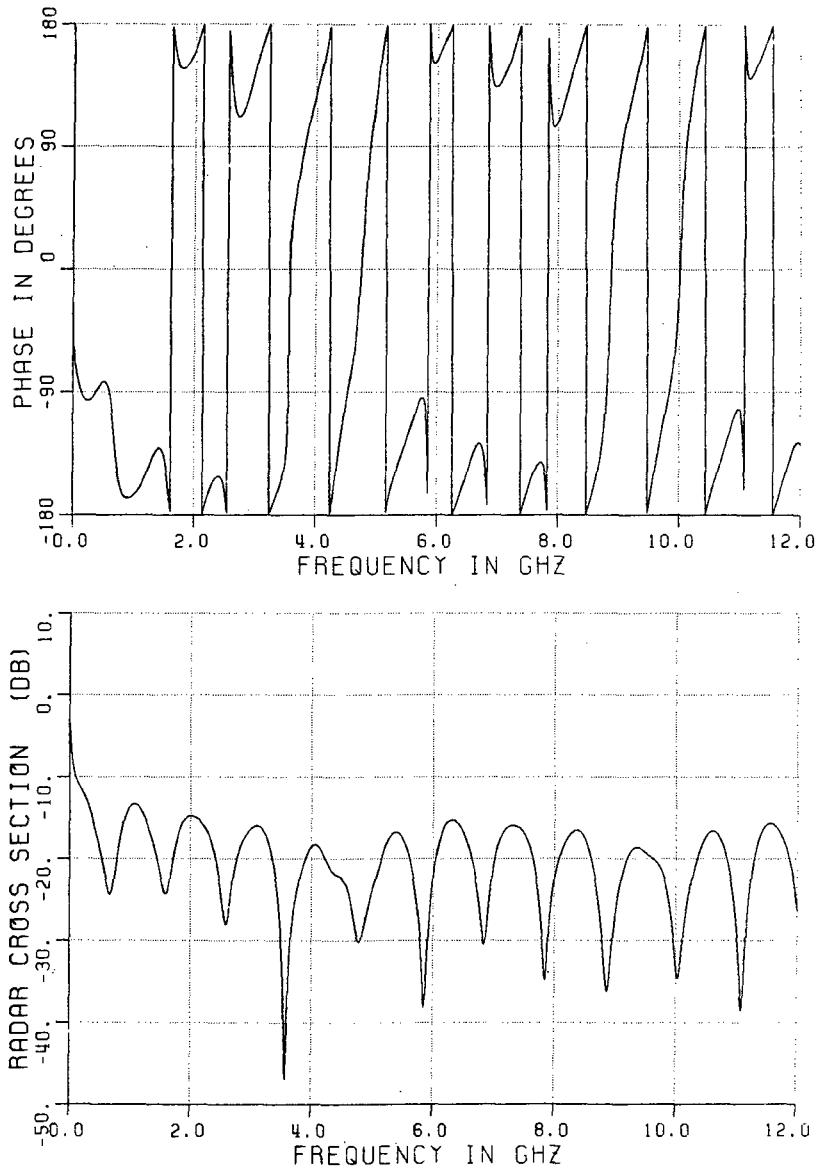


Figure 25a. Frequency scan in horizontal (x-z) plane. ϕ=0°, θ=45°, vertical ($\hat{\phi}$) polarization.

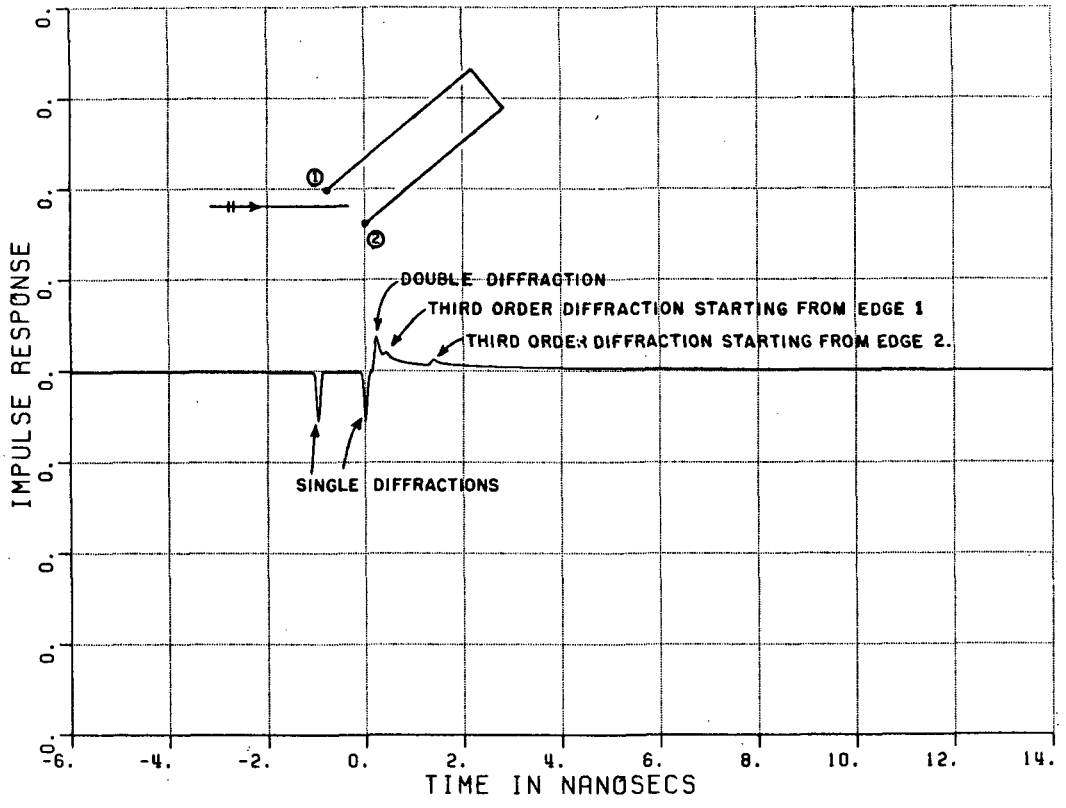


Figure 25b. Inverse Fourier transforms.

CHAPTER IV

THE ANALYSIS OF INTERIOR CAVITY EFFECTS

As described at the beginning of this report, the coupling of incident energy into the interior waveguide modes and their subsequent radiation after undergoing multiple relfections between the back wall termination and the open end comprise the cavity effects. The relationship between the analysis of the problem of modal coupling into and radiation from the open end is given in Appendix III. The classical approach to determine the radiated field from the open end due to a given mode involves an integration of the modal field across the aperture. The edge effects inherent in this procedure are not as good as predicted by the GTD. However, the edge effects given by the aperture integration method can be improved by the modified PTD approach as described in Appendix IV. The underlying argument in Appendix IV is that one can improve the aperture integration by adding the Ufimtsev's equivalent currents at the edges.

The modal field expressions in the rectangular waveguide as shown in Figure 1 is given in Appendix I (Equations A1-A13). Each mode is decomposed into four plane waves, each of which is a ray optical field. The transverse (to $\hat{z}$) components of the fields are as follows:

$$\bar{E}_{\text{modal}} = \frac{Nnm}{4j} \Big[(-\hat{x}U+\hat{y}V)\, e^{-jn_a x - jm_b y - j\beta_{nm} z} + (-\hat{x}U-\hat{y}V)\, e^{jn_a x - jm_b y - j\beta_{nm} z} + (\hat{x}U-\hat{y}V)\, e^{jn_a x + jm_b y - j\beta_{nm} z} + (\hat{x}U+\hat{y}V)\, e^{-jn_a x + jm_b y - j\beta_{nm} z} \Big] \tag{29}$$

and

$$\bar{H}_{\text{modal}} = \frac{Ynm\ Nnm}{4j} \Big[(-\hat{x}V-\hat{y}U)\, e^{-jn_a x - jm_b y - j\beta_{nm} z} + (\hat{x}V-\hat{y}U)\, e^{jn_a x - jm_b y - j\beta_{nm} z} + (\hat{x}V+\hat{y}U)\, e^{jn_a x + jm_b y - j\beta_{nm} z} + (-\hat{x}V+\hat{y}U)\, e^{-jn_a x + jm_b y - j\beta_{nm} z} \Big] . \tag{30}$$

The directions of propagation of these four rays are given by the exponents.

The integration of the modal fields across the aperture provides an approximate radiated field which is given by

$$\bar{E}^{r}_{a,nm} = \frac{jkZ_o}{4\pi} \int_0^a \int_0^b \Big[\hat{R}x\hat{R} \times \bar{J}^{\text{modal}}_{eq} + Y_o\, \hat{R} \times \bar{M}^{\text{modal}}_{eq} \Big] \frac{e^{-jkR}}{R}\, dy'dx' \tag{31}$$

where

$$\bar{J}_{eq}^{modal} = \hat{z} \times \bar{H}_{modal} = -N_{mn}\, Y_{nm} \left[\hat{x} U \cos n_a x \sin m_b y - \hat{y} V \sin n_a x \cos m_b y \right] \tag{32}$$

and

$$\bar{M}_{eq}^{modal} = \bar{E}_{modal} \times \hat{z} = -N_{mn} \left[\hat{x} V \sin n_a x \cos m_b y + \hat{y} U \cos n_a x \sin m_b y \right] \tag{33}$$

$$\hat{R}x\hat{R} \times \bar{J}_{eq}^{modal} + Y_o\, \hat{R}x\bar{M}_{eq}^{modal} = -N_{nm}\, U \cos n_a \times \sin m_b y$$

$$\left[Y_{nm} \left[-\hat{x}(1-\sin^2\theta\cos^2\phi) + \hat{y}\sin^2\theta\sin\phi\cos\phi + \hat{z}\sin\theta\cos\theta\cos\phi \right] + Y_o \left[-\hat{x}\cos\theta + \hat{z}\sin\theta\cos\phi \right] \right]$$

$$-N_{nm} V \sin n_a \times \cos m_b y \left[Y_o \left[\hat{y}\cos\theta - \hat{z}\sin\theta\sin\phi \right] + Y_{nm} \left[-\hat{x}\sin^2\theta\sin\phi\cos\phi + \hat{y}(1-\sin^2\theta\sin^2\phi) - \hat{z}\sin\theta\cos\theta\sin\phi \right] \right] . \tag{34}$$

In the far field

$$\bar{R} \cong \bar{r} - \bar{r}' \cdot \hat{r} \tag{35}$$

and

$$\hat{R}x\hat{R}x\bar{J}_{eq}^{modal} + Y_o \hat{R}x\bar{M}_{eq}^{modal} = -N_{nm} U \cos n_a x \sin m_b y \left[Y_{nm}[-\hat{\theta}\cos\theta\cos\phi + \hat{\phi}\sin\phi] + Y_o[-\hat{\theta}\cos\phi + \phi\cos\theta\sin\phi] \right]$$

$$-N_{nm} V \sin n_a x \cos m_b y \left\{ Y_{nm}[\hat{\theta}\cos\theta\sin\phi + \hat{\phi}\cos\phi + Y_o[\theta\sin\phi + \hat{\phi}\cos\theta\cos\phi] \right\} \tag{36}$$

Substituting into Equation (31), one obtains that

$$\bar{E}^{r}_{a,nm} = -\frac{kN_{nm}}{4\pi r}\, e^{-jkr}\, e^{j\frac{ksin\theta}{2}(acos\phi+bsin\phi)}$$

$$U\left[-\hat{\theta}cos\phi\left(1+\frac{Y_{nm}}{Y_o}cos\theta\right)+\hat{\phi}sin\phi\left(cos\theta+\frac{Y_{nm}}{Y_o}\right)\right]$$

$$\left[j^n \frac{sin\frac{a}{2}(ksin\theta cos\phi+n_a)}{ksin\theta cos\phi+n_a} + (-j)^n \frac{sin\frac{a}{2}(ksin\theta cos\phi-n_a)}{ksin\theta cos\phi-n_a}\right]$$

$$\left[j^m \frac{sin\frac{b}{2}(ksin\theta cos\phi+m_b)}{ksin\theta cos\phi+m_b} - (-j)^m \frac{sin\frac{b}{2}(ksin\theta cos\phi-m_b)}{ksin\theta cos\phi-m_b}\right]$$

$$+V\left[-\hat{\theta}sin\phi\left(1+\frac{Y_{nm}}{Y_o}cos\theta\right)+\hat{\phi}cos\phi\left(cos\theta+\frac{Y_{nm}}{Y_o}\right)\right]$$

$$\left[j^n \frac{sin\frac{a}{2}(ksin\theta cos\phi+n_a)}{ksin\theta cos\phi+n_a} - (-j)^n \frac{sin\frac{a}{2}(ksin\theta cos\phi-n_a)}{ksin\theta cos\phi-n_a}\right]$$

$$\left[j^m \frac{sin\frac{b}{2}(ksin\theta cos\phi+m_b)}{ksin\theta cos\phi+m_b} + (-j)^m \frac{sin\frac{b}{2}(ksin\theta cos\phi-m_b)}{ksin\theta cos\phi-m_b}\right] \qquad (37)$$

As it is seen from Equation (37), the pattern has a $\frac{sinx}{x}$ type behaviour in both $\hat{\theta}$ and $\hat{\phi}$ directions. There are four difference $\frac{sinx}{x}$ forms, each of which is due to the integration of a plane wave component of the mode as described in Equation (29). Therefore each $\frac{sinx}{x}$ peaks up at the

corresponding plane wave directions. Also, as the waveguide dimensions get larger, the peaks become sharper. As a result, only a few modes contribute strongly to the radiation around a given observation direction.

As mentioned earlier, the edge effects given by aperture integration are improved using a modified PTD approach as discussed in Appendix IV. The equivalent electric and magnetic Ufimtsev edge currents are [6] given by

$$\bar{I}_u = - \frac{\hat{e} \cdot \bar{E}^i(\text{edge})}{Z_o \sin\beta_i \sin\beta_d} \; D_s^u(\psi,\psi') \sqrt{\frac{8\pi}{jk}} \; \hat{e} \quad , \tag{38}$$

and

$$\bar{M}_u = - \frac{\hat{e} \cdot \bar{H}^i(\text{edge})}{Y_o \sin\beta_i \sin\beta_d} \; D_h^u(\psi,\psi') \sqrt{\frac{8\pi}{jk}} \; \hat{e} \quad , \tag{39}$$

where the Ufimtsev diffraction coefficients are

$$D_{s\,h}^u = - \frac{e^{-j\pi/4}}{2\sqrt{2\pi k}} \left[\left[\sec\left(\frac{\psi-\psi'}{2}\right) - \tan\left(\frac{\psi-\psi'}{2}\right) \right] \mp \left[\sec\left(\frac{\psi+\psi'}{2}\right) - \tan\left(\frac{\psi+\psi'}{2}\right) \right] \right] . \tag{40}$$

after simplification, it can be written as follows:

$$D_{s\,h}^u = - \frac{2e^{-j\pi/4}}{\sqrt{2\pi k}} \; \frac{\sin\frac{\psi}{2} - \sin\frac{\psi'}{2}}{\cos\psi + \cos\psi'} \left[\begin{matrix} \sin\frac{\psi'}{2} \\ \cos\frac{\psi}{2} \end{matrix} \right] \tag{41}$$

Therefore, one obtains

$$\bar{I}_u = -Y_o \sqrt{\frac{8\pi}{jk}} \frac{D_s^u(\psi,\psi')}{\sin\beta_i \sin\beta_d} \frac{N_{nm}}{2j}$$

$$\begin{cases} \pm \hat{x}\, U\cos n_a x'\, e^{\mp jm_b y'} = \hat{x} \left[(-1)^{m+1}\right] U\cos n_a x' & \text{for edge 1} \\ & \text{for edge 2} \\ \pm \hat{y}\, V\cos m_b y'\, e^{\mp jn_a x'} = \hat{y} \left[(-1)^{n+1}\right] (-v)\cos m_b y' & \text{for edge 3} \\ & \text{for edge 4} \end{cases} \tag{42}$$

and

$$\bar{M}_u = -Z_o \sqrt{\frac{8\pi}{jk}} \frac{D_h^u(\psi,\psi')}{\sin\beta_i \sin\beta_d} \frac{N_{nm} Y_{nm}}{2j}$$

$$\begin{cases} \hat{x} \left[(-1)^m\right] V j \sin n_a x' & \text{for edge 1} \\ & \text{for edge 2} \\ \hat{y} \left[(-1)^n\right] U j \sin m_b y' & \text{for edge 3} \\ & \text{for edge 4} \end{cases} \tag{43}$$

The radiated field for these edge correction terms is then given by

$$\bar{E}^r_{u,nm} = \frac{jkZ_o}{4\pi} \int_{rim} \left[\hat{R} \times \hat{R} \times \bar{I}_u + Y_o \hat{R} \times \bar{M}_u\right] \frac{e^{-jkR}}{R} d\ell' \quad . \tag{44}$$

In the far field, the above integrations for the radiated field can be done analytically in closed form and the result is;

$$\bar{E}^{r}_{u,nm} = -\sqrt{\frac{k}{8\pi j}}\ \frac{N_{nm}}{\sin\beta_i \sin\beta_d}\ \frac{e^{-jkr}}{r}\ e^{j\frac{k}{2}\sin\theta(a\cos\phi+b\sin\phi)}$$

$$\left\{ D^{u}_{s} \left[(-\hat{\theta}\cos\theta\cos\phi+\hat{\phi}\sin\phi)U \left[e^{-j\frac{kb}{2}\sin\theta\sin\phi} + (-1)^{m+1} e^{j\frac{kb}{2}\sin\theta\sin\phi} \right] \right] \right.$$

$$\left[(-j)^{n} \frac{\sin\frac{a}{2}(k\sin\theta\cos\phi-n_a)}{k\sin\theta\cos\phi-n_a} + (j)^{n} \frac{\sin\frac{a}{2}(k\sin\theta\cos\phi+n_a)}{k\sin\theta\cos\phi+n_a} \right]$$

$$+D^{u}_{s} \left[(\hat{\theta}\cos\theta\sin\phi+\hat{\phi}\cos\phi)V \left[e^{-j\frac{ka}{2}\sin\theta\cos\phi} + (-1)^{n+1} e^{j\frac{ka}{2}\sin\theta\cos\phi} \right] \right]$$

$$\left[(-j)^{m} \frac{\sin\frac{b}{2}(k\sin\theta\sin\phi-m_b)}{k\sin\theta\sin\phi-m_b} + (j)^{m} \frac{\sin\frac{b}{2}(k\sin\theta\sin\phi+m_b)}{k\sin\theta\sin\phi+m_b} \right]$$

$$+\frac{Y_{nm}}{Y_o} D^{u}_{h} \left[(\hat{\theta}\sin\phi+\hat{\phi}\cos\hat{\theta}\cos\phi)V \left[e^{-j\frac{kb}{2}\sin\theta\sin\phi} + (-1)^{m} e^{j\frac{kb}{2}\sin\theta\sin\phi} \right] \right]$$

$$\left[-(-j)^{n} \frac{\sin\frac{a}{2}(k\sin\theta\cos\phi-n_a)}{k\sin\theta\cos\phi-n_a} + (j)^{n} \frac{\sin\frac{a}{2}(k\sin\theta\cos\phi+n_a)}{k\sin\theta\cos\phi+n_a} \right]$$

$$+\frac{Y_{nm}}{Y_o} D^{u}_{h} \left[(\hat{\theta}\cos\phi+\hat{\phi}\cos\hat{\theta}\sin\phi)U \left[e^{-j\frac{ka}{2}\sin\theta\cos\phi} + (-1)^{n} e^{j\frac{ka}{2}\sin\theta\cos\phi} \right] \right]$$

$$\left. \left[-(-j)^{m} \frac{\sin\frac{b}{2}(k\sin\theta\sin\phi-m_b)}{k\sin\theta\sin\phi-m_b} + (j)^{n} \frac{\sin\frac{a}{2}(k\sin\theta\sin\phi+m_b)}{k\sin\theta\sin\phi+m_b} \right] \right\}$$

(45)

The total radiated field is the summation of Equations (37) and (45); namely,

$$\bar{E}^r_{nm} = \bar{E}^r_{a,nm} + \bar{E}^r_{u,nm} \quad . \tag{46}$$

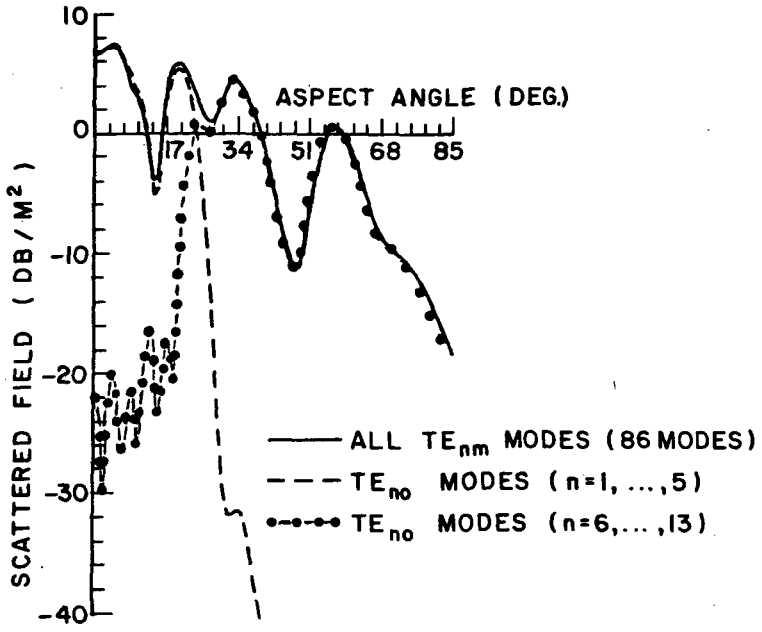
The total radiated field is the superposition of the radiation of all propagating modes.

Numerical Results for Chapter IV

The experimental measurements and calculations are done in two categories as in Chapter III; namely, aspect angle and frequeny scans and they are given in dB over m^2. Since it is difficult to experimentally isolate the open end rim scattering from the cavity effects, the calculations include both effects for comparison purposes.

The waveguide model is large in terms of the wavelength; therefore, a large number of propagating modes can exist inside the cavity. For example, at the frequency of 10 GHz, there are 172 propagating modes as well as an infinite number of evanescent modes. Since the waveguide axial length is very long with respect to the wavelength, the evanescent modes will decay very significantly such that they can be neglected. Then the next question is whether the propagating modes have a preferred direction of radiation in that one can choose a few special ones rather than all the propagating modes and include only those in the analysis. It is obvious from Equation (47) that modal radiation occur at discrete plane wave directions for each mode. Since each mode has a discrete radiation direction, some will radiate close to desired direction, and

others will not. This being the case, one can anticipate that only a few modes are significantly excited by the incident plane wave and radiate significantly in the backscatter direction. This claim has been checked numerically, and the results are shown in Figure 26. An open-ended rectangular waveguide with dimensions equal to the experimental model used in this study is analyzed at 10 GHz. The backscatter field is calculated in (x-z) plane by varying the aspect angle θ. Note that only the modal effects are included and the incident field is assumed to be $\hat{\phi}$-polarized. It is found that only the TE_{no} modes are excited in this plane for this polarization. Their plane wave directions or modal ray angles are tabulated in the figure. The scattered field is calculated by including all modal contributions as indicated by the solid line. For comparison purposes the contributions of TE_{no} (n=1,...5) modes and TE_{no} (n=6...13) modes are shown in the same figure. Note that the first five modes radiate strongly and almost replicate the solid curve in the region close to their modal ray angle directions. The remaining seven modes are major contributors for the large aspect angles. After observing this fact, the research focused on finding a rule of thumb procedure which could be used to select the minimum number of modes needed for a given direction of incident plane wave. From numerical results and comparisons with the experimental data, it was found that in horizontal and vertical planes only three modes were sufficient for the inlet under test. These three modes are selected based on their modal radiation direction such that they are closest to the incident plane wave direction. The aspect angle scan



MODAL RAY ANGLES OF TE$_{no}$ MODES

TE$_{10}$	4.23°
TE$_{20}$	9°
TE$_{30}$	12.8°
TE$_{40}$	17.17°
TE$_{50}$	21.65°

TE$_{60}$	26.28°
TE$_{70}$	31.11°
TE$_{80}$	36.19°
TE$_{90}$	41.63°
TE$_{10,0}$	47.57°
TE$_{11,0}$	54.29°
TE$_{12,0}$	62.34°
TE$_{13,0}$	73.66°

Figure 26. Importance of modes whose modal ray angles are near the angle of incidence.

results are shown in Figures 27 through 38. As done in Chapter III, the experimental measurement results are indicated by the solid line and calculations by the dashed one. In each case a comparison is provided for the calculations which include all modes versus three modes. In all cases a 1 dB/bounce energy loss is assumed to model the imperfection of the conductivity of the model used in the measurements.

Since this new concept proved to be so valuable in the principal plane, it is next applied to ϕ=45° plane to see if it fails when the incident plane wave direction is not aligned with the structural symmetry. The aspect angle scan is calculated in the ϕ=45° plane for both the $\hat{\phi}$ and $\hat{\theta}$ polarized incident fields. The results are shown in Figures 39 and 40. In this case, the 18 preselected modes are compared with the complete 172 modes as shown in each figure. Note that more terms are necessary in this general case as indicated by the results shown in Figure 41 where the six mode result is compared with the 18 mode one. Even so it is clear that one can use far fewer than the complete set of modes.

Finally, the frequency scan results are calculated and compared with measurements in Figures 42 through 49. As in Chapter III, the time domain results are deliberately shifted to better illustrate the comparisons. Note that in each case the comparisons are exceptional.

In Figure 50, the contribution of each mode is plotted separately for the geometry associated with the results of Figure 45. It is seen that as the mode number increases the given mode undergoes more bounces inside the waveguide, travels a longer distance and therefore its return

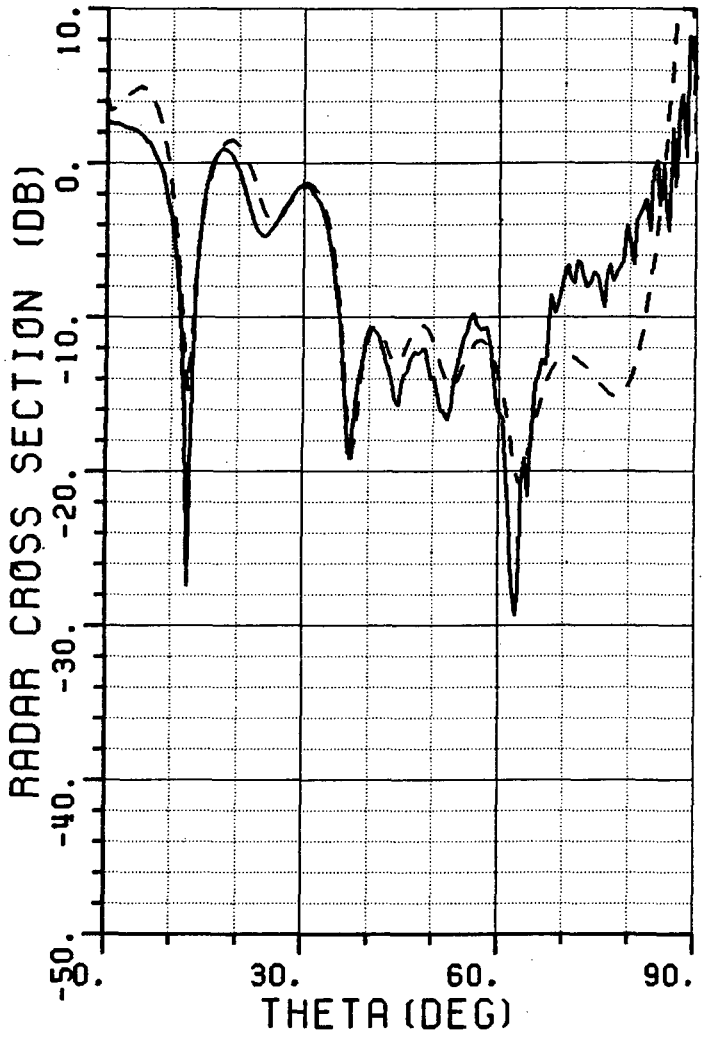


Figure 27a. Aspect angle scan in horizontal (x-z) plane. Vertical (ϕ) polarization, frequency 8.0 GHz. ___ measured, --- calculated results.

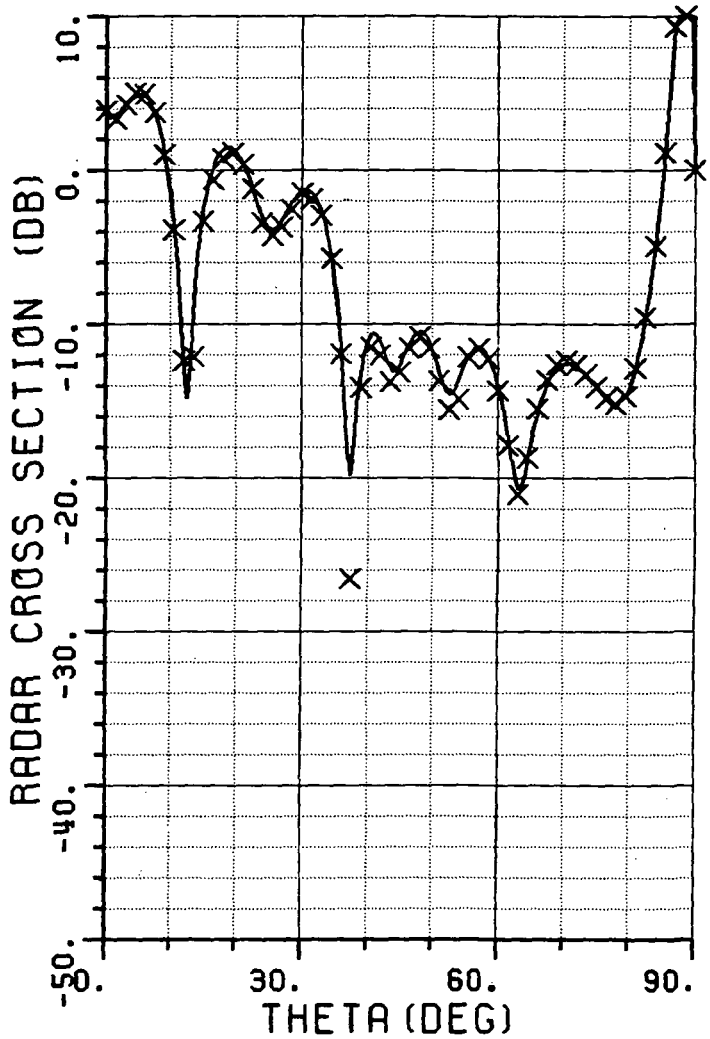


Figure 27b. Calculated aspect angle scans corresponding to Figure 27a.
___ All modes are included
xxx Only 3 modes are included

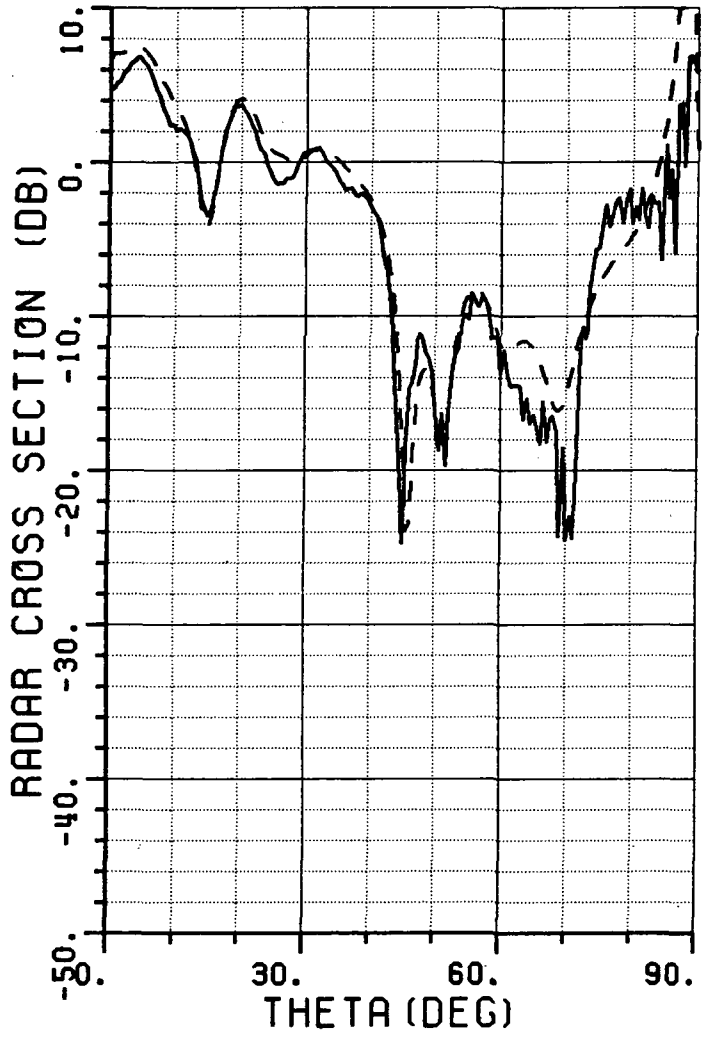


Figure 28a. Aspect angle scan in horizontal (x-z) plane. Vertical ($\hat{\phi}$) polarization, frequency 10.0 GHz. ___ measured, --- calculated results.

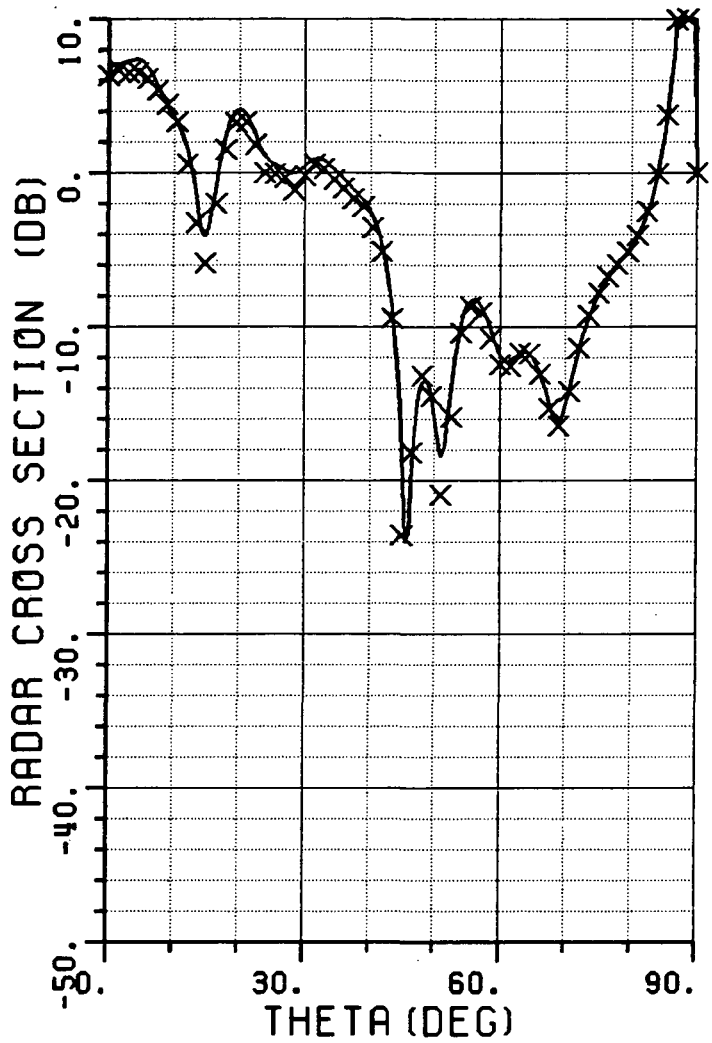


Figure 28b. Calculated aspect angle scans corresponding to Figure 28a.
___ All modes are included
xxx Only 3 modes are included

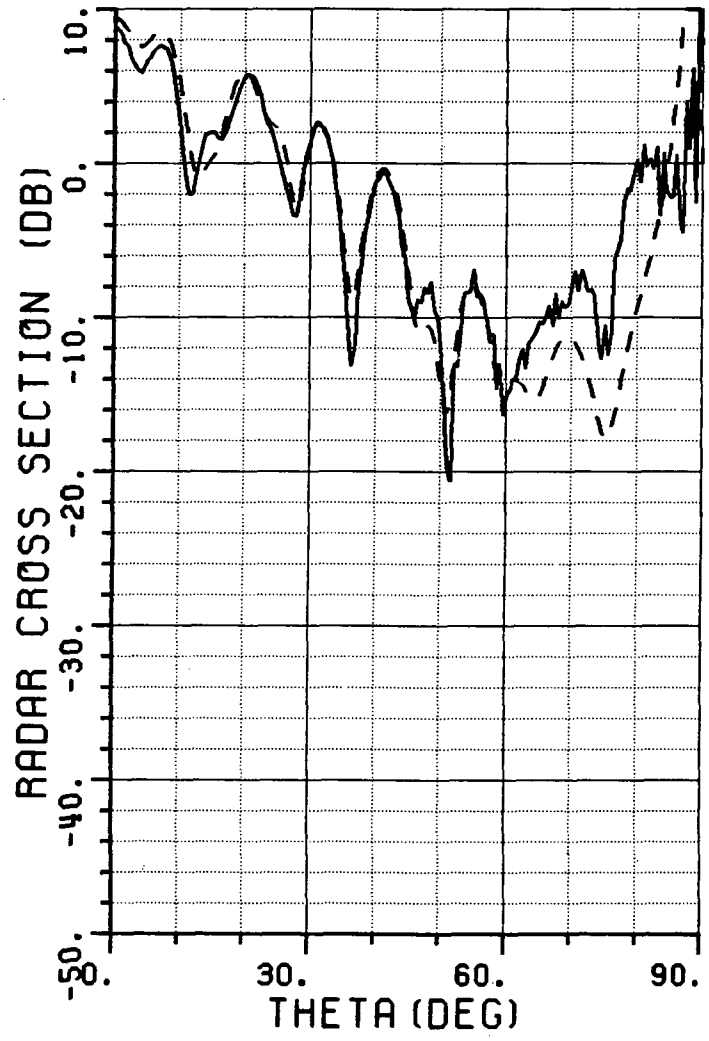


Figure 29a. Aspect angle scan in horizontal (x-z) plane. Vertical (ϕ) polarization, frequency 12.0 GHz. ___ measured, --- calculated results.

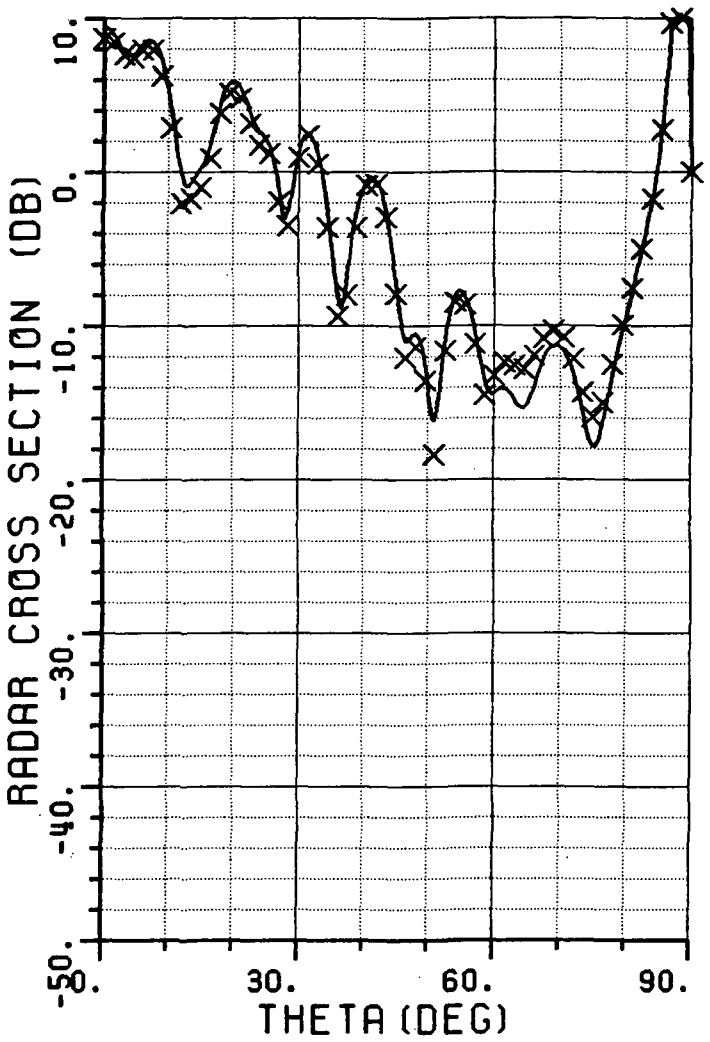


Figure 29b. Calculated aspect angle scans corresponding to Figure 29a.
—— All modes are included
xxx Only 3 modes are included

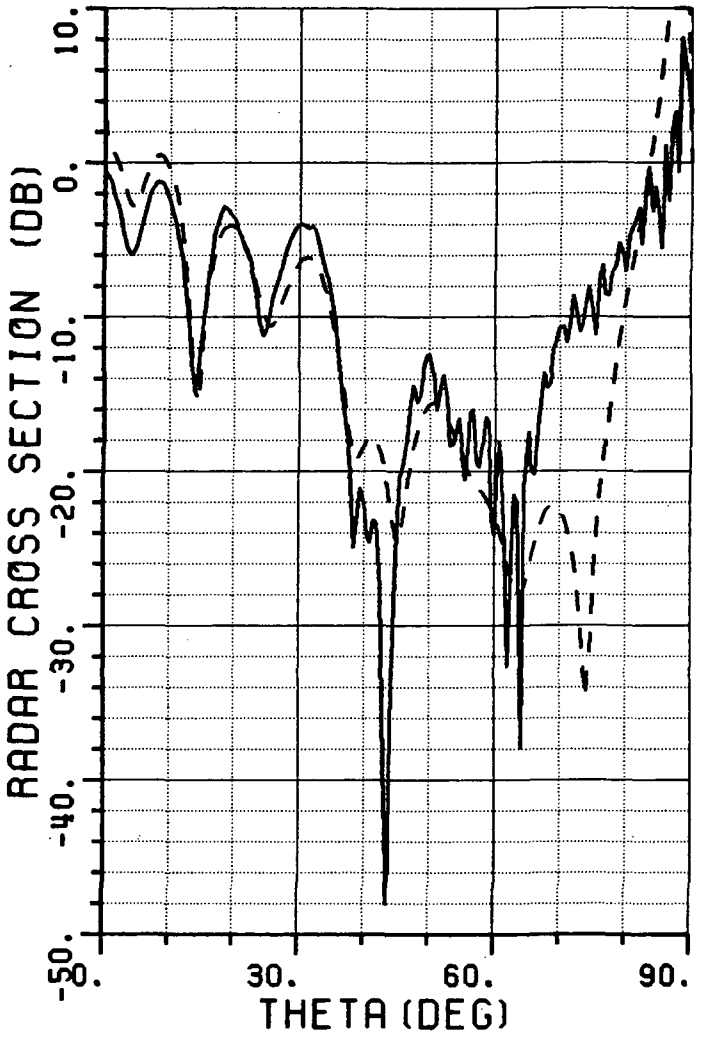


Figure 30a. Aspect angle scan in horizontal (x-z) plane. Horizontal ($\hat{\theta}$) polarization, frequency 8.02 GHz. ___ measured, --- calculated results.

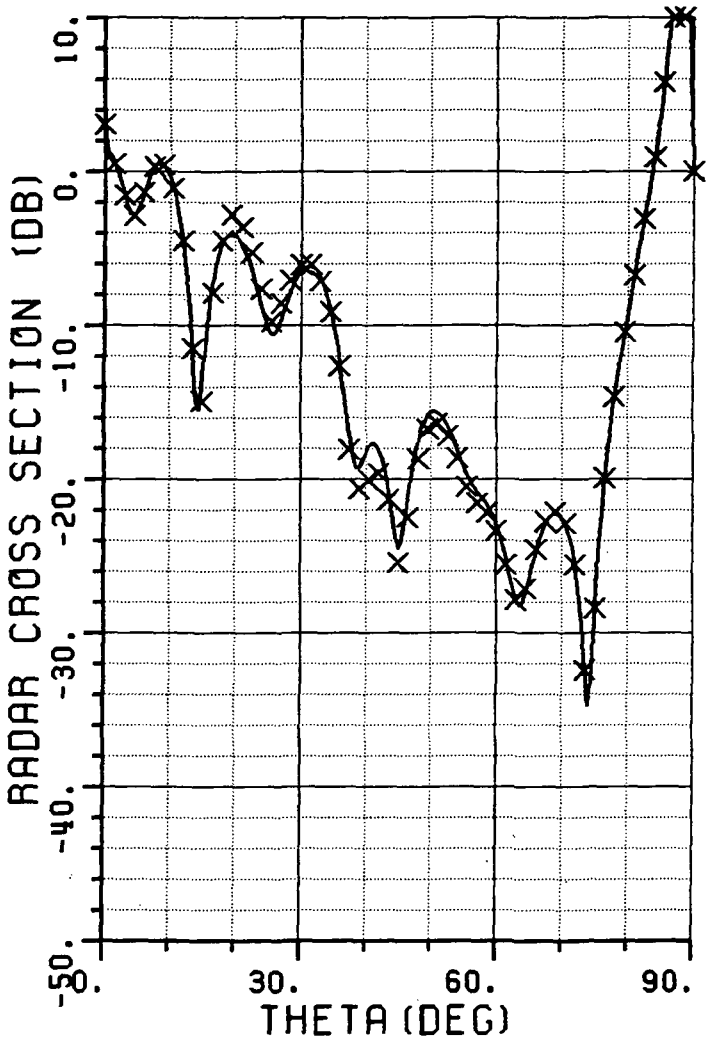


Figure 30b. Calculated aspect angle scans corresponding to Figure 30a.
___ All modes are included
xxx Only 3 modes are included

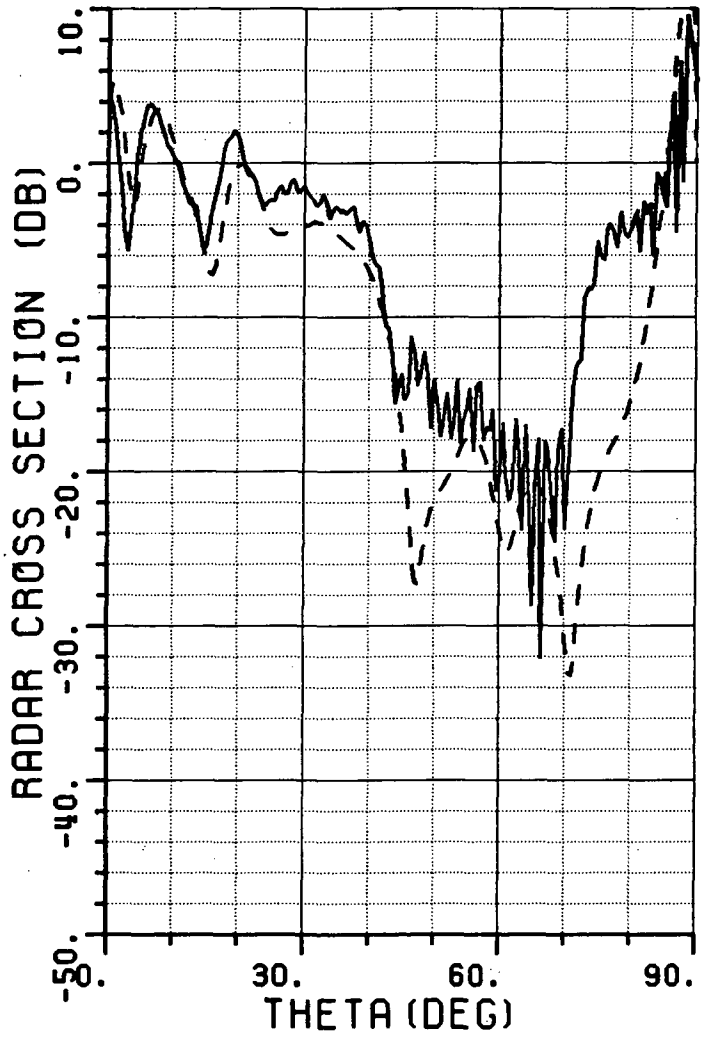


Figure 31a. Aspect angle scan in horizontal (x-z) plane. Horizontal ($\hat{\theta}$) polarization, frequency 9.98 GHz. ___ measured, --- calculated results.

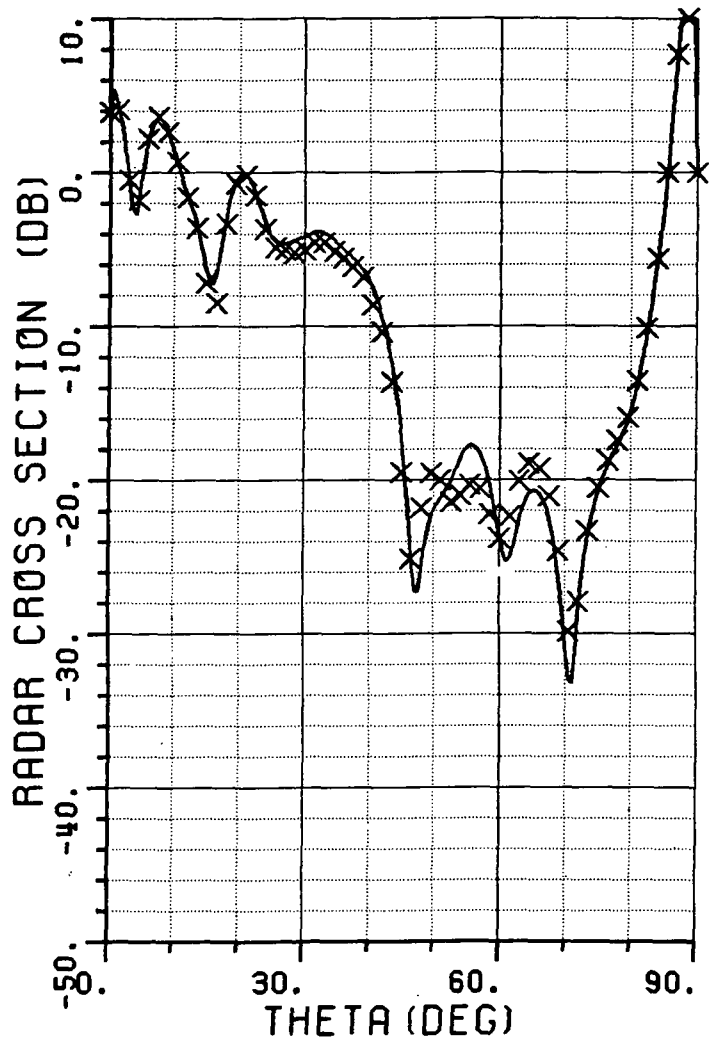


Figure 31b. Calculated aspect angle scans corresponding to Figure 31a.
—— All modes are included
xxx Only 3 modes are included

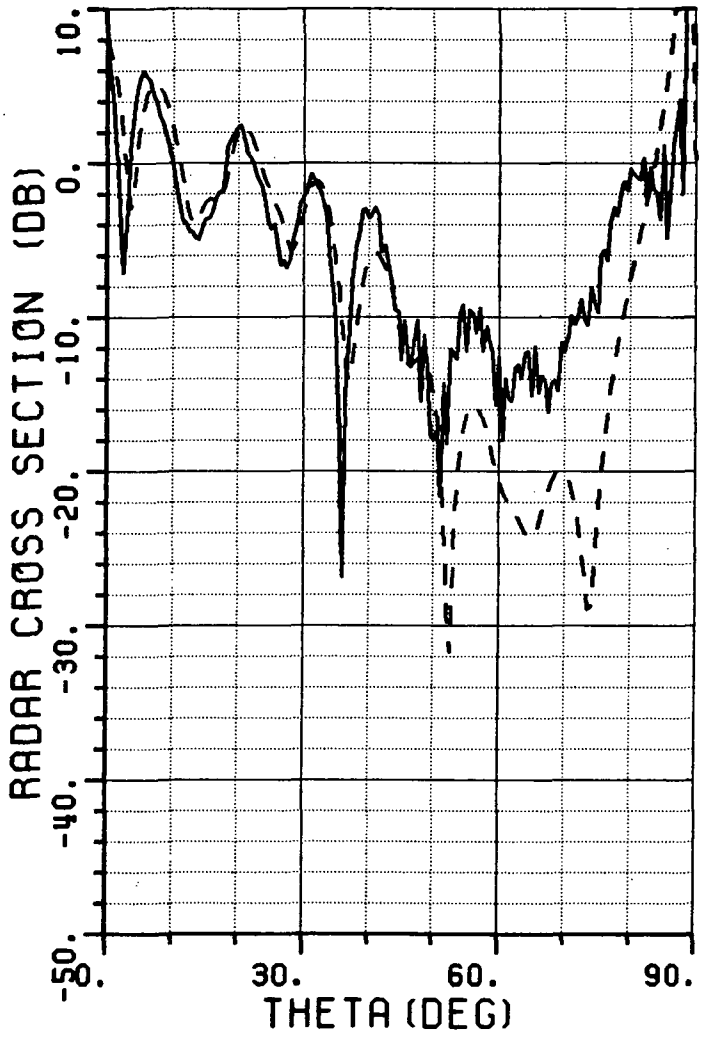


Figure 32a. Aspect angle scan in horizontal (x-z) plane. Horizontal ($\hat{\theta}$) polarization, frequency 11.95 GHz. ___ measured, --- calculated results.

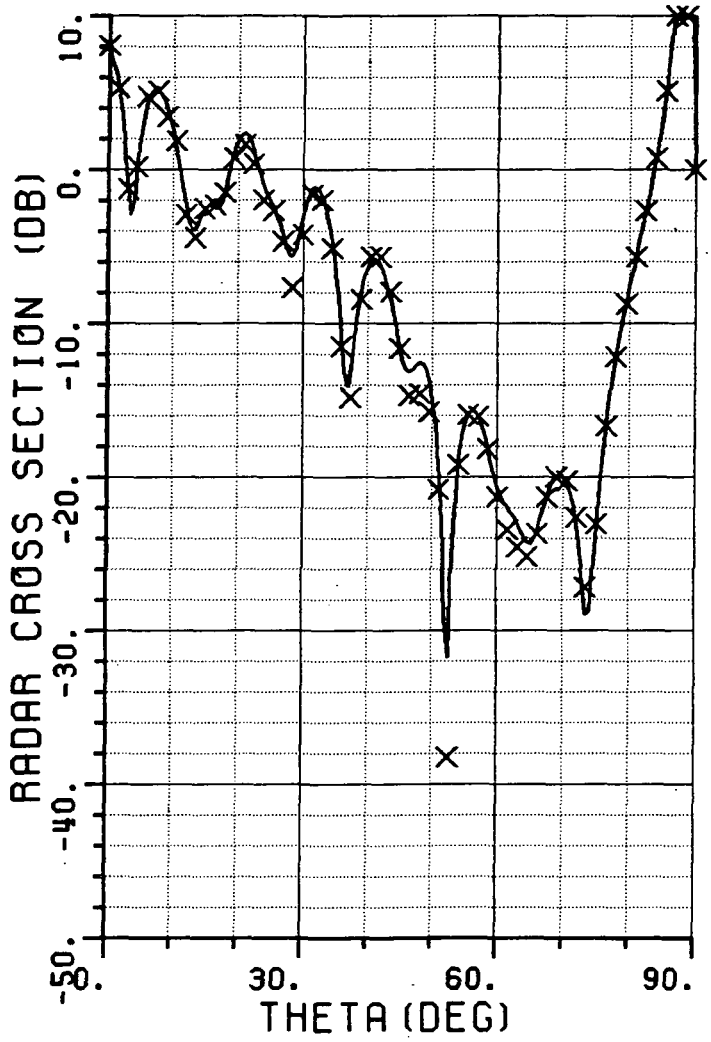


Figure 32b. Calculated aspect angle scans corresponding to Figure 32a.
—— All modes are included
xxx Only 3 modes are included

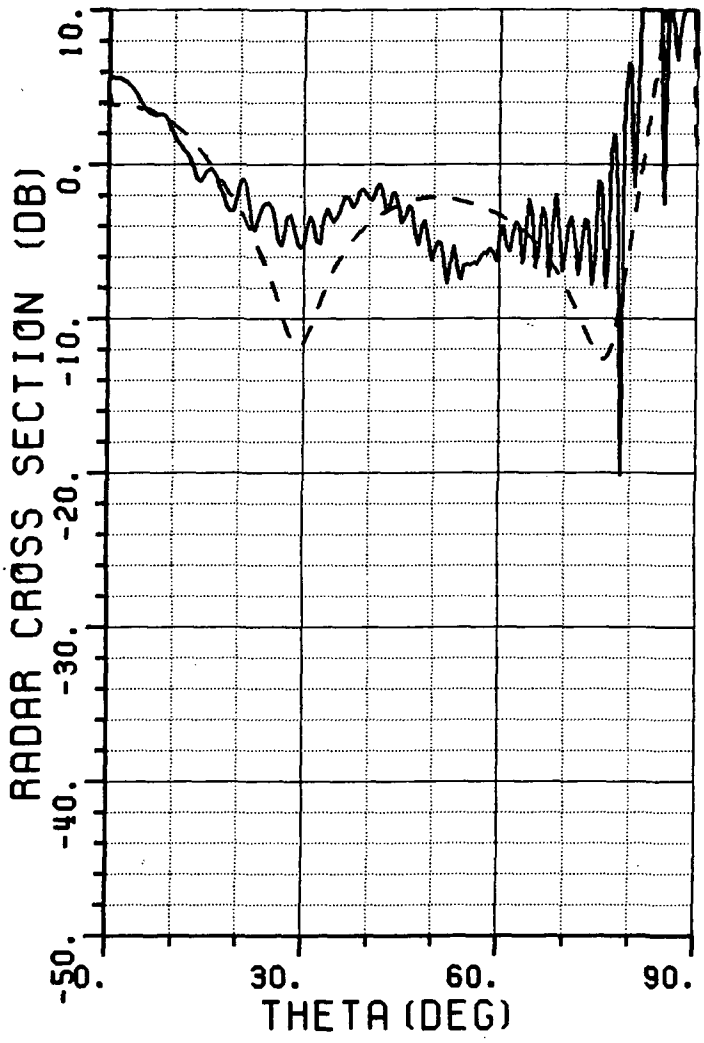


Figure 33a. Aspect angle scan in vertical (y-z) plane. Vertical ($\hat{\theta}$) polarization, frequency 8.02 GHz. ___ measured, --- calculated results.

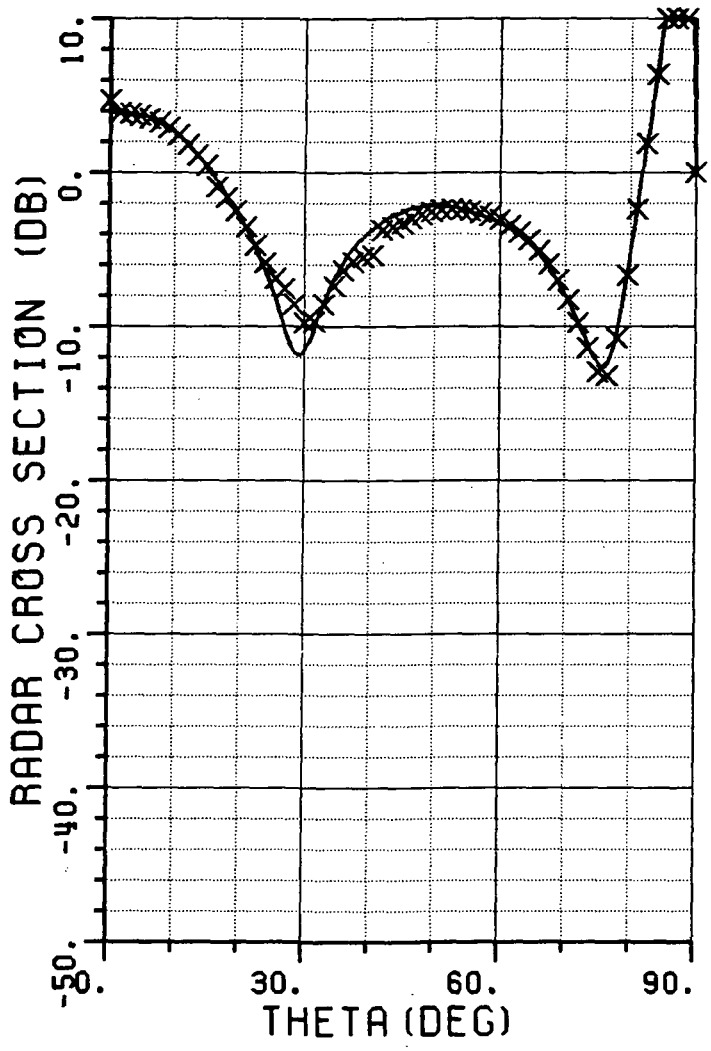


Figure 33b. Calculated aspect angle scans corresponding to Figure 33a.
—— All modes are included
xxx Only 3 modes are included

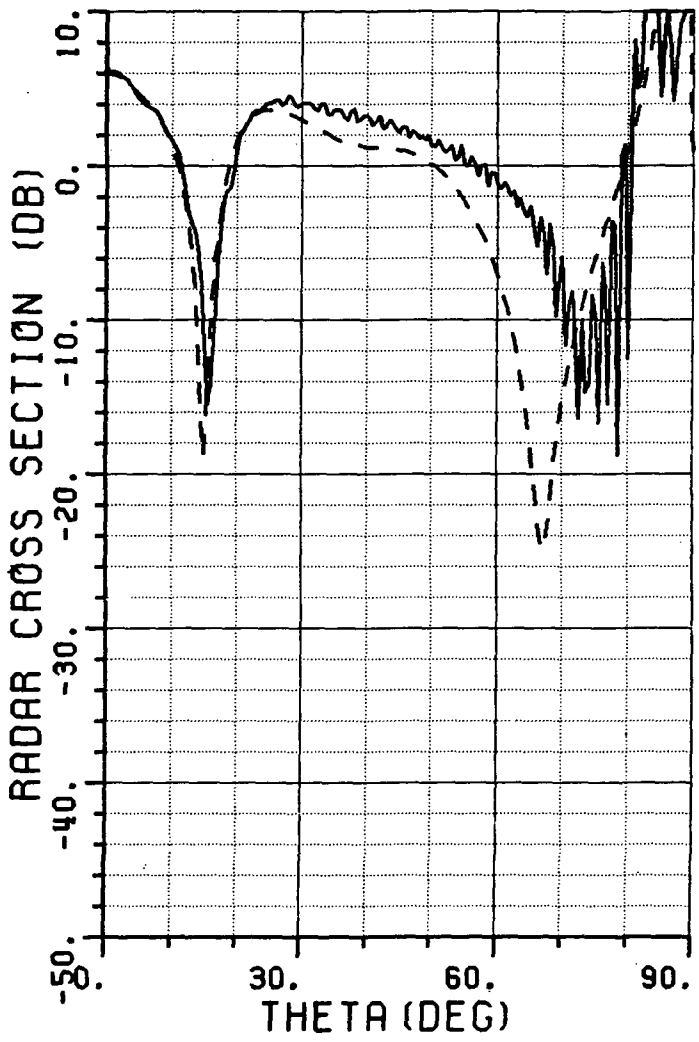


Figure 34a. Aspect angle scan in vertical (y-z) plane. Vertical ($\hat{\theta}$) polarization, frequency 10.01 GHz. —— measured, --- calculated results.

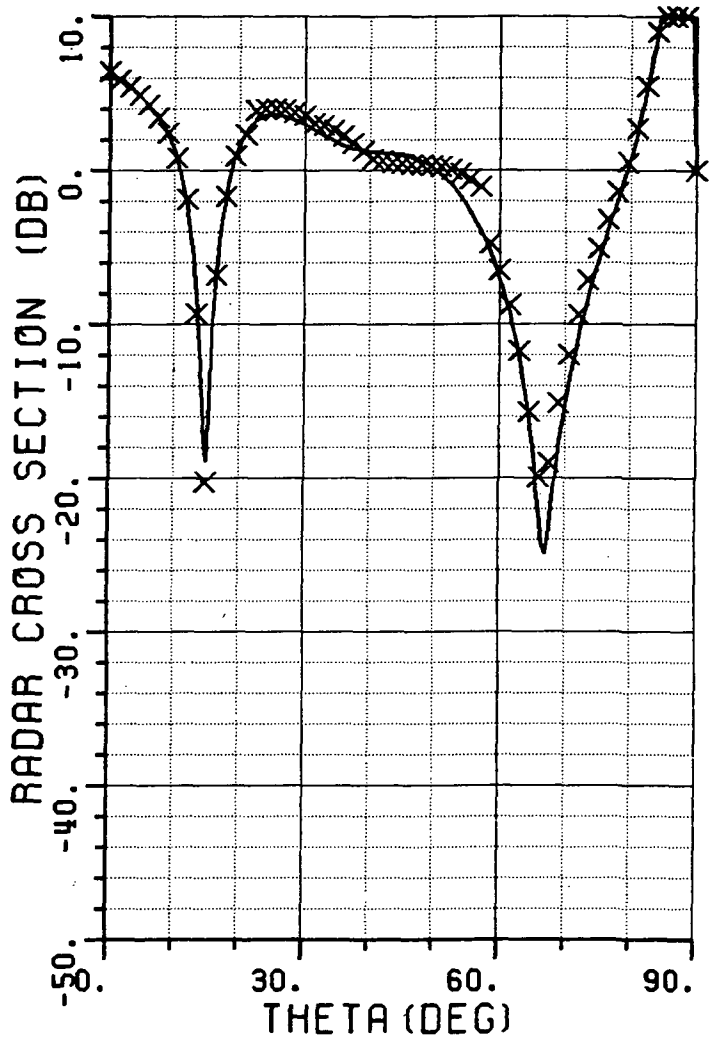


Figure 34b. Calculated aspect angle scans corresponding to Figure 34a.
—— All modes are included
xxx Only 3 modes are included

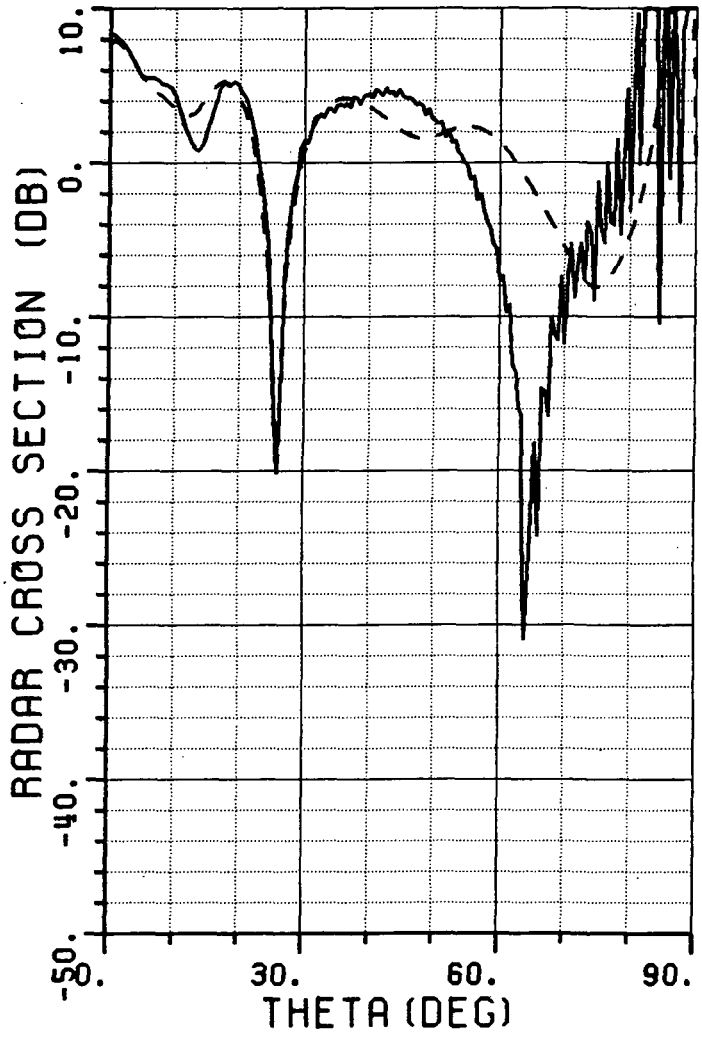


Figure 35a. Aspect angle scan in vertical (y-z) plane.
Vertical ($\hat{\theta}$) polarization, frequency 11.96 GHz.
___ measured, --- calculated results.

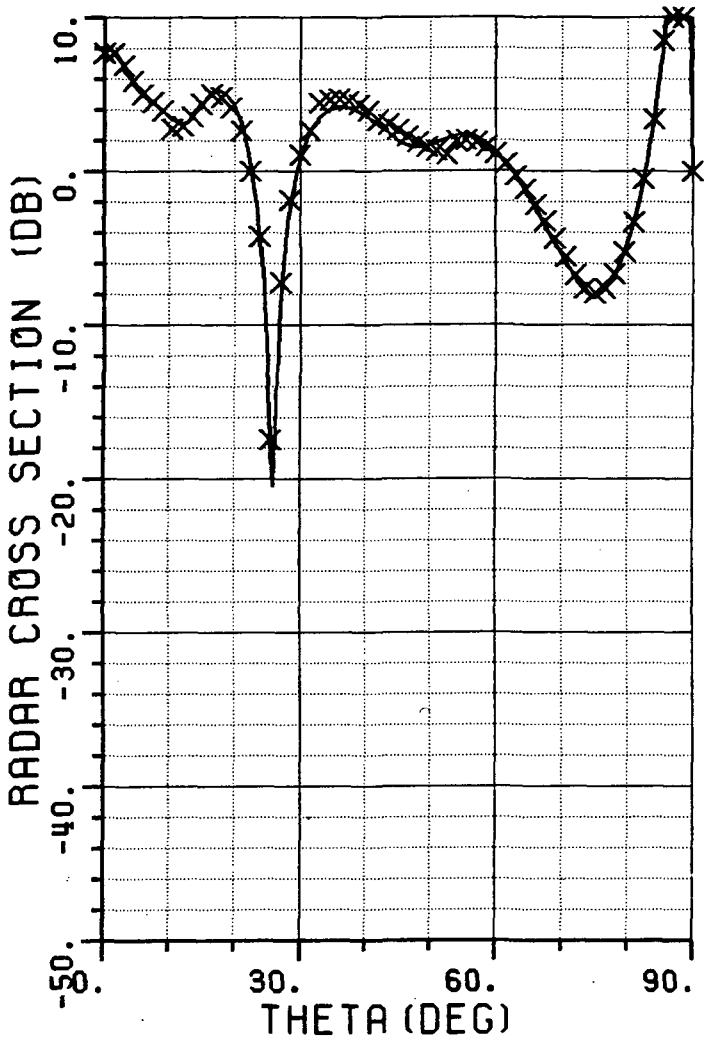


Figure 35b. Calculated aspect angle scans corresponding to Figure 35a.
___ All modes are included
xxx Only 3 modes are included

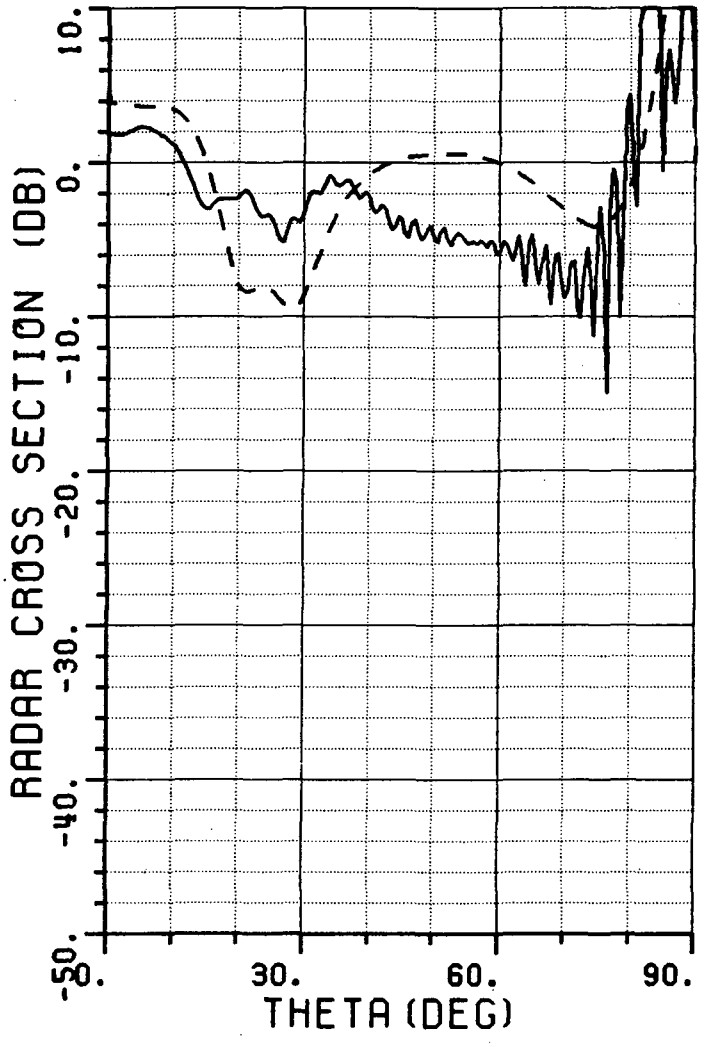


Figure 36a. Aspect angle scan in vertical (y-z) plane. Horizontal ($\hat{\phi}$) polarization, frequency 8.02 GHz. ___ measured, --- calculated results.

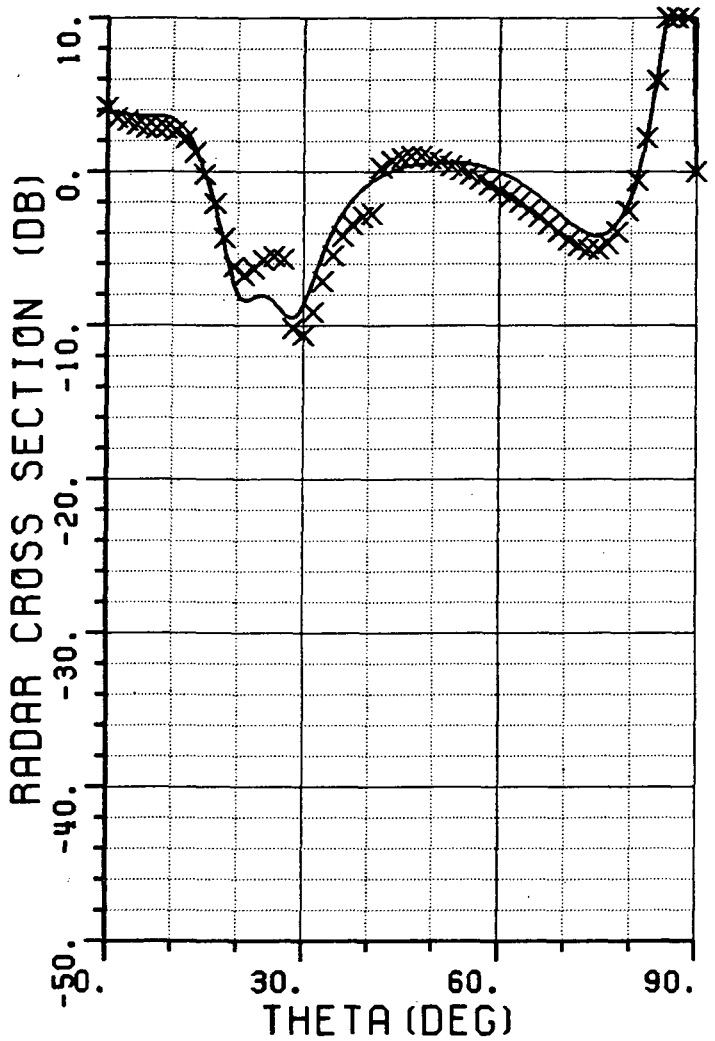


Figure 36b. Calculated aspect angle scans corresponding to Figure 36a.
___ All modes are included
xxx Only 3 modes are included

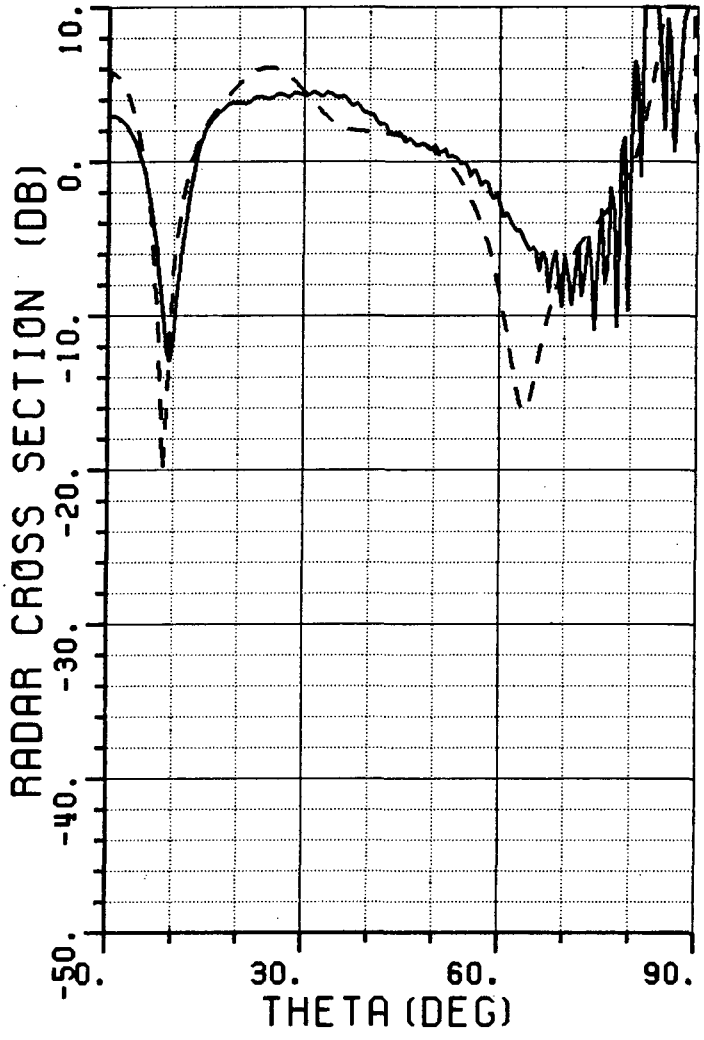


Figure 37a. Aspect angle scan in vertical (y-z) plane. Horizontal ($\hat{\phi}$) polarization, frequency 10.01 GHz. ___ measured, --- calculated results.

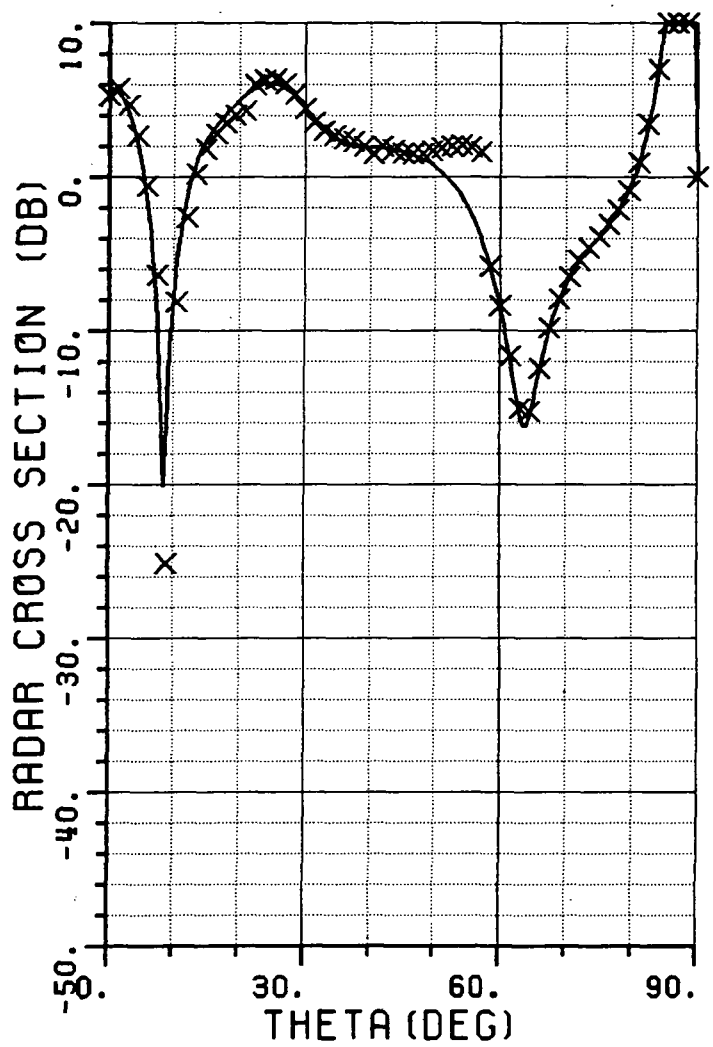


Figure 37b. Calculated aspect angle scans corresponding to Figure 37a.
___ All modes are included
xxx Only 3 modes are included

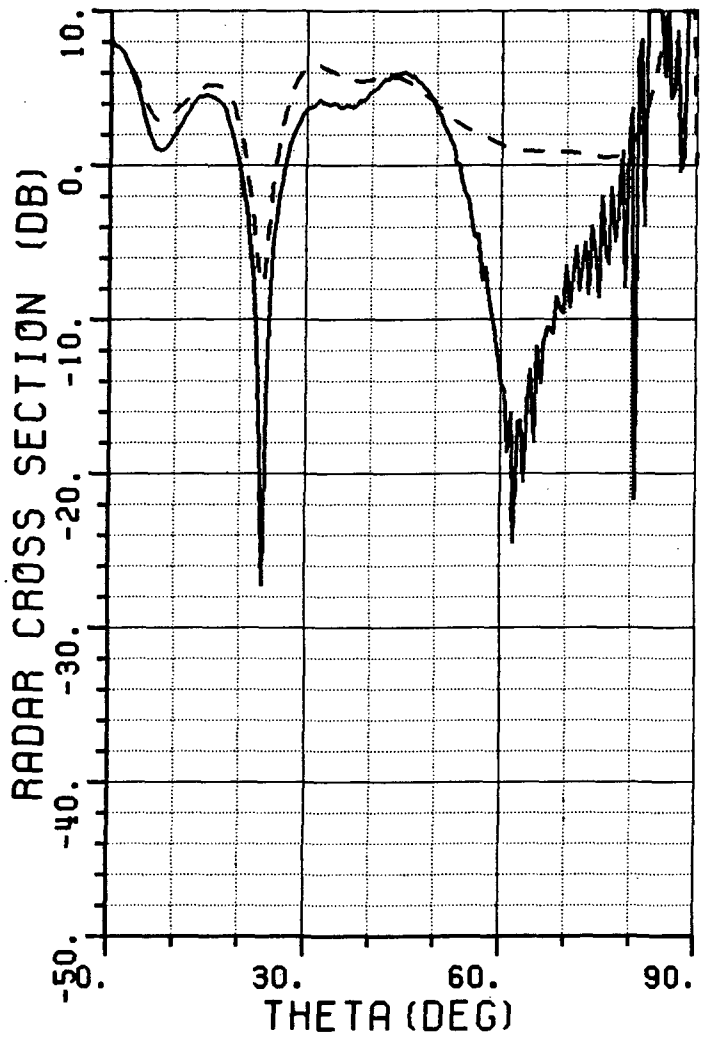


Figure 38a. Aspect angle scan in vertical (y-z) plane. Horizontal ($\hat{\phi}$) polarization, frequency 11.96 GHz. ___ measured, --- calculated results.

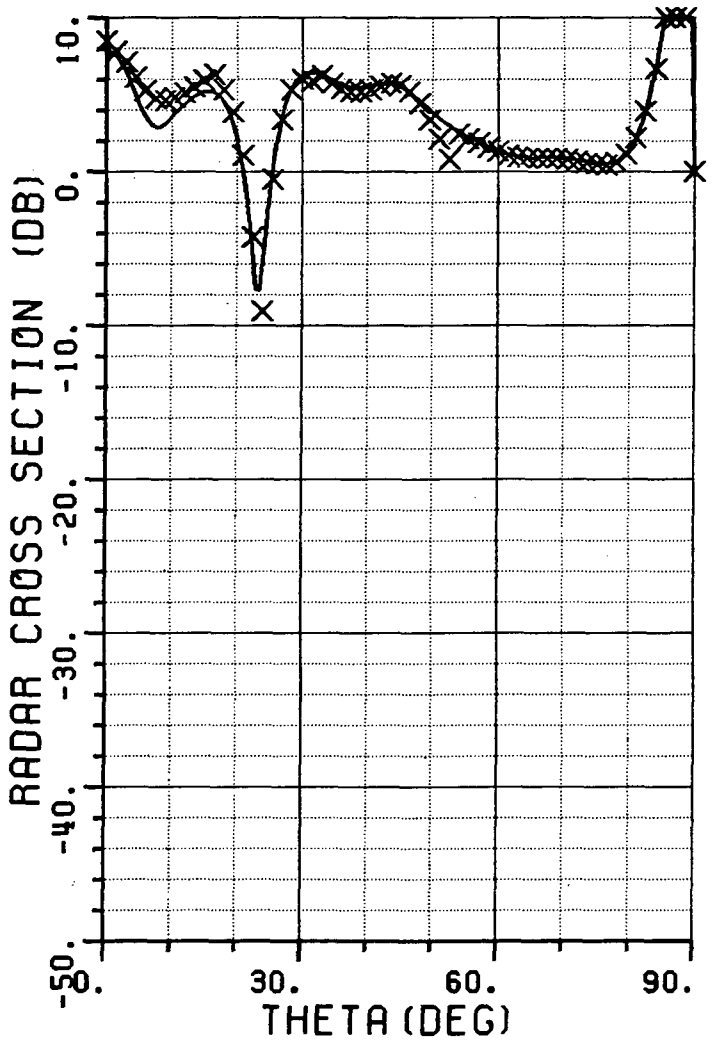


Figure 38b. Calculated aspect angle scans corresponding to Figure 38a.
___ All modes are included
xxx Only 3 modes are included

C-2

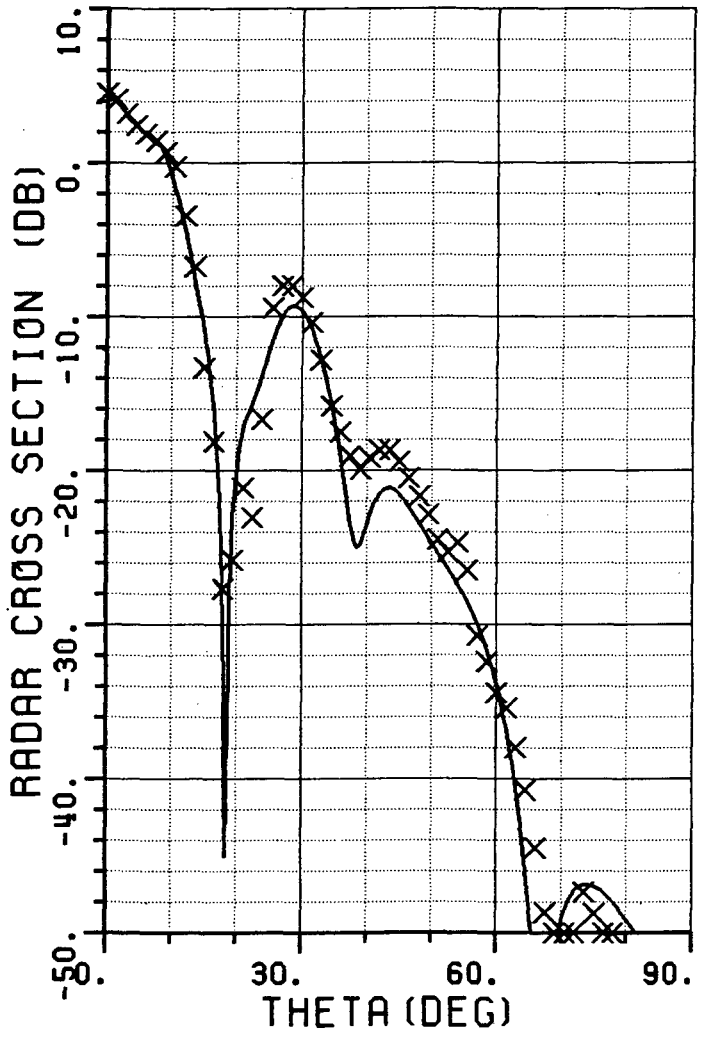


Figure 39. Calculated aspect angle scans in the plane ϕ=45°, $\hat{\phi}$ polarization, frequency = 10.0 GHz.

—— All 172 modes are included (86 TE, 86 TM modes)

xxx Only 18 modes are included (9 TE, 9 TM modes)

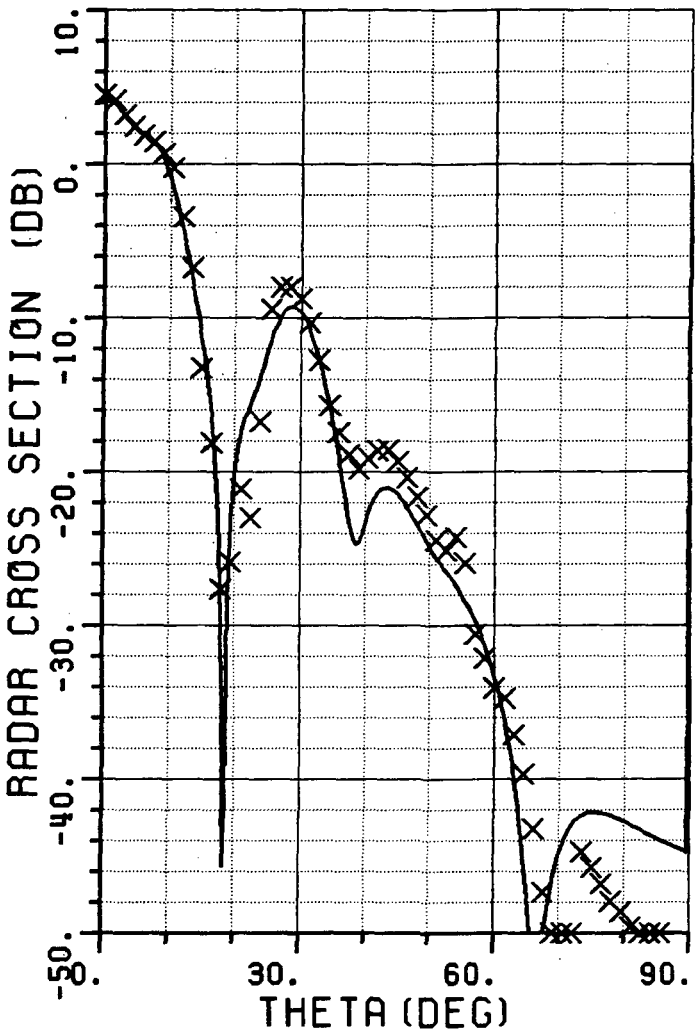


Figure 40. Calculated aspect angle scans in the plane ϕ=45°, $\hat{\theta}$ polarization, frequency = 10.0 GHz.

___ All 172 modes are included (86 TE, 86 TM modes)

xxx Only 18 modes are included (9 TE, 9 TM modes)

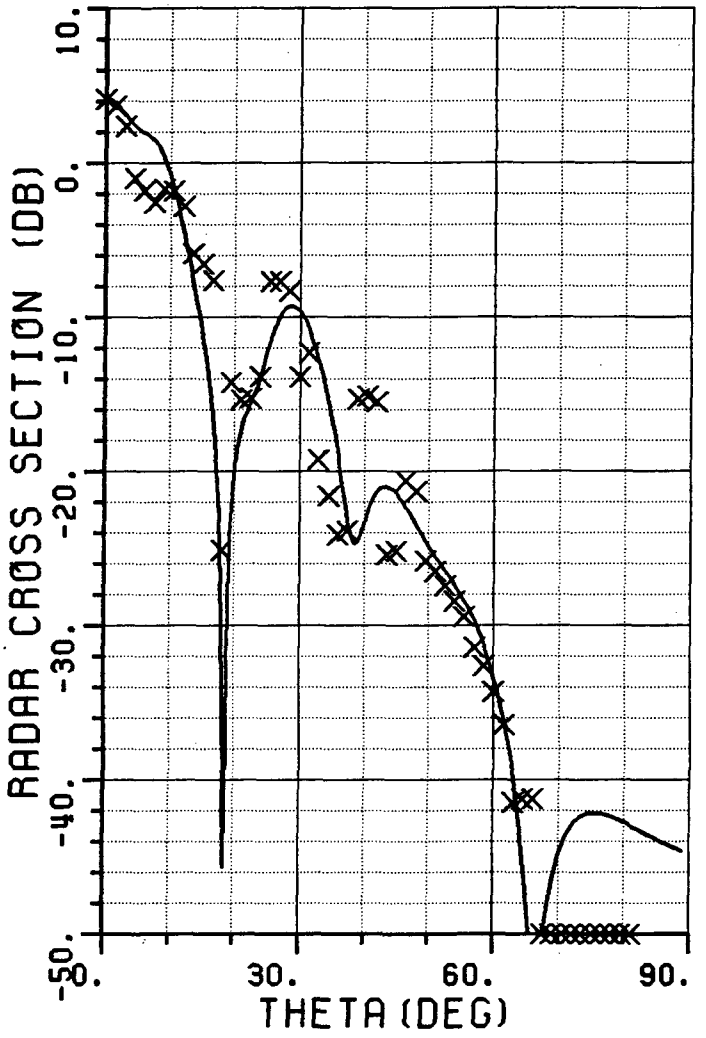


Figure 41. Calculated aspect angle scans in the plane ϕ=45°, $\hat{\theta}$ polarization, frequency = 10 GHz.

___ All 172 modes are included (86 TE, 86 TM modes)

xxx Only 6 modes are included (3 TE, 3 TM modes)

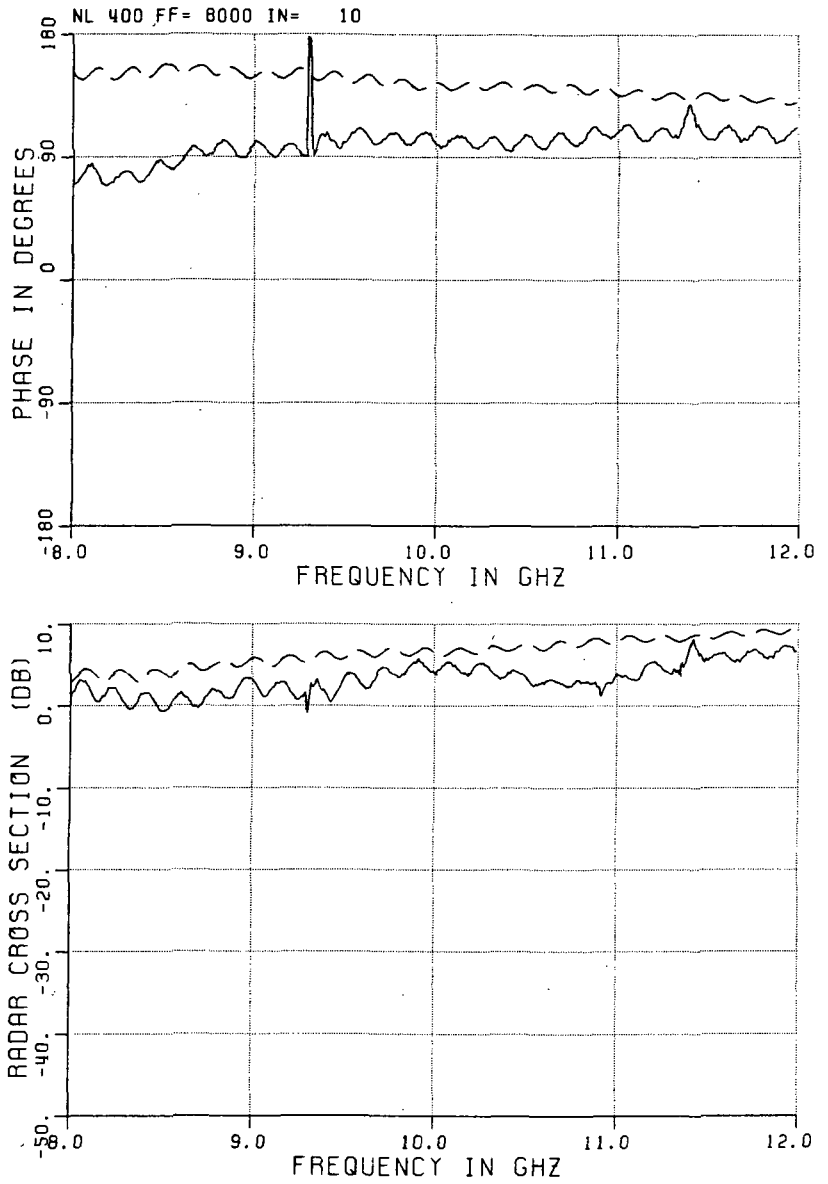


Figure 42a. Frequency scan in horizontal (x-z) plane. ϕ=0°, θ=0°, vertical ($\hat{\phi}$) polarization. ___ measured, --- calculated results.

ORIGINAL PAGE IS
OF POOR QUALITY

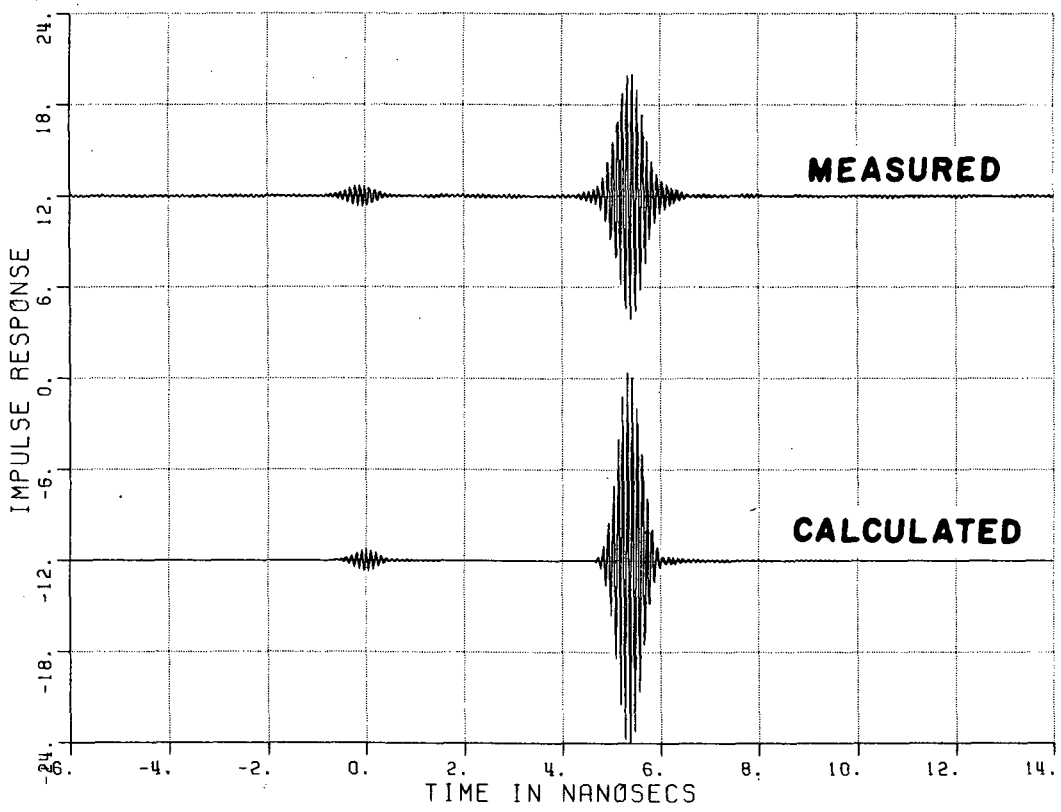


Figure 42b. Inverse Fourier transform.

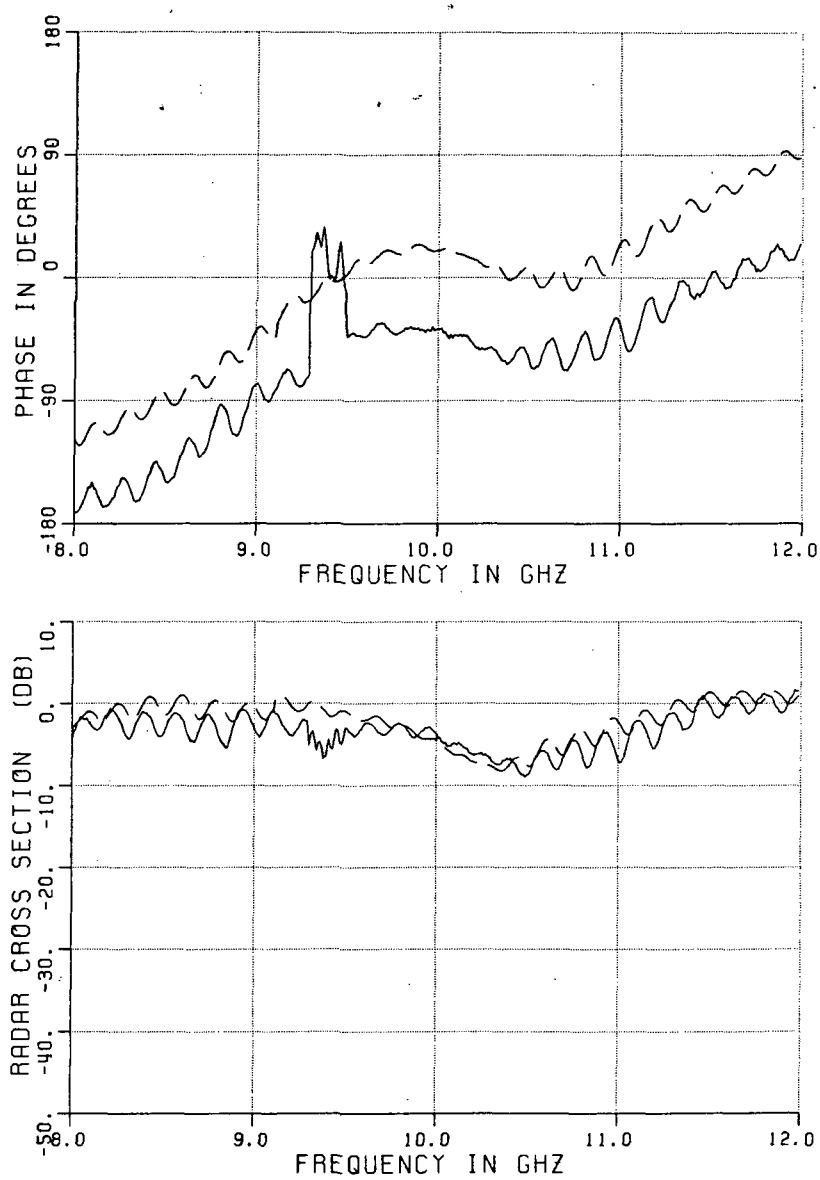


Figure 43a. Frequency scan in horizontal (x-z) plane. ϕ=0°, θ=15°, vertical ($\hat{\phi}$) polarization. ___ measured, --- calculated results.

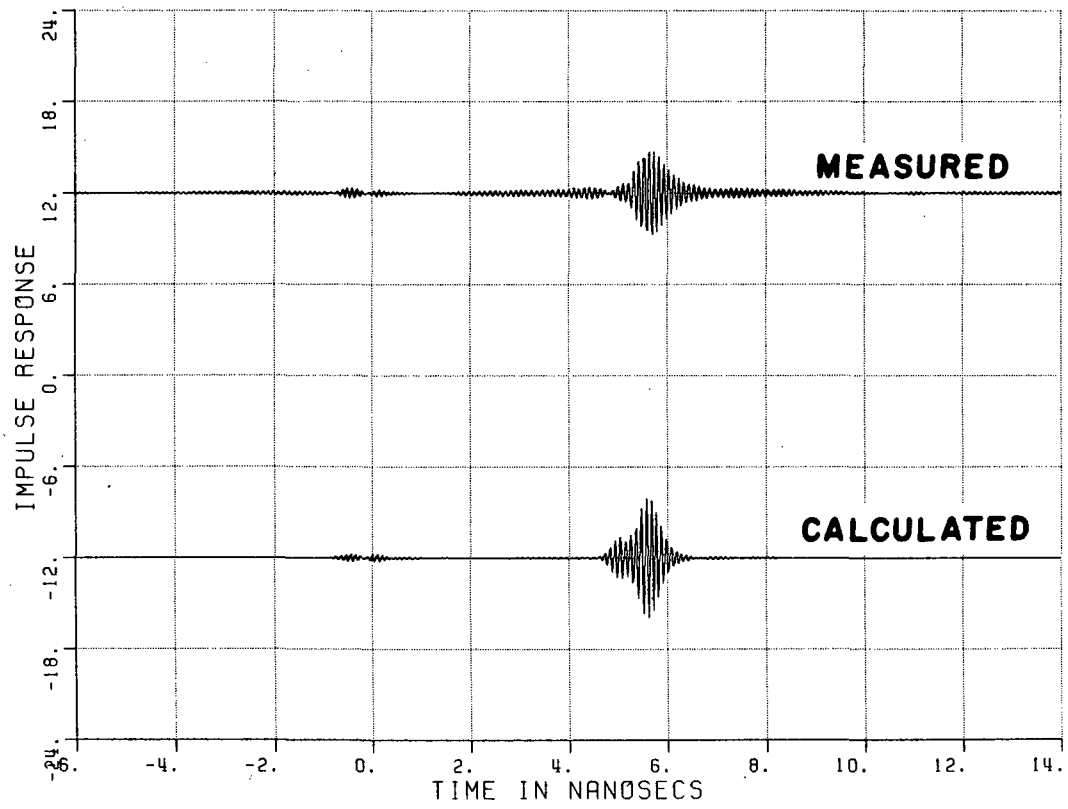


Figure 43b. Inverse Fourier transforms.

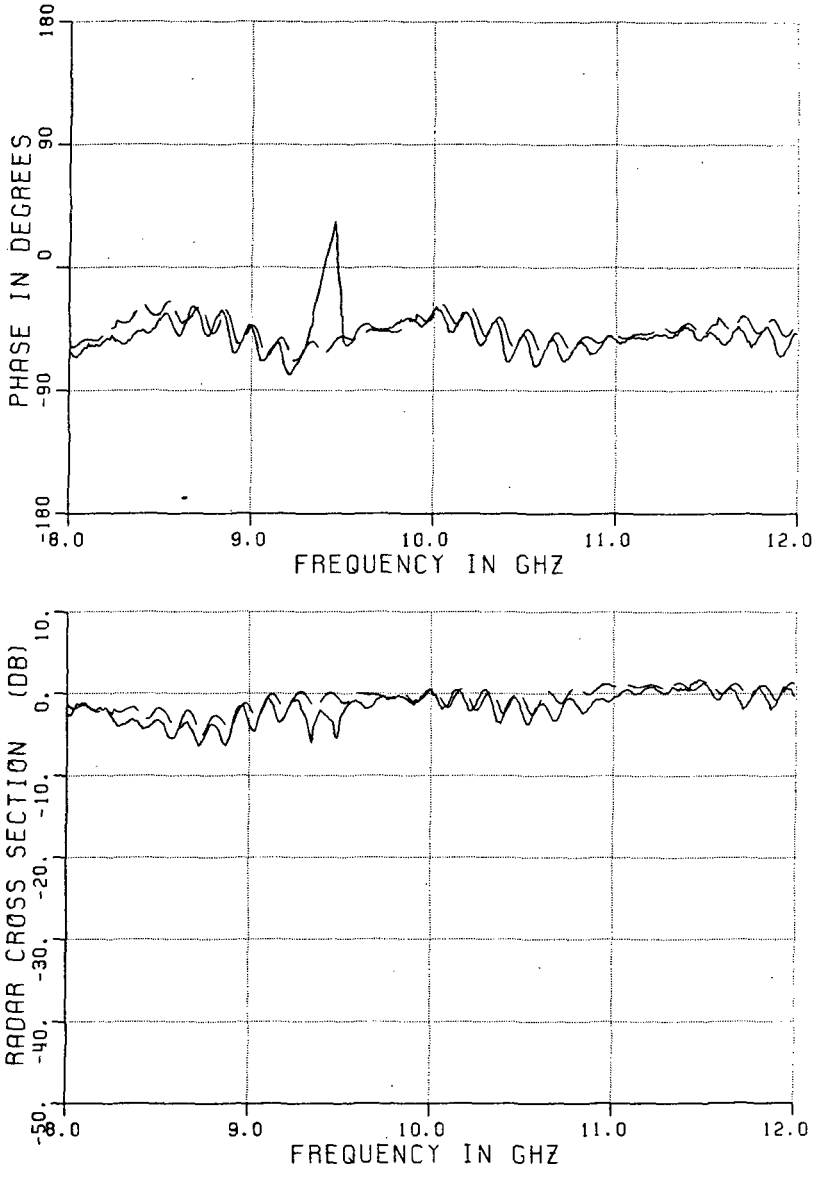


Figure 44a. Frequency scan in horizontal (x-z) plane.
ϕ=0°, θ=30°, vertical ($\hat{\phi}$) polarization.
—— measured, --- calculated results.

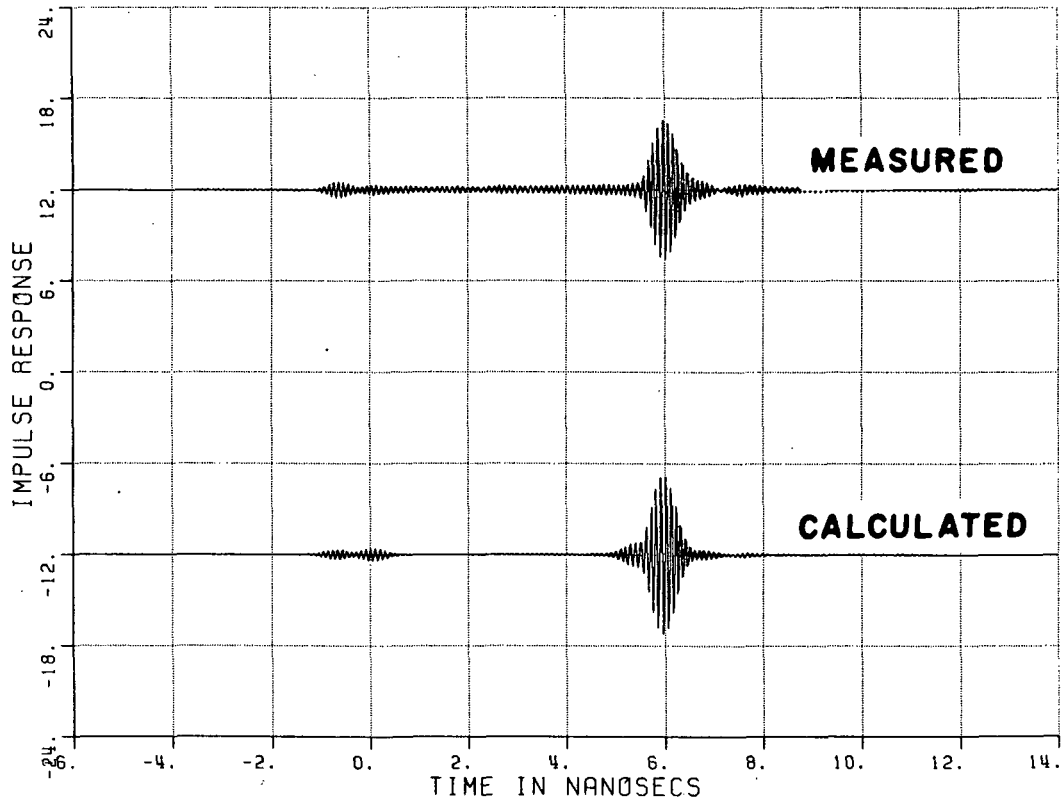


Figure 44b. Inverse Fourier transforms.

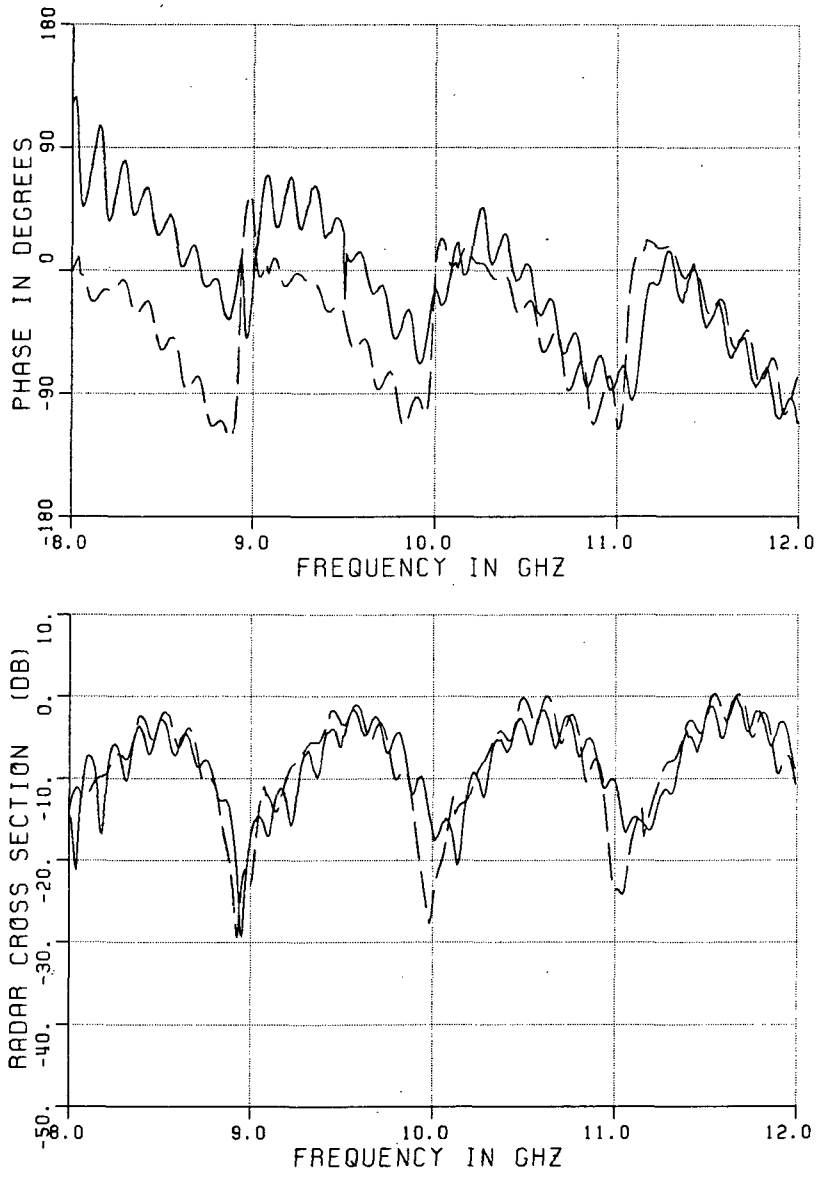


Figure 45a. Frequency scan in horizontal (x-z) plane. ϕ=0°, θ=45°, vertical ($\hat{\phi}$) polarization. ___ measured, --- calculated results.

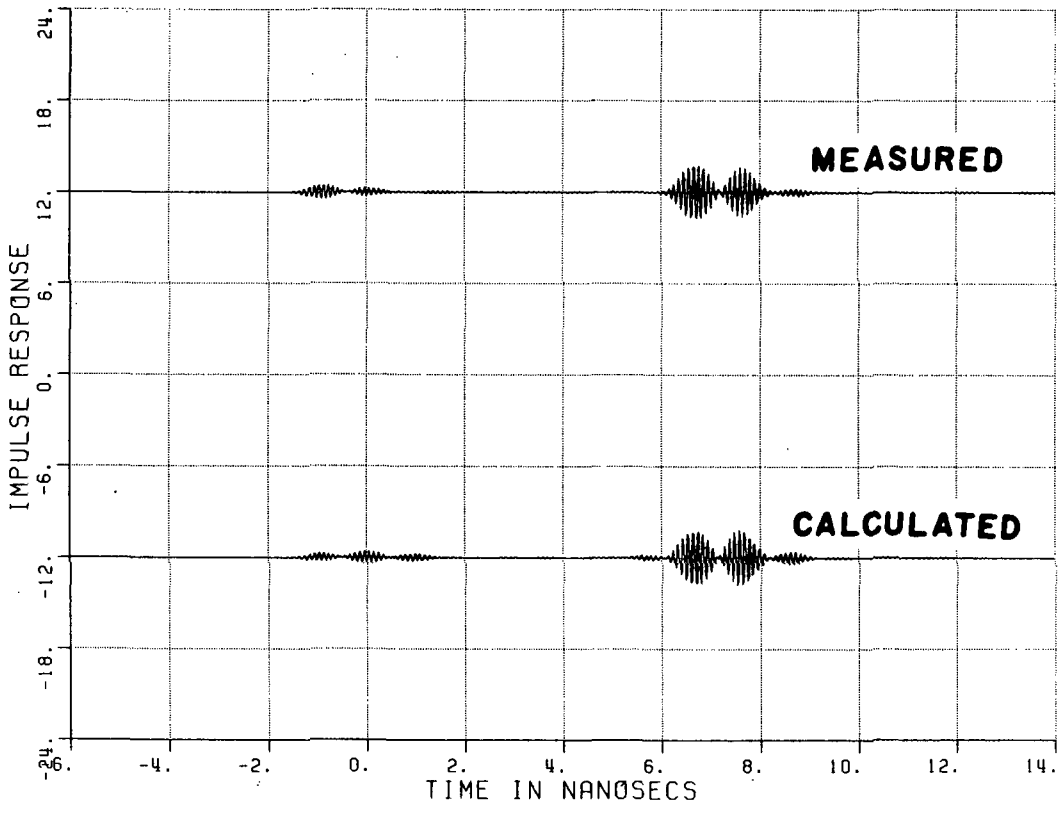


Figure 45b. Inverse Fourier transforms.

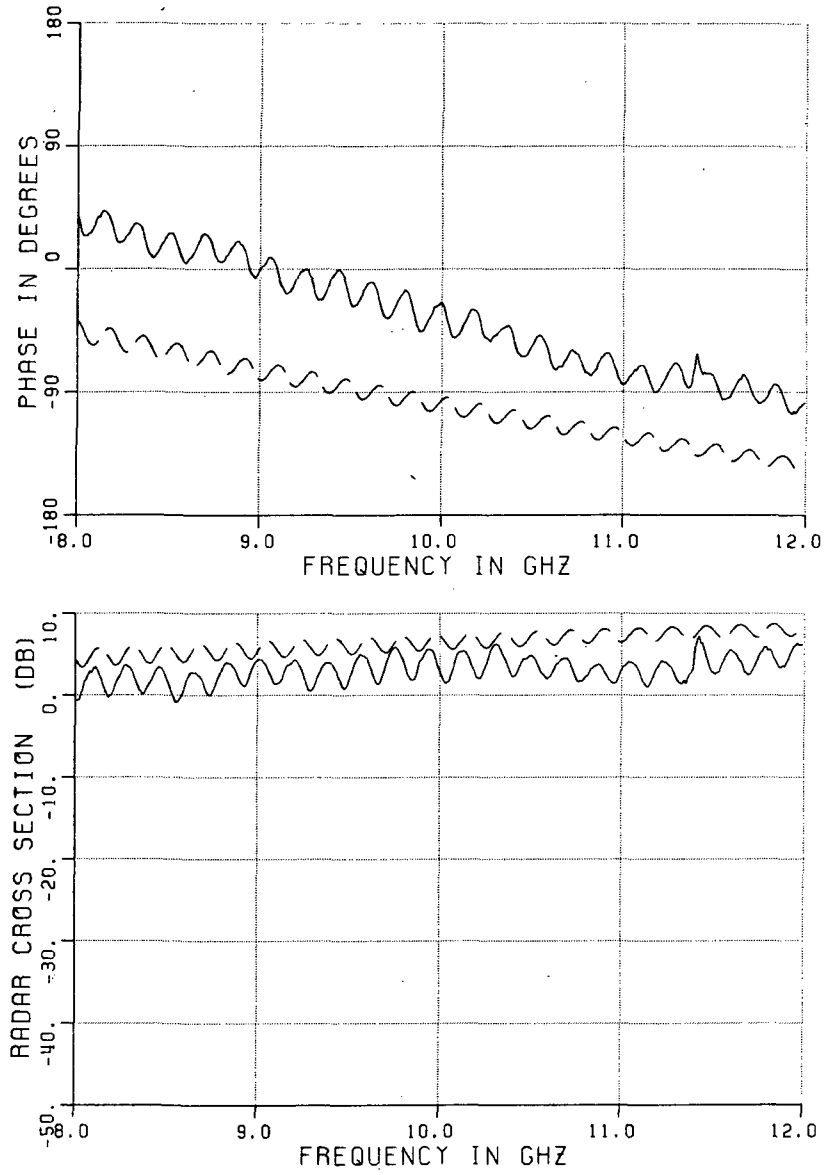


Figure 46a. Frequency scan in horizontal (x-z) plane. ϕ=0°, θ=0°, horizontal ($\hat{\theta}$) polarization. ___ measured, --- calculated results.

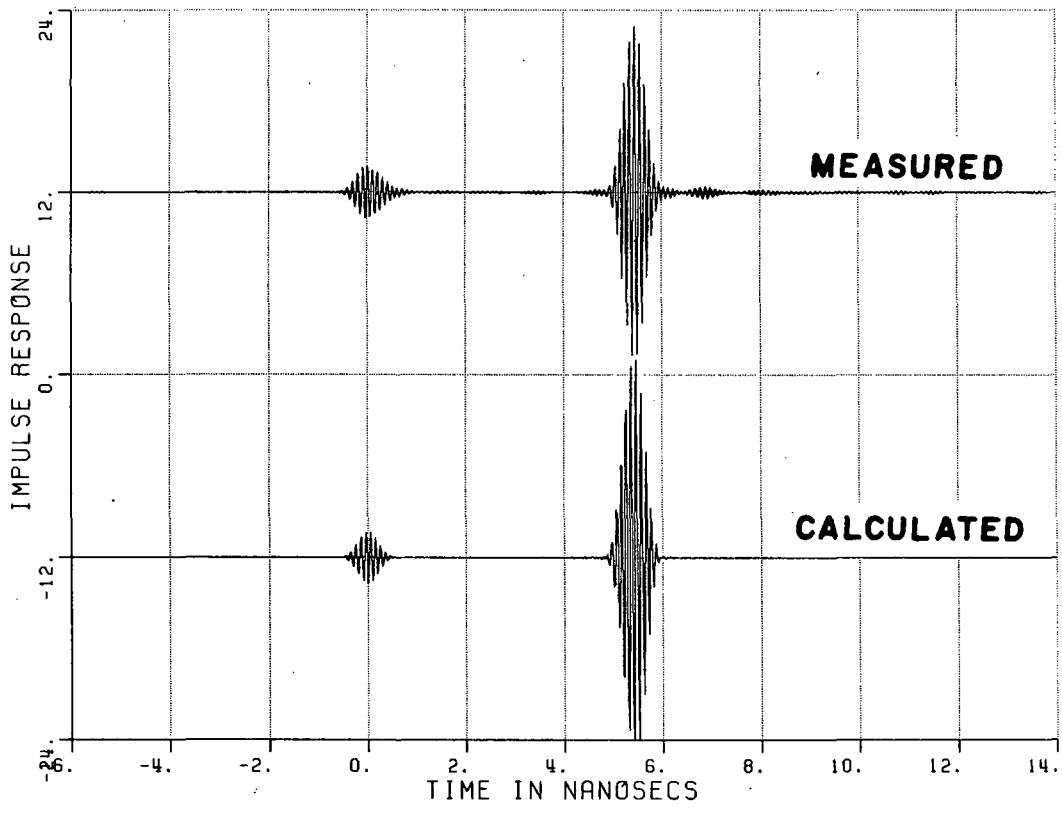


Figure 46b. Inverse Fourier transforms.

ORIGINAL PAGE IS
OF POOR QUALITY

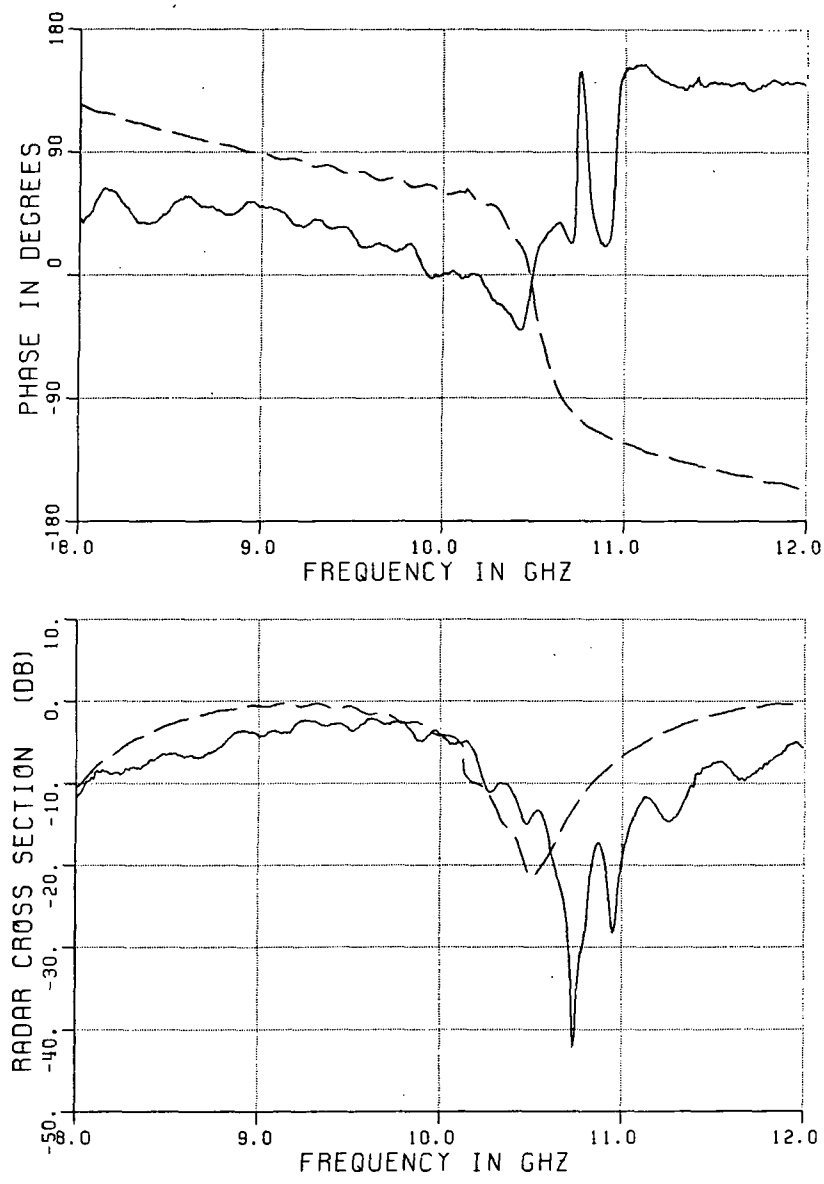


Figure 47a. Frequency scan in horizontal (x-z) plane. ϕ=0°, θ=15°, horizontal ($\hat{\theta}$) polarization. ___ measured, --- calculated results.

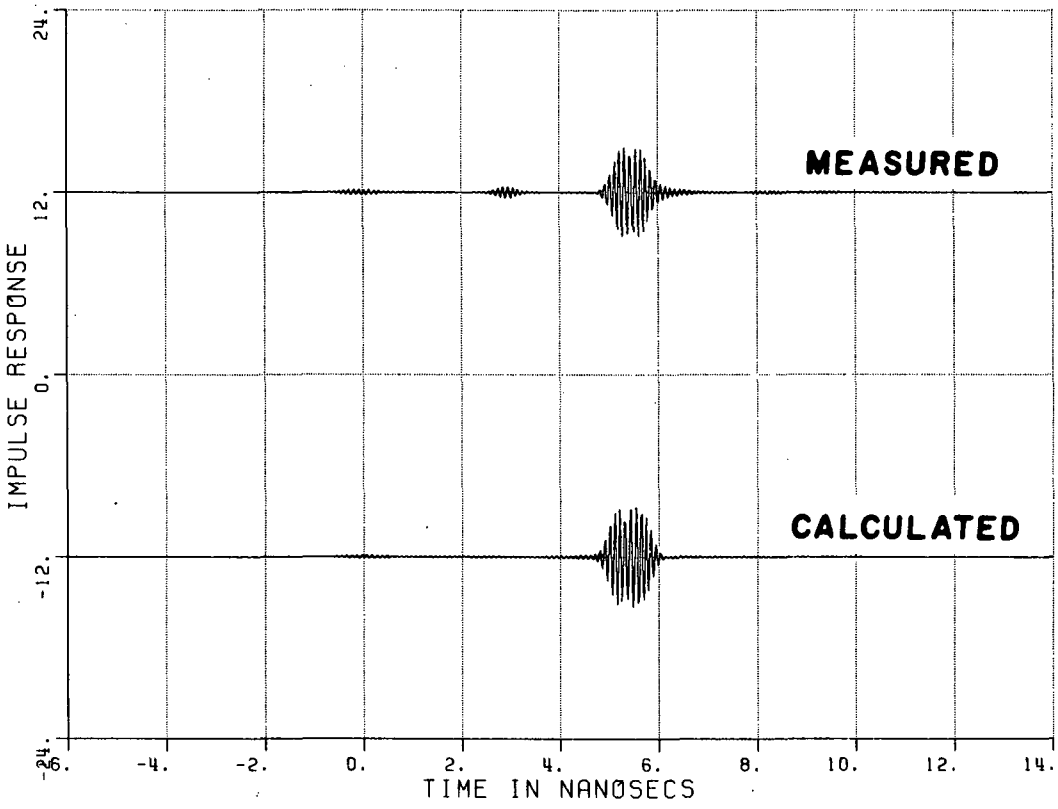


Figure 47b. Inverse Fourier transforms.

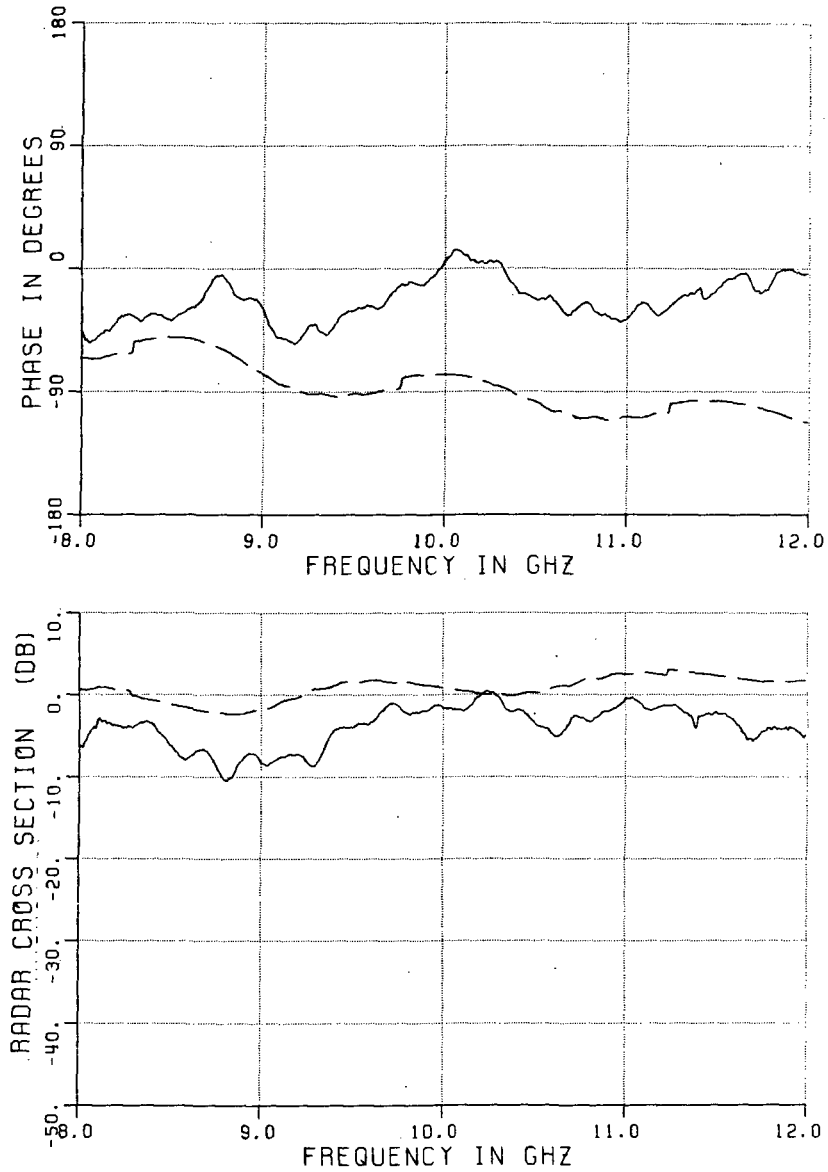


Figure 48a. Frequency scan in horizontal (x-z) plane. ϕ=0°, θ=30°, horizontal ($\hat{\theta}$) polarization. ___ measured, --- calculated results.

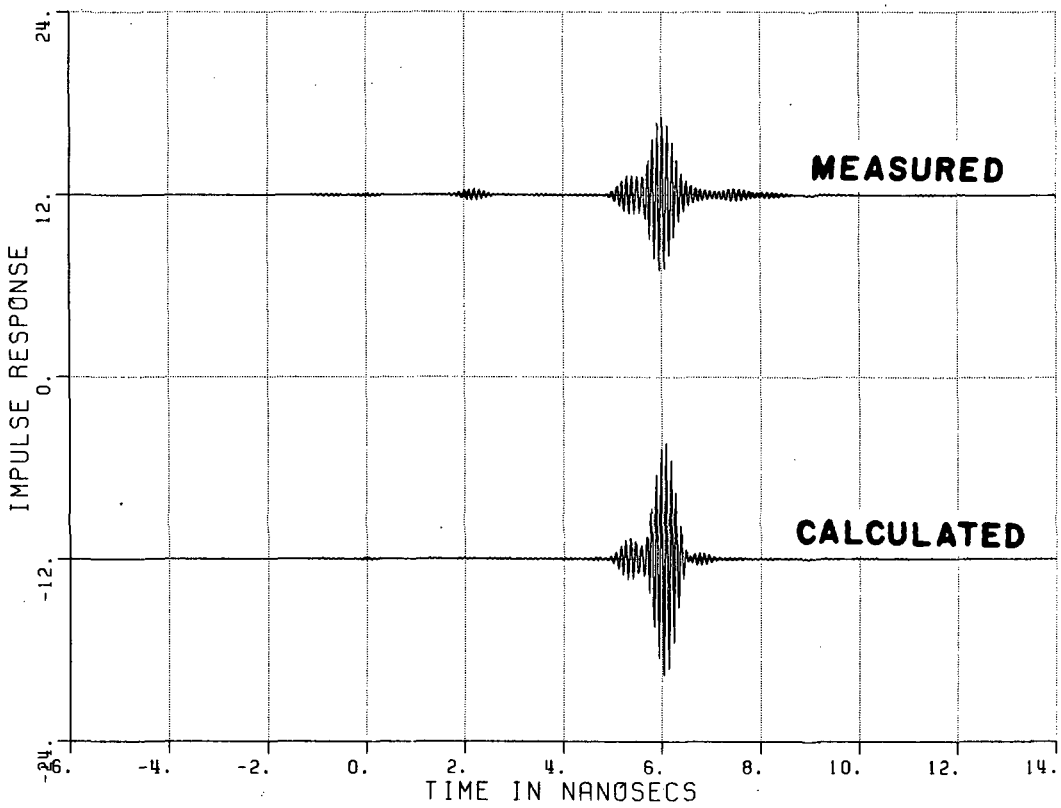


Figure 48b. Inverse Fourier transforms.

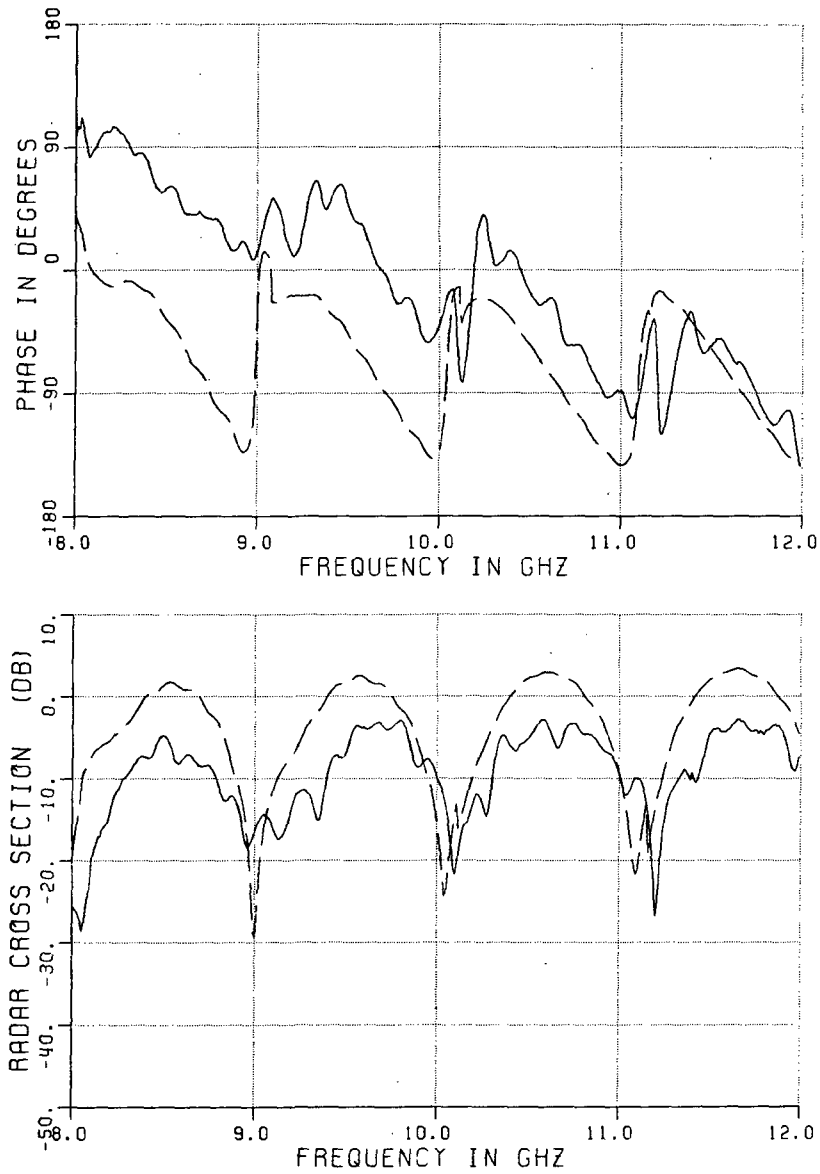


Figure 49a. Frequency scan in horizontal (x-z) plane. $\phi=0°$, $\theta=45°$, horizontal ($\hat{\theta}$) polarization. ___ measured, --- calculated results.

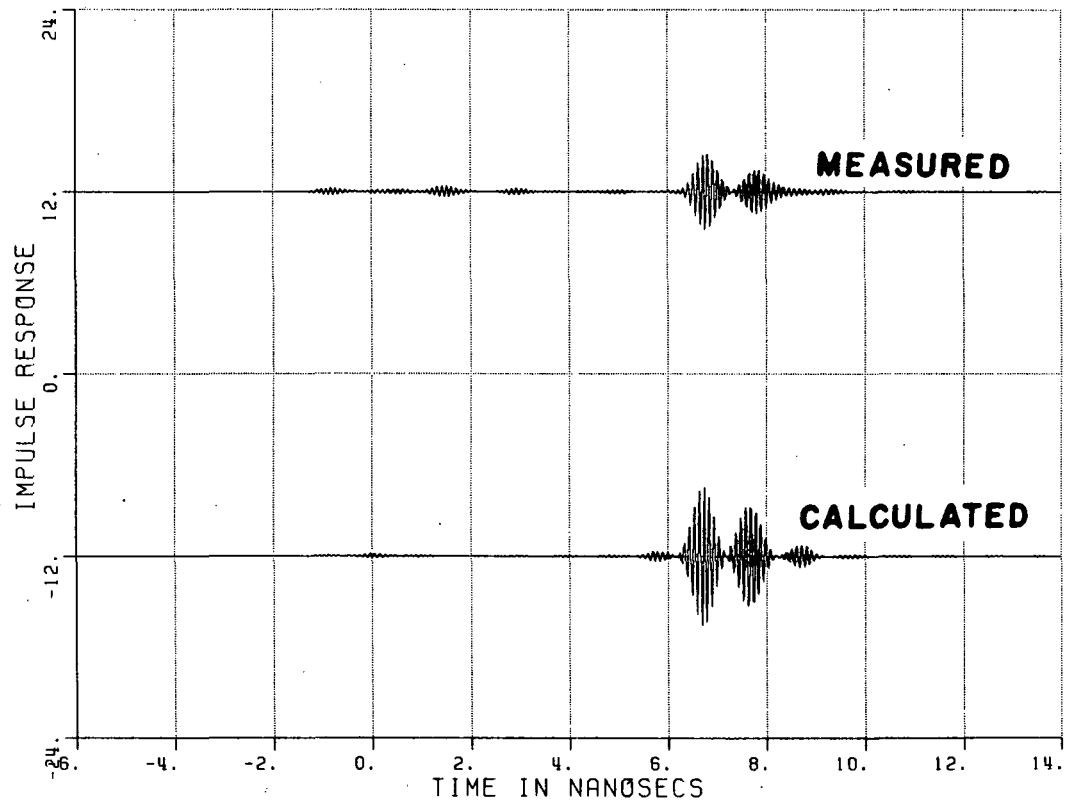


Figure 49b. Inverse Fourier transforms.

ORIGINAL PAGE IS
OF POOR QUALITY

ORIGINAL PAGE IS
OF POOR QUA

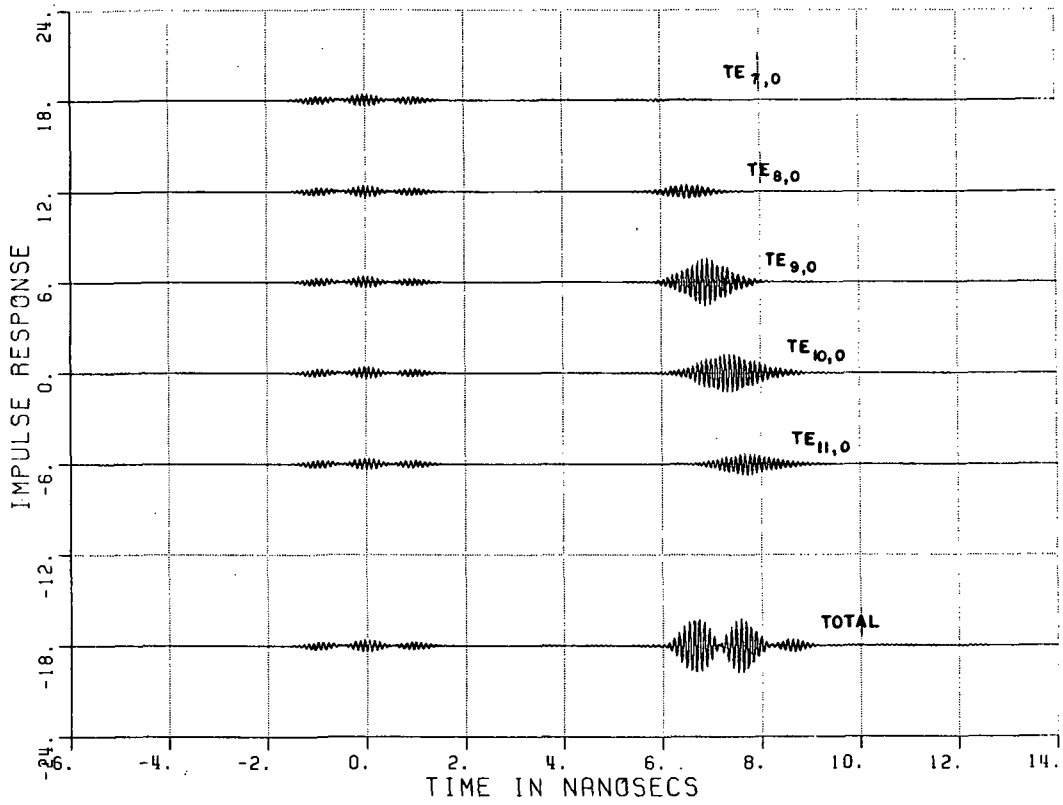


Figure 50. The separate returns of modes for the case in Figure 45b.

is received later in time, causing a stronger modal dispersion. Also note that the modal terms add up to form ripples in the total result from the cavity effect. If not understood correctly one might think this is indicating different scattering centers, which would not be true. This shows that modal propagation should carefully be traced if one wishes to obtain the true response for the cavity effects.

CHAPTER V

CONCLUSIONS

The goal of this research is to understand the dominant scattering mechanisms associated with a jet inlet structure and to develop some simple and accurate techniques to analyze them. Basically the backscattered field is composed of two major mechanisms; namely, the diffraction from the open end and radiation from the open end due to interior reflections or cavity effects. Both mechanisms are separately discussed, analyzed, and compared with aspect angle and frequency scan measured results. The analysis and numerical results for the diffraction by just the open end is presented in Chapter III. The results indicate that the GTD provides an accurate estimation of this diffraction term. Chapter IV deals with the analysis of interior cavity effects. The latter analysis is based on the expansion of the field inside the inlet in terms of rectangular waveguide modes. The coupling of the incident field into the waveguide modes and their subsequent radiation from the open end are obtained by an integration over the aperture at the open end. In appendix IV, it is shown that this aperture integration can be corrected in the same way as the PO is corrected via the PTD. However, the integration process does not give

any physical insight to the problem, and as the number of propagating modes increase with frequency it becomes cumbersome and inefficient. Therefore, in this research, new approaches to substantially improve the efficienty of these aperture integrals was investigated. It was shown that every mode can be decomposed into four ray-optical fields each of which is propagating in a particular direction. These directions are called the modal ray directions. It was determined that the modal radiation is strongest in these modal ray directions. Therefore, for a given radiation direction one can include only the radiation of those modes whose modal ray directions are closest to the radiation direction. Numerical results are included to indicate that the contribution of only three modes with modal ray directions closest to the given observation direction accurately approximates the contribution of all the propagating modes. This is an important result, because it combines modal radiation with ray-optics, and therefore it can be applied to many different and complex waveguide geometries to effectively select only the few significant modes from the entire set of propagating modes. Also, the same modal ray approach is useful in calculating the modal reflection and transmission from interior inlet discontinuities.

The model studied here had a small interior discontinuity, and, as expected, it did not seem to significantly influence the final results. It is proposed as a part of future research, to build and analyze a model with more pronounced interior discontinuities which might occur in practice.

REFERENCES

[1] R. Mittra and S.W. Lee, Analytical Techniques in the Theory of Guided Waves, The MacMillan Company, New York, 1971.

[2] P.H. Pathak, A. Altintas, C.D. Chuang and S. Barkeshli, "Near Field Scattering by Rectangular and Circular Inlet Configurations with an Impedance Surface Termination", Final Report 715267-1, The Ohio State University, ElectroScience Laboratory, prepared under contract No. N60530-83-M-40RD for Naval Weapons Center, China Lake, CA, July 1984.

[3] J.B. Keller, "Geometrical Theory of Diffraction", J. Opt. Soc. Amer., Vol. 52, pp. 116-130, 1962.

[4] R.G. Kouyoumjian, P.H. Pathak, and W.D. Burnisde, "A Uniform GTD for the Diffraction by Edges, Vertices, and Convex Surfaces", in Theoretical Methods for Determining the Interaction of Electromagnetic Waves with Structures, J.K. Skwirzynski, ed., Netherlands, Sijthoff and Noordhoff, 1981.

[5] H.Y. Yee, L.B. Felsen and J.B. Keller, "Ray Theory of Reflection from the Open End of a Waveguide," SIAM J. App. Math., Vol. 16, Nov. 2, pp. 268-300, 1968.

[6] P.H. Pathak, Techniques for High Frequency Problems, Chapter A7 in Handbook of Antenna Theory and Design, eds. Y.T. Lo and S.W. Lee, to be published by ITT-Howard W. Sams and Co., Inc.

[7] R.F. Harrington, Time Harmonic Electromagnetic Fields, McGraw Hill, New York 1961.

[8] M. Abramowitz and I.A. Stegun, Handbook of Mathematical Functions, Dover Publications Inc., New York, 1965.

APPENDIX I

MODAL FIELD EXPRESSIONS IN A RECTANGULAR WAVEGUIDE

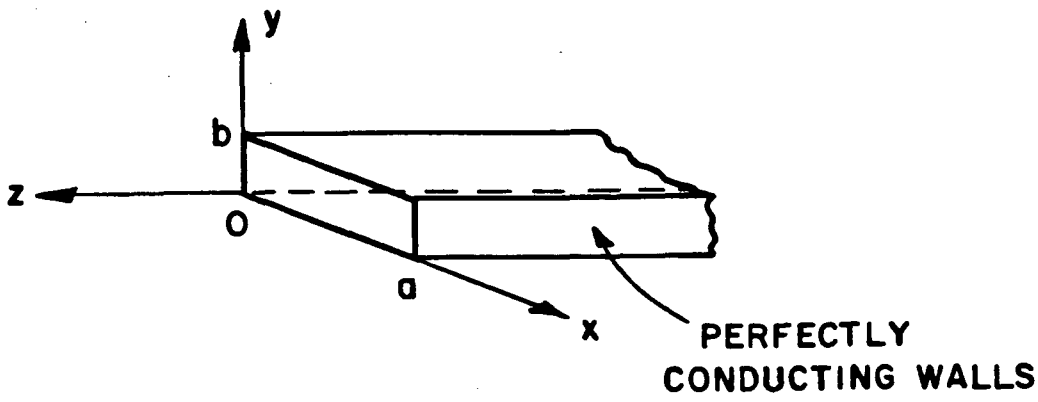


Figure A1. Rectangular waveguide geometry.

As described in [7], the modes in a rectangular waveguide as shown in Figure A.1, can be classified into sets of transverse fields to a coordinate direction.

The mode sets transverse to the axial ($\hat{z}$) direction are important and widely used, because it applies to uniform nonrectangular cross-section guides. However, in many problems, mode sets transverse to $\hat{x}$ or $\hat{y}$ coordinate may be more suitable.

These sets can be calculated from an axial or transverse vector potential [7]. The TE_{nm} and TM_{nm} to $\hat{z}$ type modal field expressions are given by:

	TE Modes	TE Modes	
h_z	$N^h_{nm} \frac{Y_o}{jk} (n_a^2+m_b^2) \cos n_a x \cos m_b y$	0	(A1)
e_z	0	$-N^e_{nm} \frac{1}{j\beta_{nm}} (n_a^2+m_b^2) \sin_a x \sin m_b y$	(A2)
h_x	$N^h_{nm} \frac{Y_o}{k} \beta_{nm} \sin n_a x \cos m_b y$	$-N^e_{nm} \frac{k}{\beta_{nm}} Y_o\, m_b \sin n_a x \cos m_b y$	(A3)
h_y	$N^h_{nm} \frac{Y_o}{k} \beta_{nm}\, m_b \cos n_a x \sin m_b y$	$N^e_{nm} \frac{k}{\beta_{nm}} Y_o\, n_a \cos n_a x \sin m_b y$	(A4)
e_x	$N^h_{nm}\, m_b \cos n_a x \sin m_b y$	$N^e_{nm}\, n_a \cos n_a x \sin m_b y$	(A5)
e_y	$-N^h_{nm}\, n_a \sin_a x \cos m_b y$	$+N^e_{nm}\, m_b \sin n_a x \cos m_b y$	(A6)
N^h_{nm}	$\left[\frac{\varepsilon_{on} \cdot \varepsilon_{om} \cdot k}{\beta_{nm} \cdot Y_o (n_a^2+m_b^2)}\right]^{1/2}$	-	(A7)
N^e_{nm}	-	$\left[\frac{\varepsilon_{on} \cdot \varepsilon_{om} \cdot \beta_{nm}}{k \cdot Y_o (n_a^2+m_b^2)}\right]^{1/2}$	(A8)
N_{nm}	N^h_{nm}	N^e_{nm}	
u	m_b	n_a	
v	n_a	$-m_b$	

where the normalization factors N^h_{nm} and N^e_{nm} are defined so as to

$$\int_0^a \int_0^b \bar{e} \times \bar{h} \cdot \hat{z} \, dx \, dy = 1 \tag{A9}$$

and

$$\varepsilon_{on} = \begin{cases} 1 \text{ if } n = 0 \\ 2 \text{ if } n \neq 0 \end{cases} \tag{A10}$$

$$n_a = \frac{n\pi}{a} \quad , \quad m_b = \frac{m\pi}{b} \tag{A11}$$

Also, $\beta_{nm} = \sqrt{k^2 - n_a^2 - m_b^2}$ is the propagation constant in z-direction, namely;

$$\bar{E}_{modal} = [e_x \hat{x} + e_y \hat{y} + e_z \hat{z}] \, e^{\mp j \beta nm z} \tag{A12}$$

$$\bar{H}_{modal} = [h_x \hat{x} + h_y \hat{y} + h_z \hat{z}] \, e^{\mp j \beta nm z} \tag{A13}$$

Finally, $Y_o = Z_o^{-1}$ is the free-space admittance.

The modal sets transverse to $\hat{x}$-axis can be written as follows:

	$TE_{x,nm}$ Modes	$TM_{x,nm}$ Modes	
e_x	0	$-N^e_{nm} \frac{(n_a^2+m_b^2)}{j\beta_{nm}} \frac{k^2-n_a^2}{j\beta_{nm}} \cos n_a x \sin m_b y$	(A14)
e_y	$-N^h_{nm} (n_a^2+m_b^2) \sin n_a x \cos m_b y$	$N^e_{nm} \frac{(n_a^2+m_b^2)}{j\beta_{nm}} \frac{n_a \cdot m_b}{j\beta_{nm}} \sin n_a x \cos m_b y$	(A15)
e_z	$N^h_{nm} \frac{(n_a^2+m_b^2)}{j\beta_{nm}} m_b \sin n_a x \sin m_b y$	$-N^e_{nm} \frac{(n_a^2+m_b^2)}{j\beta_{nm}} n_a \cdot \sin n_a x \sin m_b y$	(A16)
h_x	$N^h_{nm} \frac{Y_o(n_a^2+m_b^2)}{k\beta_{nm}} (k^2-n_a^2) \sin n_a x \cos m_b y$	0	(A17)
h_y	$-N^h_{nm} \frac{Y_o}{k\beta_{nm}} (n_a^2+m_b^2) n_a \cdot m_b \cos n_a x \sin m_b y$	$N^e_{nm} \frac{(n_a^2+m_b^2)}{j\beta_{nm}} jkY_o \cos n_a x \sin m_b y$	(A18)
h_z	$N^h_{nm} \frac{Y_o}{jk} (n_a^2+m_b^2) n_a \cos n_a x \cos m_b y$	$N^e_{nm} \frac{(n_a^2+m_b^2)}{j\beta_{nm}} \frac{kY_o}{\beta_{nm}} m_b \cos n_a x \cos m_b y$	(A19)

From Equations (A1) through (A19), one can easily conclude that

$$TE_{x,nm} = n_a \, TE_{nm} - m_b \frac{k}{\beta_{nm}} TM_{nm} \tag{A20}$$

$$TM_{x,nm} = m_b \frac{k}{\beta_{nm}} TE_{nm} + n_a \, TM_{nm} \tag{A21}$$

or, alternatively,

$$TE_{nm} = \frac{1}{n_a^2 + m_b^2 \frac{k^2}{\beta_{nm}^2}} \left[n_a \, TE_{x,nm} + m_b \frac{k}{\beta_{nm}} TM_{x,nm} \right] \tag{A22}$$

$$TM_{nm} = \frac{1}{n_a^2 + m_b^2 \frac{k^2}{\beta_{nm}}} \left[-m_b \frac{k}{\beta_{nm}} TE_{x,nm} + n_a \, TM_{x,nm} \right] \tag{A23}$$

APPENDIX II

MODAL FIELD EXPRESSIONS IN A LINEARLY TAPERED WAVEGUIDE

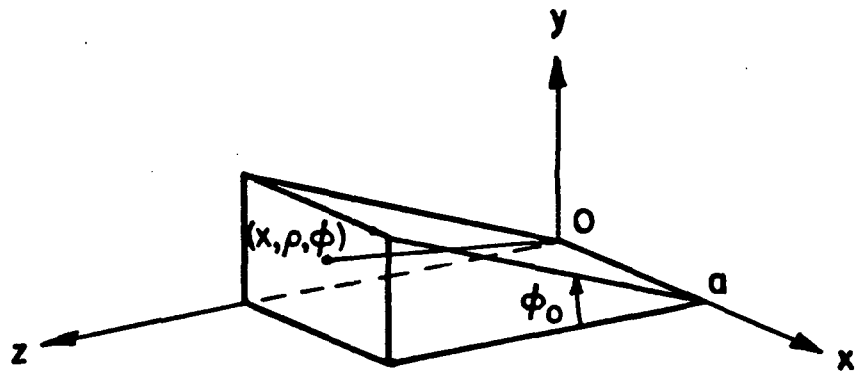


Figure A2. Geometry of a linearly tapered waveguide.

In this problem, it is possible to find mode sets transverse to $\hat{x}$-axis. The fields can be computed from the scalar function

$$\left[\frac{\partial^2}{\partial y^2} + \frac{\partial^2}{\partial z^2} + \left[k^2 - \left(\frac{n\pi}{a}\right)^2\right]\right]\psi = 0 \qquad \text{(A24)}$$

with appropriate boundary conditions. ψ is the x-component of the magnetic vector potential $\bar{A}$ in the TM_x case and the x-component of the electric vector potential $\bar{F}$ in the TE_x case [7].

Case 1 TE_x modes: These modes satisfy the relation $E_x=0$ and can be derived from $\bar{F}=\hat{x}\psi$.

The field components are given by;

$$E_\rho = \frac{-1}{\rho}\frac{\partial\psi}{\partial\phi} \qquad H_\rho = \frac{1}{jkZ_o}\frac{\partial^2\psi}{\partial\rho\partial x} \tag{A25}$$

$$E_\phi = \frac{\partial\psi}{\partial\rho} \qquad H_\phi = \frac{1}{jkZ_o}\frac{1}{\rho}\frac{\partial^2\psi}{\partial\phi\partial x} \tag{A26}$$

$$E_x = 0 \qquad H_x = \frac{1}{jkZ_o}\left(\frac{\partial^2}{\partial x^2} + k^2\right)\psi \tag{A27}$$

The appropriate scalar function ψ is given by;

$$\psi_{nm} = \sin\left(\frac{n\pi}{a}x\right)\cos\left(\frac{m\pi}{\phi_o}\phi\right)\begin{bmatrix} H^{(1)}_{\frac{m\pi}{\phi_o}}(k_t\rho) & \text{Ingoing Wave} \\ H^{(2)}_{\frac{m\pi}{\phi_o}}(k_t\rho) & \text{Outgoing Wave}\end{bmatrix} \tag{A28}$$

where

$$k_t^2 = k^2 - \left(\frac{n\pi}{a}\right)^2 \tag{A29}$$

The explicit expressions for the outgoing field components are given by;

$$E_\rho = \frac{1}{\rho}\frac{m\pi}{\phi_o}\sin\left(\frac{n\pi}{a}x\right)\sin\left(\frac{m\pi}{\phi_o}\phi\right)H^{(2)}_{\frac{m\pi}{\phi_o}}(k_t\rho) \tag{A30}$$

$$E_\phi = \sin\left(\frac{n\pi}{a}x\right)\cos\left(\frac{m\pi}{\phi_o}\phi\right)\frac{d}{d\rho}H^{(2)}_{\frac{m\pi}{\phi_o}}(k_t\rho) \tag{A31}$$

$$E_x = 0 \tag{A32}$$

$$H_\rho = \frac{1}{jkZ_o}\left(\frac{n\pi}{a}\right)\cos\left(\frac{n\pi}{a}x\right)\cos\left(\frac{m\pi}{\phi_o}\phi\right)\frac{d}{d\rho}\,H^{(2)}_{\frac{m\pi}{\phi_o}}(k_t\rho) \tag{A33}$$

$$H_\phi = -\frac{1}{jkZ_o}\frac{1}{\rho}\left(\frac{m\pi}{\phi_o}\right)\left(\frac{n\pi}{a}\right)\cos\left(\frac{n\pi}{a}x\right)\sin\left(\frac{m\pi}{\phi_o}\phi\right)H^{(2)}_{\frac{m\pi}{\phi_o}}(k_t\rho) \tag{A34}$$

$$H_x = \frac{1}{jkZ_o}k_t^2\sin\left(\frac{n\pi}{a}x\right)\cos\left(\frac{m\pi}{\phi_o}\phi\right)H^{(2)}_{\frac{m\pi}{\phi_o}}(k_t\rho) \tag{A35}$$

For small ϕ_o and large ρ, the Debye Asymptotic approximation for the Hankel function [8]

$$H^{(1)}_{\nu}(z) \sim \sqrt{\frac{2}{\pi\nu\sqrt{(\frac{z}{\nu})^2-1}}}\;e^{\pm j\left[\nu\sqrt{(\frac{z}{y})^2-1}\;-\nu\cos^{-1}\frac{\nu}{z}\;-\;\frac{\pi}{4}\right]} \tag{A36}$$

can be used. For small $\frac{\nu}{z}$; $\cos^{-1}\frac{\nu}{z} \to \frac{\pi}{2}$, so the above relation becomes;

$$H^{(1)}_{\nu}(z) \sim \sqrt{\frac{2}{\pi\sqrt{z^2-\nu^2}}}\;(\mp j)^{\nu}\,e^{\pm j\sqrt{z^2-\nu^2}}\;e^{\pm j\frac{\pi}{4}} \tag{A37}$$

and

$$\frac{d}{dz}H^{(1)}_{\nu}(z) \sim \sqrt{\frac{2}{\pi\sqrt{z^2-\nu^2}}}\;(\mp j)^{\nu}\left[\mp j\sqrt{1-(\frac{\nu}{z})^2}\;e^{\pm j\sqrt{z^2-\nu^2}}\right]e^{\mp j\frac{\pi}{4}} \tag{A38}$$

which goes to the large argument form [7] for $z \gg \nu$.

If one makes use of Equations (A37) and (A38) in the field expressions of Equations (A30) through (A35), one obtains the following expressions (up to a common factor) for an outgoing wave;

$$E_\rho = \frac{m\pi}{\rho\phi_o} \frac{1}{\sqrt{\beta_{nm}\rho}} \sin\left(\frac{n\pi}{a}x\right) \sin\left(\frac{m\pi}{\phi_o}\phi\right) e^{-j\beta_{nm}\rho} \tag{A39}$$

$$E_\phi = \frac{1}{\sqrt{\beta_{nm}\rho}} \sin\left(\frac{n\pi}{a}x\right) \cos\left(\frac{m\pi}{\phi_o}\phi\right) (-j\beta_{nm}) e^{-j\beta_{nm}\rho} \tag{A40}$$

$$E_x = 0 \tag{A41}$$

$$H_\rho = \frac{1}{jkZ_o} \left(\frac{n\pi}{a}\right) (-j\beta_{nm}) \frac{1}{\sqrt{\beta_{nm}\rho}} \cos\left(\frac{n\pi}{a}x\right) \cos\left(\frac{m\pi}{\phi_o}\phi\right) e^{-j\beta_{nm}\rho} \tag{A42}$$

$$H_\phi = \frac{1}{jkZ_o} \left(\frac{n\pi}{a}\right) \left(\frac{m\pi}{\rho\phi_o}\right) \frac{1}{\sqrt{\beta_{nm}\rho}} \cos\left(\frac{n\pi}{a}x\right) \sin\left(\frac{m\pi}{\phi_o}\phi\right) e^{-j\beta_{nm}\rho} \tag{A43}$$

$$H_z = \frac{1}{jkZ_o} \left(k^2-\left(\frac{n\pi}{a}\right)^2\right) \frac{1}{\sqrt{\beta_{nm}\rho}} \sin\left(\frac{n\pi}{a}x\right) \cos\left(\frac{m\pi}{\phi_o}\phi\right) e^{-j\beta_{nm}\rho} \tag{A44}$$

where

$$\beta_{nm}^2 = k^2 - \left(\frac{n\pi}{a}\right)^2 - \left(\frac{m\pi}{\rho\phi_o}\right)^2 \tag{A45}$$

is the function determining the phase advance in ρ-direction. Note that β_{nm} is a function of ρ. By comparing Equations (A39) through (A44) with Equations (A14) through (A19), one can see that the expressions of slightly tapered waveguide fields may be approximated by TE_x, TM_x-type rectangular waveguide mode sets. To do this, one has to make the following approximations.

$$\rho \rightarrow z \tag{A46}$$

$$\rho\phi \rightarrow y \tag{A47}$$

$$\rho\phi_o \rightarrow b \tag{A48}$$

together with Equation (A45) where ρ-dependence cannot be approximated by Equation (A48), since it is the function determining the phase advance which is more sensitive to the approximations.

Case 2 TM_x modes: These modes satisfy the relation $H_x=0$ and can be derived from $\bar{A}=\hat{x}\psi$.

The field components are given by:

$$E_\rho = \frac{1}{jkY_o} \frac{\partial^2\psi}{\partial\rho\partial x} \qquad H_\rho = \frac{1}{\rho} \frac{\partial\psi}{\partial\phi} \tag{A49}$$

$$E_\phi = \frac{1}{jkY_o} \frac{1}{\rho} \frac{\partial^2\psi}{\partial\phi\partial x} \qquad H_\phi = -\frac{\partial\psi}{\partial\rho} \tag{A50}$$

$$E_x = \frac{1}{jkY_o} \left(\frac{\partial^2}{\partial x^2} + k^2\right) \psi \qquad H_x = 0 \tag{A51}$$

The appropriate scalar function ψ is given by:

$$\psi = \cos\left(\frac{n\pi}{a}x\right) \sin\left(\frac{m\pi}{\phi_o}\phi\right) \begin{bmatrix} H^{(1)}_{\frac{m\pi}{\phi_o}}(k_t\rho) & \text{Ingoing Wave} \\ H^{(2)}_{\frac{m\pi}{\phi_o}}(k_t\rho) & \text{Outgoing Wave} \end{bmatrix} \tag{A52}$$

The explicit expressions for the outgoing field components are given by:

$$E_\rho = \frac{-1}{jkY_o} \left(\frac{n\pi}{a}\right) \sin\left(\frac{n\pi}{a}x\right) \sin\left(\frac{m\pi}{\phi_o}\phi\right) \frac{d}{d\rho} H^{(2)}_{\frac{m\pi}{\phi_o}}(k_t\rho) \tag{A53}$$

$$E_\phi = \frac{-1}{jkY_o} \frac{1}{\rho} \left(\frac{n\pi}{a}\right) \left(\frac{m\pi}{\phi_o}\right) \sin\left(\frac{n\pi}{a}x\right) \cos\left(\frac{m\pi}{\phi_o}\phi\right) H^{(2)}_{\frac{m\pi}{\phi_o}}(k_t\rho) \tag{A54}$$

$$E_x = \frac{1}{jkY_o} \left(k^2-\left(\frac{n\pi}{a}\right)^2\right) \cos\left(\frac{n\pi}{a}x\right) \sin\left(\frac{m\pi}{\phi_o}\phi\right) H^{(2)}_{\frac{m\pi}{\phi_o}}(k_t\rho) \tag{A55}$$

$$H_\rho = \frac{1}{\rho} \left(\frac{m\pi}{\phi_o}\right) \cos\left(\frac{n\pi}{a}x\right) \cos\left(\frac{m\pi}{\phi_o}\phi\right) H^{(2)}_{\frac{m\pi}{\phi_o}}(k_t\rho) \tag{A56}$$

$$H_\phi = - \cos\left(\frac{n\pi}{a}x\right) \sin\left(\frac{m\pi}{\phi_o}\phi\right) \frac{d}{d\rho} H^{(2)}_{\frac{m\pi}{\phi_o}}(k_t\rho) \tag{A57}$$

$$H_x = 0 \tag{A58}$$

Again using Debye's Asymptotic form for the Hankel function, one obtains the following field expressions:

$$E_\rho = - \frac{1}{jkY_o} \left(\frac{n\pi}{a}\right) \frac{1}{\sqrt{\beta_{nm}\rho}} \sin\left(\frac{n\pi}{a}x\right) \sin\left(\frac{m\pi}{\phi_o}\phi\right) (-j\beta_{nm}) e^{-j\beta_{nm}\rho} \tag{A59}$$

$$E_\phi = - \frac{1}{jkY_o} \left(\frac{n\pi}{a}\right) \left(\frac{m\pi}{\phi_o}\right) \frac{1}{\sqrt{\beta_{nm}\rho}} \sin\left(\frac{n\pi}{a}x\right) \cos\left(\frac{m\pi}{\phi_o}\phi\right) e^{-j\beta_{nm}\rho} \tag{A60}$$

$$E_x = \frac{1}{jkY_o} \left(k^2-\left(\frac{n\pi}{a}\right)^2\right) \frac{1}{\sqrt{\beta_{nm}\rho}} \cos\left(\frac{n\pi}{a}x\right) \sin\left(\frac{m\pi}{\phi_o}\phi\right) e^{-j\beta_{nm}\rho} \tag{A61}$$

$$H_\rho = \left(\frac{m\pi}{\rho\phi_o}\right) \frac{1}{\sqrt{\beta_{nm}\rho}} \cos\left(\frac{n\pi}{a}x\right) \cos\left(\frac{m\pi}{\phi_o}\phi\right) e^{-j\beta_{nm}\rho} \tag{A62}$$

$$H_\phi = - \frac{1}{\sqrt{\beta_{nm}\rho}} \cos\left(\frac{n\pi}{a}x\right) \sin\left(\frac{m\pi}{\phi_o}\phi\right) (-j\beta_{nm}) e^{-j\beta_{nm}\rho} \tag{A63}$$

These modal expressions under the approximations defined by Equations (A46) through (A48) become equivalent to the TM_x modes in a rectangular waveguide.

APPENDIX III

APPLICATION OF THE RECIPROCITY THEOREM TO FIND THE COUPLING OF INCIDENT ENERGY INTO THE MODAL FIELD BY KNOWING THE MODAL RADIATION FROM THE OPEN END OF A RECTANGULAR WAVEGUIDE

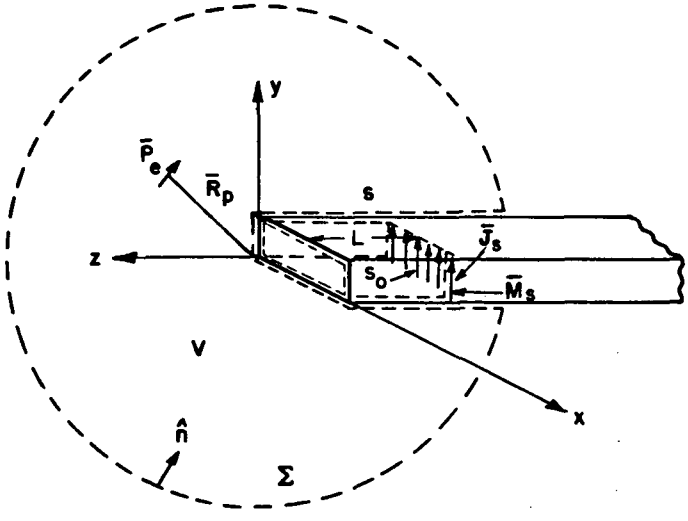


Figure A3. The geometry of the problem.

Figure A3 shows an open ended rectangular waveguide geometry with perfectly conducting walls. Let there be modal fields inside the waveguide propagating in $+\hat{z}$ direction and represented by:

$$\bar{E}_n^+ = c_n^+ (\bar{e}_n + \bar{e}_{zn})\, e^{-j\beta_n z} \tag{A64}$$

$$\bar{H}_n^+ = c_n^+ (\bar{h}_n + \bar{h}_{zn})\, e^{-j\beta_n z} \tag{A65}$$

where $\bar{e}_n$ (or $\bar{h}_n$) is the transverse electric (or magnetic) field, and $\bar{e}_{zn}$ (or $\bar{h}_{zn}$) is the longitudinal electric (or magnetic) field. c_n^+ is the coefficient of the nth mode.

Some of the energy carried by this modal field will be radiated into the free space through the aperture. The far field radiation can be calculated approximately by the aperture integration of the modal field and the resulting radiated fields are shown by $\bar{E}^r$ and $\bar{H}^r$.

The rest of the energy of the incident mode will reflect back to the guide in terms of an mth mode.

$$\bar{E}_m^- = \Gamma_{mn}\, c_n^+ (\bar{e}_m - \bar{e}_{zm})\, e^{j\beta_m z} \tag{A66}$$

$$\bar{H}_m^- = \Gamma_{mn}\, c_n^+ (-\bar{h}_m + \bar{h}_{zm})\, e^{j\beta_m z} \tag{A67}$$

where Γ_{nm} is the complete modal reflection coefficient from the open end.

First consider the geometric plane defined by z=-L inside the semi-infinite pipe, and let S_o denote the area of this waveguide cross section at z=-L as shown in Figure A3. Then let S denote the surface area which tightly encapsulates the complete outer (exterior) surface of the semi-infinite waveguide, and also a portion of the inner walls of this waveguide up to the distance z=-L within the guide. The surface S does not include the plane at z=-L within the pipe. Let Σ denote the sphere at infinity which surrounds the semi-infinite guide such that S on the exterior or outer wall of the semi-infinite guide is connected to

the surface Σ at $z \to -\infty$ as in Figure A3. Next, consider the following two cases. In the first case, the semi-infinite rectangular waveguide is excited from within by the modal fields with amplitude c_n^+ which propagate in the $+\hat{z}$ direction. However, in the second case, the geometry is excited by external fields, $\bar{E}^e$ and $\bar{H}^e$, which for convenience is assumed to be produced by an electric test source $\bar{J}_e$ at $\bar{R}_p$ exterior to and in the far zone of the semi-infinite guide.

Let the equivalent sources $\bar{J}_s$ and $\bar{M}_s$ be located at z=-L in the guide,

$$\bar{J}_s = \hat{n} \times \left[c_n^+ (\bar{h}_n + \bar{h}_{zn}) e^{j\beta_n L} + \sum_m \Gamma_{mn} c_n^+ (-\bar{h}_m + \bar{h}_{zm}) e^{-j\beta_m L} \right] \tag{A68}$$

$$\bar{M}_s = -\hat{n} \times \left[c_n^+ (\bar{e}_n + \bar{e}_{zn}) e^{j\beta_n L} + \sum_m \Gamma_{mn} c_n^+ (\bar{e}_m - \bar{e}_{zm}) e^{-j\beta_m L} \right] \tag{A69}$$

where $\hat{n}$ is the unit vector pointing into the volume V, enclosed by surfaces $S+S_o+\Sigma$. Form reciprocity one obtains:

$$\int\int_{\Sigma+S+S_o} \left[\bar{E}^r \times \bar{H}^e - \bar{E}^e \times \bar{H}^r \right] \cdot \hat{n} ds = \int\int\int_V \bar{J}_e \cdot \bar{E}^r \, dv \tag{A70}$$

However, by the boundary conditions

$$\hat{n} \times \bar{E}^r \Big|_{\text{on } S} = 0 \quad , \tag{A71}$$

and

$$\hat{n} \times \bar{E}^e \Big|_{\text{on } S} = 0 \quad . \tag{A72}$$

Also, $(\bar{E}^r, \bar{H}^r)$ and $(\bar{E}^e, \bar{H}^e)$ satisfy the radiation condition on Σ. Therefore Equation (A70) reduces to:

$$- \iint_{S_o} \bar{H}^e \cdot M_s \, ds + \iint_{S_o} \bar{E}^e \cdot \bar{J}_s \, ds = \bar{p}_e \cdot \bar{E}^r (\bar{R}_p) \quad , \tag{A73}$$

since

$$\bar{J}_e = \bar{p}_e \, \delta (|\bar{R}-\bar{R}_p|) \quad , \tag{A74}$$

a point source in the far field.

In Equation (A74) $\bar{R}_p$ is the position vector from the reference point to point P.

Inside the waveguide the fields $\bar{E}^e$ and $\bar{H}^e$ will have the following representation

$$\bar{E}^e = \sum_p A_p^- (\bar{e}_p - \bar{e}_{zp}) \, e^{j\beta_p z} \tag{A75}$$

$$\bar{H}^e = \sum_p A_p^- (-\bar{h}_p + \bar{h}_{zp}) \, e^{j\beta_p z} \tag{A76}$$

Substituting Equations (A75) and (A76) into Equations (A73) one obtains:

$$- \iint_{S_o} \sum_p A_p^- (-\bar{h}_p+\bar{h}_{zp}) \, e^{-j\beta_p L} \, c_n^+ \left[\bar{e}_n x \hat{z} \, e^{j\beta_n L} + \sum_m \Gamma_{mn} (\bar{e}_m x \hat{z}) e^{-j\beta_m L} \right] ds$$

$$- \iint_{S_o} \sum_p A_p^- (\bar{e}_p-\bar{e}_{zp}) \, e^{-j\beta_p L} \, c_n^+ \left[(\hat{z} \times \bar{h}_n) e^{j\beta_n L} - \sum_m \Gamma_{mn} (\hat{z} x \bar{h}_m) e^{-j\beta_m L} \right] ds$$

$$= \bar{p}_e \cdot \bar{E}^r (\bar{R}_p) \tag{A77}$$

Using the orthogonality properties of waveguide modes one obtains:

$$\left[\iint_{S_o} \bar{e}_n \times \bar{h}_n \cdot \hat{z} \, ds \right] (-c_n^+ A_n^-) \, 2 = \bar{p}_e \cdot \bar{E}^r (\bar{R}_p) \tag{A78}$$

$$-2 \, c_n^+ A_n^- = \frac{\bar{p}_e \cdot \bar{E}^r (\bar{R}_p)}{\iint_{S_o} \bar{e}_n \times \bar{h}_n \cdot \hat{z} \, ds} \tag{A79}$$

In order to produce an incident field $\bar{E}^i = \hat{\theta} E_\theta^i + \hat{\theta} E_\phi^i$ at the opening of the waveguide, one can let

$$\bar{p}_e = - (\hat{\theta} E_\theta^i + \hat{\phi} E_\phi^i) \frac{4\pi}{j\omega\mu} R_p \, e^{jkR_p} \tag{A80}$$

Thus,

$$A_n^- = \frac{(\hat{\theta} E_\theta^i + \hat{\phi} E_\phi^i) \cdot \bar{E}^r (\bar{R}_p) \, R_p \, e^{jkR_p}}{-2 \, c_n^+ \iint_{S_o} \bar{e}_n \times \bar{h}_n \cdot \hat{z} \, ds} \quad \frac{4\pi}{j\omega\mu} \tag{A81}$$

APPENDIX IV

CORRECTION FOR THE APERTURE INTEGRATION

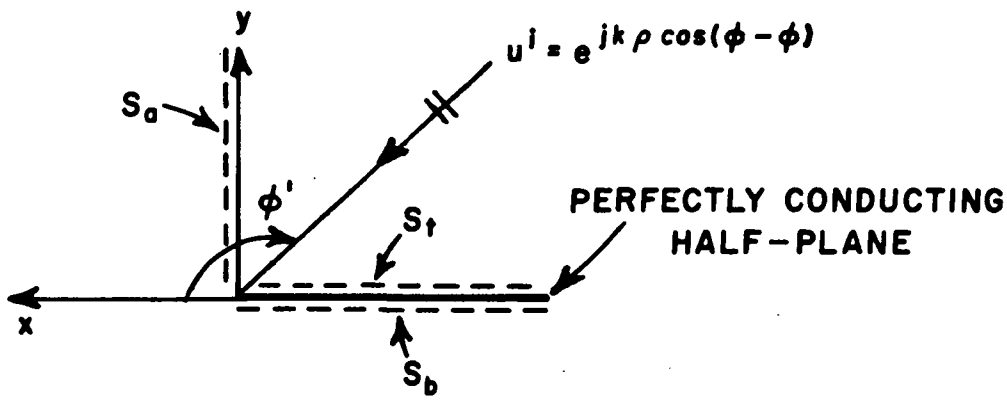


Figure A4. Scattering from a perfectly-conducting half-plane.

As shown in the figure, a perfectly conducting half-plane is located in the region y=0, x<0. The half-plane is illuminated by a plane wave $u^i = e^{jk\rho\cos(\phi-\phi')}$ $(\pi/2 < \phi' < \pi)$.

Let S_t, S_b denote the top and bottom surfaces of the half plane, respectively and S_a denote the aperture surface at x=0, y>0.

Since the geometry is infinite in z-direction the problem can be reduced to a scalar problem where the total field u may represent either the $\hat{z}$-component of the electric field (E_z) or the $\hat{z}$-component of the

magnetic field (H_z). The former case is called the soft case and the latter is called the hard case. The analysis for both cases are very similar, therefore only the soft case will be considered here. In this case, the total field E_z can be written as the combination of three contributions; namely, the incident, the reflected and the diffracted fields. The incident and reflected fields are also called as the geometrical optics (GO) fields. The GO field is given by the following expressions:

$$E_z^{go} = e^{jk\rho\cos(\phi+\phi')} - e^{jk\rho\cos(\phi+\phi')} = e^{jk_x^i x}\, 2j\sin k_y^i y \quad ; \text{ on } S_t,\ S_a$$
$$= 0 \quad ; \text{ on } S_b \qquad \text{(A82)}$$

since S_b is in the shadow region of the half-plane. In Equation (A82),

$$k_x^i = k\cos\phi' \qquad \text{and} \qquad k_y^i = k\sin\phi' \qquad \text{(A83a;b)}$$

The transverse fields can be calculated using

$$-jkZ_o\, \bar{H} = \left(-\hat{y}\,\frac{\partial}{\partial x} + \hat{x}\,\frac{\partial}{\partial y}\right) E_z \qquad \text{(A84)}$$

Therefore, the transverse geometrical optics fields can be obtained using Equations (A82) and (A83).

$$-jkZ_o\, H_x^{go} = jk_y^i\, e^{jk_x^i x}\, 2\cos k_y^i y \qquad \text{(A85)}$$

$$-jkZ_o\, H_y^{go} = -jk_x^i\, e^{jk_x^i x}\, 2\sin k_y^i y \qquad \text{(A86)}$$

In the physical optics (PO) approximation, one uses the following radiation integral to get the scattered field using the GO fields on the illuminated side of the half-plane (S_t).

$$\bar{E} = \int_S ds' \left[-jkZ_o G_o (\hat{n}x\bar{H}) + (\hat{n}x\bar{E}) \times \nabla G_o\right] \tag{A87}$$

where

$$G_o = \frac{j}{4} H_o^{(2)} (k|\bar{\rho}-\bar{\rho}'|) \tag{A88}$$

is the free-space Green's function in two-dimensions.

One notes that on S_t; $\hat{n} \times \bar{E} = 0$. Therefore the PO approximation to scattered field is given by:

$$E_z^{PO} = \int_{S_t} ds' \left[-jkZ_o G_o (\hat{y}x\bar{H}^{go})\right] \tag{A89}$$

Using Equations (A85) and (A86) in Equations (A89), one obtains:

$$E_z^{PO} = -\int_0^\infty \left[-jkZ_o H_x \cdot G_o\right] dx' \tag{A90}$$

The Green's function Go can also be written as:

$$G_o = -\frac{j}{4\pi} \int_{-\infty}^{\infty} dk_y \frac{e^{-jk_y y - jk_x x}}{k_x} e^{jk_y y'} = -\frac{j}{4\pi} \int_{-\infty}^{\infty} dk_x \frac{e^{-jk_x x - jk_y y}}{k_y} e^{jk_x x'} \tag{A91}$$

where

$$k_x^2 + k_y^2 = k^2 \tag{A92}$$

Substituting Equations (A85) and (A91) into Equations (A90) and changing the order of integration, one obtains:

$$E_z^{PO} = \frac{-1}{2\pi} \int_{-\infty}^{\infty} dk_x \frac{e^{-jk_x x - jk_y y}}{k_y} k_y^i \int_o^{\infty} e^{jk_x^i x' + jk_x x'} dx' \qquad \text{(A93)}$$

$$E_z^{PO} = \frac{-j}{2\pi} \int_{-\infty}^{\infty} \frac{e^{-jk_x x - jk_y y}}{k_y} \frac{k_y^i}{k_x^i + k_x} dk_x \qquad \text{(A94)}$$

Using the transformation

$$k_x = k\cos\alpha \qquad k_y = k\sin\alpha \quad , \qquad \text{(A95a;b)}$$

Equation (A94) becomes

$$E_z^{PO} = \frac{-j}{2\pi} \int_{C_\alpha} e^{-jk\rho\cos(\alpha-\phi)} \frac{\sin\phi'}{\cos\alpha+\cos\phi'} d\alpha \qquad \text{(A96)}$$

where the integration path C_α is shown below:

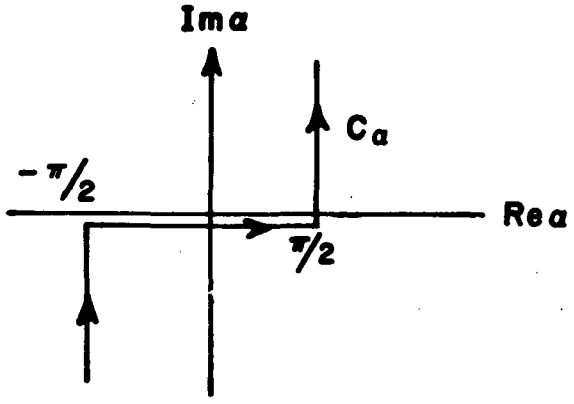


Figure A5. The integration path C_α.

On the other hand, if one integrates the GO fields over S_a and S_b to get the scattered field, one obtains:

$$E_z^k = \int_{Sa} ds' \left[-jkZ_0 G_0 (\hat{x}x\hat{y} H_y^{go}) + (\hat{x}x\hat{z} E_z^{go}) \times \nabla G_0\right] \tag{A97}$$

since GO field is zero on S_b.

Using Equations (A82), (A86) and (A91) in Equations (A97), one obtains:

$$E_z^k = \frac{j}{4\pi} \int_{-\infty}^{\infty} dk_y \, e^{-jk_y y - jk_x x} \left[\frac{1}{k_y + k_y^i} - \frac{1}{k_y - k_y^i}\right] \frac{(k_x^i - k_x)}{k_x} \tag{A98}$$

Using the transformations in Equation (A95), one finally obtains:

$$E_z^k = -\frac{j}{2\pi} \int_{C_\alpha} e^{-jk\rho\cos(\alpha-\phi)} \frac{\sin\phi'}{\cos\alpha+\cos\phi'} d\alpha \tag{A99}$$

Equations (A96) and (A99) are exactly the same, therefore the Ufimtsev edge correction [6] to Equation (A96) can be used without modification to correct for the aperture integration result of Equation (A99).